Title
Fatigue of Aluminum-Lithium Alloys

Authors
Rao, K.T. Venkateswara
Ritchie, R.O.

Publication Date
1992

LBL-30176
Preprint

Center for Advanced Materials

CAM

Submitted to International Materials Reviews

Fatigue of Aluminum-Lithium Alloys

K.T. Venkateswara Rao and R.O. Ritchie

January 1991

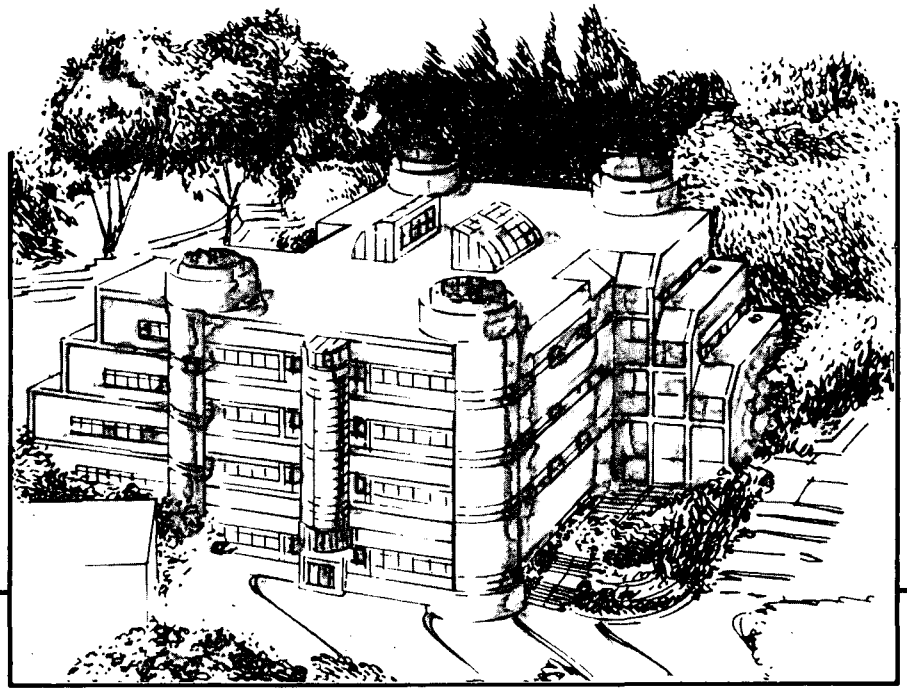

Materials and Chemical Sciences Division

Lawrence Berkeley Laboratory • University of California

ONE CYCLOTRON ROAD, BERKELEY, CA 94720 • (415) 486-4755

Prepared for the U.S. Department of Energy under Contract DE-AC03-76SF00098

DISCLAIMER

LBL-30176

FATIGUE OF ALUMINUM-LITHIUM ALLOYS

K. T. Venkateswara Rao and R. O. Ritchie

Center for Advanced Materials, Lawrence Berkeley Laboratory
and
Department of Materials Science and Mineral Engineering
University of California
Berkeley, CA 94720

submitted to
International Materials Reviews

January 1991

This work was supported by the Director, Office of Energy Research, Office of Basic Energy Sciences, Materials Sciences Division of the U.S. Department of Energy under Contract No. DE-AC03-76SF00098.

FATIGUE OF ALUMINUM-LITHIUM ALLOYS

K. T. Venkateswara Rao and R. O. Ritchie

Center for Advanced Materials, Lawrence Berkeley Laboratory and
Department of Materials Science and Mineral Engineering
University of California, Berkeley, CA 94720

ABSTRACT

Aluminum-lithium alloys are a class of low-density, high-strength, high stiffness monolithic metallic materials that have been identified as prime candidates for replacing 2000 and 7000 series aluminum alloys currently used in commercial and military aircraft. In this review, the cyclic fatigue strength and fatigue-crack propagation characteristics of aluminum-lithium alloys are reviewed in detail with emphasis on the underlying micromechanisms associated with crack advance and their implications to damage-tolerant design and lifetime computations. Compared to traditional aerospace aluminum alloys, results on the fatigue of binary Al-Li, experimental Al-Li-Cu, and near-commercial Al-Li-Cu-Zr and Al-Li-Cu-Mg-Zr systems indicate that alloying with Li degrades the low-cycle fatigue resistance, although high-cycle fatigue behavior remains comparable. The alloys, however, display superior (long-crack) fatigue-crack growth properties, resulting from a prominent role of crack-tip shielding, principally due to deflected and tortuous crack-path morphologies, induced by the shearable nature of coherent δ' precipitates, crystallographic texture and anisotropic grain structures. Environmental fatigue resistance is comparable to 2000 series alloys and better than 7075-type alloys. The accelerated growth of small fatigue cracks, strong anisotropy, poor short-transverse properties and a sensitivity to compression overloads are the principal disadvantages of Al-Li alloys.

INTRODUCTION

Designers of modern commercial and military aerospace vehicles and space launch systems are constantly in search for new materials with lower density, and higher strength, stiffness and stability at elevated or cryogenic temperatures. To meet these challenges, much effort has been directed toward developing intermetallics, ceramics and composites as structural and engine materials for future applications (1-6). However, for structural airframes, age-hardened 2000 and 7000 series aluminum alloys have long been preferred for civil and military aircraft by virtue of their high strength-to-weight ratio, although the use of composite materials, particularly for secondary structures, is rapidly increasing. Nearly 75% of the structural weight of the Boeing 757-200 airplane is comprised of plates, sheets, extrusions and forgings of 2024, 2224, 2324, 7075 and 7150 aluminum alloys (7); typical components

---

K. T. Venkateswara Rao, M.S., Ph.D. and Professor R. O. Ritchie, M.A., Ph.D., Sc.D., F.I.M., C.Eng., are with the Center for Advanced Materials, Lawrence Berkeley Laboratory, and the Department of Materials Science and Mineral Engineering, University of California, Berkeley, CA 94720, USA.

include, body frames, fuselage (frames, skins and substructures), wings (stiffeners, ribs, stringers and skins), and horizontal stabilizers.

Today, conventional aluminum alloys face stiff competition from emerging composite technologies, particularly in the structural aerospace market; hybrid materials based on organic and metal matrices with fiber, whisker or particulate ceramic reinforcements offer impressive combinations of strength, stiffness and high-temperature resistance (2,8-12). In addition, aramid polymer-reinforced aluminum alloy (ARALL) laminates (13-15), fabricated by resin bonding aramid fibers sandwiched between thin aluminum-alloy sheets, show exceptional promise as fatigue-resistant materials. In the light of these advances, the aluminum industry has recently introduced a new generation of aluminum-lithium alloys,* by additionally incorporating ultra-low density lithium into traditional aluminum alloys; these alloys represent a new class of light-weight, high-modulus, high-strength, monolithic structural materials, which are cost-effective compared to the more expensive composites (16-28).

* Although this class of alloys contains alloying elements like copper, magnesium, and zirconium in addition to aluminum and lithium, the term aluminum-lithium (or Al-Li) alloys is generally used to encompass all aluminum alloys containing greater than 0.5 wt.% lithium.

Despite possible limitations regarding specific-stiffness and high-temperature stability, Al-Li alloys enjoy several advantages over composite materials. Economically, Al-Li alloys are typically only three times as expensive as conventional aluminum alloys, whereas competing hybrid materials can be up to 10 to 30 times more expensive (28). Secondly, Al-Li alloy fabrication technology is generally compatible with existing manufacturing methods such as extrusion, sheet forming and forging to obtain finished products. Finally, they offer considerably higher ductility and fracture-toughness properties compared to most metal-matrix composites (9-12).

Historically, efforts to design lithium-containing aluminum alloys date back to the early 1920s, although concerns over their poor ductility and toughness halted production and use in the 1960s; references 26, 27, 29, and 30 provide an excellent review of these developments. Escalation in fuel costs during the 1970s rekindled research on the Al-Li system with prospects of building more fuel-efficient aircraft; design trade-off studies had shown that reducing density was the most optimal route (30-32). Each weight-percent of lithium added to aluminum lowers the density approximately 3% and improves the elastic modulus by nearly 6% for Li additions of up to 4 wt.% (21,33). Accordingly, direct substitution of Al-Li alloys (containing $\sim$3 wt.% Li) for traditional aluminum alloys can yield $\sim$11% weight-savings; complete redesign of aircraft utilizing the full potential of Al-Li alloys could save up to $\sim$17% by weight (30).

Early studies by Sanders and Starke (21,34) on binary Al-Li alloys showed that problems of low ductility and toughness could be traced to inhomogeneous slip and strain localization, resulting from coherent δ' (Al_3Li) particle hardening in the matrix, nucleation and growth of grain boundary δ (AlLi)

precipitates, and the formation of δ'-precipitate free zones (PFZs). Subsequent developments in alloy design and processing have attempted to reduce this inhomogeneous deformation mode by incorporating additional alloying elements and modifying thermomechanical treatments. As a result, advanced commercial Al-Li-X-Y-Z alloys today exhibit strength-toughness combinations which are comparable, and often superior, to traditional aluminum alloys 2024, 2124, 7075, 7150 and 7475, particularly at cryogenic temperatures (35-42). Details of the principal alloys of commercial interest, their designations and nominal chemical composition limits are summarized in Table I.

Since advanced Al-Li alloys are principally targeted for safety-critical structural aerospace applications, their durability and damage tolerance performance are of considerable importance. Over the last decade, a number of investigations have focused on various aspects of fatigue crack-initiation and crack-propagation in Al-Li alloys. It is therefore the objective of the present paper to review these cyclic properties with emphasis on the underlying micromechanisms; reviews on the crack-growth mechanisms under monotonic loading may be found in Refs. 43 and 44. Crack-initiation and crack-growth behavior is examined as a function of microstructural, mechanical, and environmental factors. It is concluded that in general the fatigue behavior of Al-Li alloys is not significantly different from traditional aluminum alloys, although crack-propagation kinetics of long cracks are retarded by more pronounced crack-tip shielding* from such mechanisms as crack deflection, crack-path tortuosity and consequent roughness-induced crack-closure mechanisms. In fact, the observed variations in fatigue resistance of Al-Li alloys with respect to microstructure, crack size, loading sequence and product form are largely a manifestation of the degree to which shielding is promoted or restricted in the different microstructures under various loading conditions.

* Crack-tip shielding mechanisms act to impede crack advance by lowering the local stress intensity actually experienced at the crack tip (45,46). Such mechanisms, which act principally in the crack wake, include transformation and microcrack toughening in ceramics, crack bridging in composites, and crack closure during fatigue-crack growth. Closure mechanisms are described in detail in the section on Fatigue Crack Propagation.

MICROSTRUCTURAL FEATURES

Strengthening in Al-Li alloys is predominantly from hardening by the nucleation and growth of one or more second-phase particle distributions, precipitated from a supersaturated solid solution. This is achieved by aging naturally (at room temperature) or artificially (at an elevated temperature below the metastable solvus line) following solution treatment and quenching the alloy from the single-phase field. By controlling the aging time and temperature, microstructures are optimized for targeted mechanical properties in the various tempers. Generally, these temper designations are referred to as i) underaged (T3), synonymous with low strength and fine uniform distributions of coherent hardening precipitates in

the matrix, ii) peak-aged (T6, T8), with maximum strength and partially-coherent precipitates, and iii) over-aged (T7), with slightly reduced strength and coarse incoherent precipitates. Many published papers (16-20,47-56) have extensively reviewed the solid-state phase transformations and precipitation sequences in Al-Li alloys; salient microstructural features are summarized below.

Binary Al-Li Alloys

Binary alloys of aluminum containing less than ~1.7 wt. % Li are essentially random solid solutions of aluminum and lithium. The elevated flow stress compared to pure aluminum is due to short-range order and dislocation interactions between solute atoms and associated strain fields. For lithium contents greater than 1.7 wt. %, the alloys are hardened by long-range ordering through the precipitation of ordered ($L1_2$ structure), metastable and spherical δ' particles, in an α (fcc) Al-Li solid solution matrix. Due to the low particle/matrix misfit strains (~-0.12%), the precipitates tend to remain coherent with the matrix and retain their spherical morphology, even for particle diameters as large as 300 nm (54). In the naturally-aged condition (or underaged tempers), microstructures show fine homogeneous distributions of δ' particles (2-5 nm in diameter) in the matrix and at grain boundaries. With increased aging time and/or temperature, the matrix δ' precipitates coarsen, and equilibrium δ particles nucleate heterogeneously along grain boundaries, thereby resulting in the formation of Li-depleted δ'-PFZs surrounding δ. Improvements in strength in these alloys are primarily due to the resistance of δ'-particles to dislocation motion (from order-hardening, elastic-moduli differences and misfit coherency strains between the matrix and precipitates); the extent of hardening is proportional to both the volume fraction and size of δ' precipitates. However, deformation in binary alloys is highly localized along narrow slip bands and within soft-PFZs, which can promote premature crack nucleation, and contribute to poor ductility and toughness of Al-Li alloys (34). Typical chemical compositions, heat treatments and mechanical properties of selected binary alloys are summarized in Table II.

Ternary Al-Li-Cu and Al-Li-Mg Alloys

To reduce the inhomogeneous mode of deformation, ternary elements have been incorporated in Al-Li alloys to enable the nucleation of additional hardening precipitates and to modify the coherency strains between δ' particles and the matrix. For example, Al-Li alloys containing 2-3 wt. % Cu are strengthened by semi-coherent T_1 (Al_2CuLi) and θ'-like (Al_2Cu) plates in the matrix. Precipitation of the equilibrium T_2 (Al_6CuLi_3) phase is sometimes observed along grain and subgrain boundaries particularly in peak and overaged tempers. Moreover, in addition to the commonly observed spherical morphology, the ordered δ'-phase also forms surrounding the θ' plates. In Al-Li-Mg alloys containing less than 2 wt. % Mg, δ' is the only hardening phase; however, magnesium reduces the solid-solubility of

lithium in aluminum and hence increases the volume fraction of δ' precipitates. At longer aging times and for alloys with Mg-contents greater than 2 wt.%, Al_2MgLi precipitates in the matrix and along grain boundaries.

Commercial Alloys

Commercial Al-Li alloys are alloyed with Cu, Mg and dispersoid-forming elements like Zr, Mn and Cr that form a fine dispersion of intermetallic phases to reduce the tendency for localized deformation. Zr is generally preferred because it results in fine as-cast grain structures and better corrosion properties. In addition, to reduce the deleterious effects of δ'-PFZs on ductility and toughness, wrought Al-Li sheet and plate products are given a 2-6% permanent stretch prior to aging; this promotes uniform intragranular precipitation and thus suppresses heterogeneous grain-boundary precipitation phenomena.

The resulting grain structures for most ingot-metallurgy (I/M)-based high-strength aluminum alloys following such thermomechanical processing are pan-cake shaped and elongated in the rolling direction; Al-Li alloy sheet and plate, however, show a greater degree of anisotropy due to the small Zr additions which can effectively suppress recrystallization and retard grain growth. As shown in Fig. 1a, grain sizes in I/M alloys are fairly coarse, typically 500 μm wide, 50 μm thick and several mm in length; the exception is the 8091 alloy where grain sizes are finer (58). Microstructures in powder-metallurgy (P/M) processed Al-Li alloys are more refined; grain sizes are typically between 0.5-5 μm and the structures are less anisotropic (Fig. 1b,c). Strong deformation textures are common in I/M alloys owing to prior thermomechanical treatments. These textures are found to be predominantly of the "brass" type ($\{110\}<112>$), with evidence of weaker "S" ($\{123\}<634>$) and "copper" ($\{112\}<111>$) types (59-66). However, the various components of texture vary strongly across the thickness of the plate with the intensity of each component showing a maximum at the center (59); moreover, $\{001\}<110>$ type recrystallization textures are observed in the near-surface regions (62). Chemical compositions and thermomechanical treatments for the principal commercial Al-Li alloys are listed, respectively, in Tables II and III.

In underaged tempers, commercial Al-Li alloys are strengthened by metastable δ' spheres, β' (Al_3Zr, also referred to as α') dispersoids and composite precipitates of δ' surrounding β' (Fig. 2a). Al_3Zr particles are spherical, coherent and ordered with an $L1_2$ superlattice structure. In addition, aging to peak strength (T8 condition) in Al-Li-Cu-Zr (2090) systems causes matrix precipitation of T_1 and θ' plates, coarsening of matrix-δ', the formation of relatively narrow ($\sim$100 nm-wide) δ'-PFZs at high-angle grain boundaries, and fine precipitation of T_1 plates along subgrain boundaries (Figs. 2a,b). In Mg-containing alloys, T_1 and θ' plates are replaced by S (Al_2CuMg) laths in the matrix (Fig. 2c); precipitation of T_1 occurs in competition with S for available nucleation sites and copper atoms. For

example, precipitation of T_1 plates has been reported for 8090-type alloys but not for 8091 compositions (47). Despite the pre-aging deformation, grain-boundary effects are prevalent, even in peak-aged tempers. In 8090-T8, small amounts of grain-boundary precipitation result in $\sim$500 nm-wide δ'-PFZs (Fig. 2d); in 8091-T8, heterogeneous precipitation is more extensive and PFZs are correspondingly wider ($\sim 1\ \mu$m).

With longer aging times (overaged tempers), coarse equilibrium Cu- and/or Mg-rich phases and T_1 plates or T_2 precipitates decorate grain and subgrain boundaries, respectively, concurrently leading to the formation of solute-denuded PFZs. In addition, undissolved impurities during processing are also present as coarse Fe- and Cu-rich intermetallic phases along the elongated high-angle grain boundaries. Microstructural details and room-temperature mechanical properties of the principal I/M and P/M Al-Li alloys are summarized in Tables IV and V, respectively.

Specific Al-Li alloys can be $\sim$30% higher in strength with similar elongation and toughness properties when compared to traditional aluminum alloys (Table V). However, these properties are typical of thermomechanically-processed wrought product forms (namely pre-stretched and artificially-aged sheet and plate) in the longitudinal orientation; generally short-transverse properties are considerably less attractive. The unrecrystallized elongated grain structures and deformation-texture variations ensure that properties are strongly dependent on orientation, both in the rolling plane and through the plate thickness (41,64-67). Moreover, the excellent strength and toughness properties, characteristic of sheet and plate products, are often compromised for forgings, extrusions and thick-section plates, where uniform quenching rates and pre-aging deformation are not feasible (64-72).

CYCLIC STRESS-STRAIN AND FATIGUE-CRACK INITIATION BEHAVIOR

The application of cyclic loads to metallic materials at stress levels much below the yield or tensile strengths can significantly alter their constitutive behavior. Depending on the initial wrought product form, heat treatment and applied plastic-strain amplitude ($\Delta\epsilon_p/2$), the material may undergo cyclic softening, cyclic hardening, show mixed (hardening and softening) response, or have no effect at all (73). Following transient hardening or softening, materials generally exhibit saturation or stability at some equilibrium stress or strain value, before eventually softening due to incipient damage or crack nucleation. High-strength aluminum alloys are good examples of cyclic hardening materials, whereas softening is observed in quenched and tempered steels; low-carbon steels, high-strength low-alloy (HSLA) steels and titanium alloys are examples of materials which initially soften before hardening (73). The cyclic stress-strain properties are traditionally evaluated either in low-cyclic fatigue (LCF), where the strains are predominantly plastic, or in high-cyclic fatigue (HCF), where the macroscopic strains are predominantly elastic. Typically, lifetimes under LCF conditions are below $\sim 10^3$ cycles, whereas HCF pertains to lives exceeding $\sim 10^3$ cycles.

Low-Cycle Fatigue (LCF) Behavior

Similar to most high-strength Al alloys, Al-Li alloys in general initially harden under cyclic loading, particularly at low plastic-strain amplitudes (typically $\Delta\epsilon_p/2$ below $\sim 10^{-3}$), followed by saturation before softening to final fracture (57,74,80,85). At higher plastic strains ($\Delta\epsilon_p/2$ above $\sim 10^{-3}$), however, the alloys continuously soften to failure with little cyclic stability (57,75,81,85). Similar trends are apparent for most experimental and commercial Al-Li alloys, although the extent of hardening, saturation or softening and resultant fatigue lifetimes are a strong function of alloy composition, microstructure, temperature and environment (34,57,74-91). Typical variations in the cyclic stress amplitude with applied strain, under fully-reversed strain-controlled loading for binary Al-Li alloys and commercial 8090-T6 alloy, are illustrated in Fig. 3; corresponding monotonic and stabilized cyclic stress-strain curves are compared in Fig. 4.

Binary Al-Li alloys

Strengthening by lithium in solid solution ($\lesssim 1.7$ wt. % Li) yields microstructures which initially cyclically harden at plastic strain amplitudes less than $\sim 10^{-3}$, before softening and eventually attaining cyclic stability until fracture (57,78-80). Hardening can be permanent for alternating strains greater than $\sim 10^{-3}$ with no saturation before softening (57) (Fig. 3); corresponding cyclic stress-strain curves show continuous hardening to failure without any plateau region (Fig. 4a). The elevated flow stress during fatigue can be attributed to an increase in the dislocation density, dislocation-dislocation interactions and dislocations interacting with solute-atom strain fields (74). Transmission electron microscopy (TEM) observations reveal the deformation to be largely homogeneous (34,57). Cellular dislocation structures, similar to those observed in single-phase, high stacking-fault energy fcc metals, are common particularly at high plastic-strain amplitudes (Fig. 5a), although they are slightly more elongated and less polygonized compared to pure aluminum (wavy slip); no veins or ladder-like persistent slip bands (PSBs) are seen. At low plastic-strain amplitudes slip is planar (34). With increased deformation, softening is associated with the nucleation of microcracks along slip-band intrusions emerging on the surface for $\Delta\epsilon_p/2 < 10^{-3}$, and along grain boundaries or where slip bands impinge at grain boundaries for $\Delta\epsilon_p/2 > 10^{-3}$. Propagation of the fatal crack occurs by non-crystallographic, ductile striation-type crack-growth mechanisms (Fig. 5b) that involve alternating shear or successive blunting and resharpening of the crack tip (34,57,80).

In contrast, aged microstructures with lithium contents exceeding ~ 1.7 wt. % that are precipitation-hardened by δ' particles (e.g., Al-2.5wt. % Li alloy), show significant cyclic hardening (Figs. 3,4a). Cyclic stress/strain curves show an initial increase in stress amplitude due to dislocation interactions, with small saturation periods (which diminish with artificial aging), followed by softening

to failure from δ' shearing and strain localization (34). Unlike dislocation cell structures in solid-solution hardened microstructures, fatigue deformation is inhomogeneous and slip is essentially planar for all plastic strain amplitudes (34,57); intense slip bands are developed parallel to {111} planes (Fig. 5c).

However, the strong cyclic-hardening behavior of Al-Li alloys with higher Li-content and higher δ' volume fractions is offset by marked reductions in LCF resistance, as shown by the Coffin-Manson curves in Fig. 6a. Although solid-solution hardened and underaged microstructures experience only limited losses in fatigue strength compared to pure aluminum (an exception is underaged alloys at low plastic-strains where slip is planar), fatigue lives are reduced by as much as four orders of magnitude in artificially peak-aged and overaged binary Al-Li alloys (34,57,75-82).

The detrimental effects of Li on the LCF resistance of Al-Li alloys is principally due to the presence of large volume fractions of shearable, ordered δ' precipitates; small Li additions which go into solid solution have almost no effect (34,57). During deformation, initial dislocation motion shears the δ' precipitates and reduces order by creating antiphase domain boundaries within the particles; following dislocations preferentially move on the same glide plane at a lower resolved stress to restore order, thus resulting in pair-dislocation motion and a tendency toward planar slip. Additionally, planar slip is promoted by the reduced effective diameter of sheared δ' particles and reductions in the stacking-fault energy of aluminum due to Li additions (34). As such, deformation is localized along narrow PSBs parallel to the {111} glide planes causing stress concentrations at their intersection with grain boundaries. These effects become more pronounced in the peak and overaged tempers due to an increase in size and amount of δ' particles (34,57); equilibrium δ precipitates further accentuate this effect by aggravating the degree of strain localization in the soft δ'-PFZs at grain boundaries. Microcrack nucleation at dislocation pile-ups is common for all plastic-strain amplitudes; coalescence of these microcracks to form a fatal flaw may occur crystallographically along slip bands or at weakened grain boundaries, depending on the alloy temper. As shown in Fig. 5d, fatigue fracture in underaged Al-2.5 wt. % Li is transgranular as microcracks link up by slip-band cracking (34,57). Conversely, intergranular cracking is prevalent in the peak and overaged microstructures; few secondary cracks initiate, and the first intergranular crack to nucleate propagates catastrophically to failure.

Commercial Al-Li alloys

In commercial Al-Li alloys, cyclic and monotonic flow stresses are substantially higher, and fatigue lives correspondingly lower, compared to binary Al-Li alloys because of additional strengthening from T_1 and S precipitates (Figs. 4b, 6b). T_1 and S precipitates are thought to favor a dispersion of slip and promote plastic-strain homogenization at the subgrain level through the activation of multiple slip systems within the grain. However, inhomogeneous fatigue deformation still occurs along PSBs or embrittled grain boundaries. In fact, the partially coherent S precipitates have been observed to shear

during fatigue at high plastic strains, presumably due to stress concentrations at the matrix/S interfaces that favor dislocation nucleation and precipitate cleavage (84). Moreover, the highly textured grain structures in commercial alloys limit the number of slip systems by reducing the effectiveness of grain boundaries as barriers to dislocation motion due to the low degree of misorientation (80-88).

Cyclic stress-strain behavior in commercial alloys is similar to that in binary alloys strengthened by δ' particles (Figs. 3,4b). Limited hardening and stability, followed by softening, is seen at low strain amplitudes due to crack nucleation at slip bands emanating from large ($\sim$1 to 10 μm) cracked or uncracked constituent particles; at high strains, the alloys soften continuously to failure. Crack nucleation occurs in coarse slip bands, possibly at intrusions or extrusions on the specimen surface; hardening and softening are generally associated with dislocation/particle interactions and δ' shear, respectively (86,87). However, Coffin-Manson curves for commercial alloys show a transition at low-strain amplitudes below $\sim 10^{-3}$, which approximately corresponds to strains below which the cyclic stress response is stable (harden) and above which the alloys soften (Fig. 6b). Most studies associate this transition to changes in deformation mechanism, or the degree of slip homogeneity (85-87). Such changes have also been noted in 8090-T8 and 2020-T651 Al-Li alloys; ductile intergranular fractures, characteristic of monotonic failure, are prevalent at high-strain amplitudes above the transition strain, whereas transgranular shear (slip-band cracking) failures are observed below the transition strain, suggesting marked effects of slip planarity at low strain ranges (80-85).

Microstructural factors that enhance slip homogeneity in Al-Li alloys are generally found to improve LCF resistance. For example, stretching (prior to aging) to increase the number density of the partially coherent T_1 and S phases, the addition of dispersoid-forming elements, and fine recrystallized grain structures, are all considered beneficial to LCF (75,80,86-88). In contrast, results in 2020 suggest that unrecrystallized microstructures may exhibit better fatigue resistance over recrystallized structures (75); this effect, however, seems to be associated with the suppression of grain-boundary precipitation by the preaging deformation.

Finally, compared to traditional high-strength aluminum alloys, commercial Al-Li alloys possess comparable fatigue-crack initiation properties (Fig. 6b). In the high-strain region of the Coffin-Manson curve, however, crack-initiation resistance may be somewhat lower in Al-Li alloys due to higher elastic cyclic stresses for a given cyclic strain, resulting from their increased Young's modulus (67).

Stress Instabilities during Cyclic Hardening

Recent studies (89-91) have shown that following cyclic hardening, stabilized cyclic stress-strain curves (or hysteresis loops) for binary Al-Li alloys often exhibit stress instabilities, characterized by successive drops in the fatigue stress (Fig. 7), depending upon the plastic-strain amplitude, alloy temper, test frequency and temperature. For example, the instabilities are only seen at specific temperatures

above 233K for Al-Li microstructures hardened by δ' (as opposed to solid-solution strengthening), when accumulated plastic strains ($2N \times \Delta\epsilon_p/2$, where N is the number of cycles) exceed ~ 0.1 (independent of alloy composition and aging temper), and at frequencies below 0.2 Hz. Moreover, elevated cyclic flow strengths have been measured by interrupting the test and room-temperature aging the material.

Gentzbittel *et al.* (89) suggest that this behavior is influenced by dynamic strain aging or the Portevin-Le Chatelier phenomenon; however, as the stress instabilities are not seen in Al-Li solid solutions (i.e., in Al-0.7 wt. % Li alloy), this implies that the effect is associated with δ' precipitates rather than dislocation-lithium (solute) atom interactions. It is more probable that the effects originate from the instability of small δ' particles ($\gtrsim$ 1.5 nm) to localized shearing by moving dislocations; mechanical instabilities in the fatigue stress are then a result of successive reversion and reprecipitation of δ' in the matrix. In fact, TEM studies by Brechet *et al.* (90) have confirmed this observation. In the early stages of deformation, spherical δ' particles are sheared by dislocations leading to the formation of antiphase domain boundaries (Fig. 8a). On repeated shearing, the δ'-precipitates become unstable from the antiphase boundary energy and dissolve in the matrix. Since deformation is concentrated along narrow bands parallel to the {111} slip planes, the resulting microstructure (Fig. 8b) consists of precipitate-free bands enriched in lithium, where dislocation motion is relatively unimpeded compared to microstructure outside the bands. Finally, assisted by fatigue-induced vacancies, lithium diffuses to the side of the band and reprecipitates as δ', thus enhancing the local coarsening kinetics and volume fraction of δ' particles (snow-plow effect). Simple models proposed to explain the redissolution of δ' within the bands, band width and band separation, based on an increase in the free energy from shear-induced antiphase boundaries, are in reasonable agreement with experimental results (90,91).

Although the precise relevance of such microscopic fatigue-damage processes to macroscopic crack-advance mechanisms is as yet unclear, these observations do confirm that cyclic deformation in Al-Li alloys proceeds by dislocation shearing of the ordered δ' precipitates. Similar studies on the LCF behavior of 8090 and 2020 Al-Li alloys have also shown that, at high plastic-strain levels, spherical δ', lath-like S precipitates and even Al_3Zr dispersoids are shearable and may contribute to low fatigue lives (83,84,86).

High-Cycle or S/N Fatigue

In contrast to LCF behavior where Li in the form of δ' precipitates has an adverse effect on fatigue life, the high-cycle fatigue properties of Al-Li alloys are excellent (92-95). Compared to pure aluminum, the fatigue resistance of binary Al-Li alloys increases with Li content and aging time (Fig. 9), primarily due to strengthing by Li in solid solution, and the growth of ordered δ' precipitates; cold work prior to artificial aging further enhances this effect. Similar results have been reported for binary Mg-Li alloys (93), where increases in fatigue strength and tensile strength are again related.

Although the global strains that cause HCF failures are nominally elastic, plastic strains are experienced locally at microstructural heterogeneities. Metallographic observations on as-quenched Al-1.8 wt.% Li alloy show very fine surface slip bands distributed homogeneously within the grains during the early stages of cycling at high stress levels; these coarsen and assist microcrack nucleation at sharp slip bands or grain boundaries before finally propagating to failure (92). Artificial aging further increases strength and induces greater inhomogeneity in fatigue deformation with increasing δ'-particle size and distribution. Planar dislocation arrays are seen in TEM studies along <110> in the solution-treated condition; similar features are evident in artificially-aged tempers at low cyclic stresses, and dislocation-cell structures are evident at high stress levels. After thermomechanical treatments, Al-Li alloys show greater improvements in fatigue strength due to their higher monotonic strength, coupled with a cell structure that alleviates slip localization and retards crack initiation (92).

Smooth- and notched-specimen stress/lifetime (S/N) fatigue data (at R = 0.1) for commercial Al-Li alloys 2020-T651, 2090-T81, 2091-T8 and 8090 are comparable with results for 7075-T6 and 2124-T351 (95-98) (Fig. 10). Typical endurance strengths of the commercial alloys are roughly 40 to 50% of the tensile strength; stretching prior to aging can lead to further improvements (92,95). However, results on 2091-T8 alloy (96) suggest that undissolved intermetallic constituent particles (rich in Cu, Fe and Mg) can also influence HCF as they are preferential nucleation sites for microcracks. Moreover, the HCF properties of commercial Al-Li alloys are highly anisotropic due to marked deformation textures and pan-cake shaped grain structure that result in strength variations with specimen orientation; in 2090-T83 Al-Li sheet, for example, S/N fatigue lives for the L+45° orientation are significantly lower than for the longitudinal (L) or long-transverse (L-T) orientations, particularly in smooth as opposed to notched samples (67).

Effect of Surface Treatment

Surface treatments using shot peening, ion implantation, nitriding and laser glazing techniques are commonly employed to improve fatigue-crack initiation resistance through the introduction of compressive residual stresses at the surface; work-hardening effects also play a minor role. Studies on peak-aged 8090 (99-101) have confirmed that the HCF resistance of Al-Li alloys can be improved using such techniques. However, crack-initiation lives (defined as the number of cycles required to grow a 100 μm crack) can be shorter in shot-peened compared to untreated specimens, due to early crack nucleation at stress concentrations or fold-like defects generated by the peening; subsequent crack propagation is retarded such that total fatigue lifetimes are improved.

Other treatments, such as acid pickling and anodizing (used as precursors to adhesive bonding and for corrosion protection) can lead to reduced fatigue life due to premature crack nucleation from preferential grain-boundary attack and the rupture of surface oxide films. Recent results (99,101)

indicate, however, that 8090-T8 is less susceptible to problems from chromic/sulfuric acid pickling than Al-Zn-Mg-Cu alloys, because the reduced grain-boundary precipitation decreases the electrochemical driving force for dissolution and crack formation. Moreover, unlike other aluminum alloys, the fatigue strength can be restored by reanodizing the pickled surfaces; an increased fracture strain of the lithium-bearing surface oxide films is presumed to be the principal cause for this behavior (99).

FATIGUE-CRACK PROPAGATION

In recent years, damage-tolerant design procedures have become increasingly important in predicting life and ensuring the durability of many safety-critical structures; the concept presumes that defect populations pre-exist in components and that structural integrity is a function of the number of cycles to propagate the largest undetected flaw to failure (102-104). Lifetimes are conservatively predicted by integration of a relationship describing the crack-growth rate (da/dN) as a function of the mechanical crack-driving force, from initial to final (critical) crack size. For nominally linear-elastic conditions, where the driving force can be defined in terms of the applied stress-intensity range, $\Delta K = K_{max} - K_{min}$ (K_{max} and K_{min} are the maximum and minimum stress intensities), these relationships are generally based on the Paris power-law relation, viz:

$$da/dN = C\,\Delta K^{m}, \qquad (1)$$

where C and m are experimentally determined scaling constants. Although Eq. (1) provides a reasonable description for crack-growth rates in a range typically between $\sim 10^{-9}$ and 10^{-6} m/cycle, it does not adequately characterize behavior at ΔK levels approaching the fatigue threshold, ΔK_{TH}, below which long cracks are presumed dormant, or close to instability, where limit load or catastrophic failure (e.g., at $K_{max} = K_{Ic}$, the fracture toughness) occurs; in these instances, more complex equations are curve-fit to the crack-growth data. Such crack propagation "laws" are generally determined under constant-amplitude loading conditions, using fracture-mechanics type specimen geometries containing pre-existing, long (>5 mm) through-thickness cracks, via manual or computer-controlled load-shedding schemes which reduce ΔK levels at a fixed load ratio ($R = K_{min}/K_{max}$).

In many materials crack-propagation behavior is strongly affected by crack closure, particularly at near-threshold levels (45,105-111); in fact, significant effects of microstructure, load ratio and even environment have been attributed to variations in crack-closure levels. The closure phenomenon is a consequence of the crack not being fully open during the entire loading cycle, even under tension-tension loading conditions, such that premature contact of the crack surfaces occurs at the closure stress intensity, K_{cl} before minimum load is reached. Prominent mechanisms include closure due to residual plastic deformation - plasticity-induced crack closure, interference of fracture-surface asperities between mating

fracture surfaces in the crack wake - roughness-induced crack closure, and wedging of the crack from corrosion or oxide deposits on the fracture surface - oxide-induced crack closure (105-109). The salient mechanisms pertinent to high-strength aluminum alloys and their influence on crack-growth rates are illustrated in Fig. 11; measurement techniques are discussed in refs. 110,111.

Similar to other crack-tip shielding mechanisms (45,46), the role of closure is to perturb the near-tip stress or strain field by lowering the local driving force actually experienced at the crack tip. This driving force can be defined as (45):

$$\Delta K_{eff} = K_{max} - K_{cl} \; ; \qquad (K_{cl} > K_{min}) \, ,$$
$$\Delta K_{eff} = \Delta K \; ; \qquad (K_{cl} < K_{min}) \, . \qquad (2)$$

Where growth rates are correlated in terms of ΔK_{eff}, the crack-growth relationships have been termed intrinsic, i.e., devoid of mechanical crack-closure effects. Alternatively, the intrinsic fatigue-crack propagation resistance can be directly assessed using constant K_{max}/increasing K_{min} (variable R) load-shedding schemes which restrict closure effects (112).

As noted previously, localized planar-slip deformation in δ'-hardened Al-Li alloys has adverse effects on (LCF) crack-initiation resistance; however, paradoxically, it can be beneficial to crack-propagation resistance by inducing crystallographically tortuous crack paths. Such geometrical changes in crack-path morphology promote crack-tip shielding, in particular from the wedging of fracture-surface asperities, and retard crack advance.

Behavior in Experimental Al-Li Alloys and 2020

Early studies on fatigue-crack propagation in Al-Li alloys were performed on Al-3Li-1.25Mn systems (74) and peak-aged 2020-T651 (98) in moist air, where it was found that crack-growth rates, between 10^{-9} and 10^{-5} m/cycle, were significantly slower than in 7075-T6, particularly at low stress-intensity levels. Such observations were attributed to the higher elastic modulus of Al-Li alloys, which results in lower crack tip opening displacement (CTOD) at fixed ΔK and consequently lower crack-growth rates per cycle, although at higher ΔK levels approaching instability, growth rates were faster in the Al-Li alloys. Similar behavior was noted for Al-Li-Mg alloys (113) and rapid-solidification processed (RSP) Al-Li-Cu-Mn alloys (114) and the improved fatigue properties were associated with slip-band cracking; enhanced slip-reversibility due to the planarity of slip from δ'-particle hardening was reasoned to diminish the crack-tip damage (irreversible cyclic plastic strain) accumulated each cycle (114). Residual stresses developed during quenching after solution treatment were also found to have a significant influence on crack growth in RSP materials.

More recently, with the renewed interest in Al-Li systems, the fatigue behavior of peak-aged 2020 alloy has been re-examined over a wider range of growth rates between 10^{-11} and 10^{-6} m/cycle (115). Crack-propagation data under constant-amplitude (variable-ΔK/constant-R = 0.33) and spectrum loading (single tensile overload every 8000 cycles with K_{oL}/K_{max} = 1.8) are compared with corresponding results for 7075-T651 and 7091-T7E69 in Fig. 12 (for an ambient moist air environment). As reported in earlier studies (98), 2020 exhibits significantly slower crack-growth rates, by more than two orders of magnitude at near-threshold levels; however, this cannot be rationalized purely on modulus differences since the improved crack-growth properties of 2020 are apparent even after normalizing growth-rate data with Young's modulus (115). Of more importance here is the fact that crack advance in 2020 is highly crystallographic at all ΔK levels with substantial crack deflection and branching; consequently, fracture surfaces are extremely rough and faceted, with little evidence of ductile striations. In addition, oxide deposits have been detected on these surfaces, with excess oxide thicknesses estimated from secondary-ion mass spectroscopy to be between ~5 and 10 nm.

Based on these observations, the superior fatigue-crack propagation kinetics in Al-Li alloys, specifically 2020, are attributed to the highly nonlinear and tortuous crack-path morphologies. This follows from coherent-particle (δ') hardening in the coarse-grained and textured microstructures which results in marked planar-slip deformation along close-packed {111} slip planes; this in turn promotes cracking along slip bands leading to a crystallographically-faceted mode of crack extension (115-118,123,124). The resulting crack deflection and branching *locally* reduce the Mode I stress intensity at the crack tip and further promote roughness-induced crack closure via wedging of the fracture-surface asperities (facets) in the crack wake. Despite the more heavily oxidized fracture surfaces in 2020 (compared to traditional 2000 series alloys) due to the presence of lithium, additional contributions to crack closure from the wedging of oxide debris are relatively insignificant because the excess oxide thicknesses remain small compared to the CTOD.

Subsequent results on high-purity Al-Li-Cu-Zr alloys, containing controlled variations of Cu and Li (35,119-122), provided further evidence that the superior crack-propagation resistance of Al-Li alloys is associated with crack-tip shielding mechanisms induced by inhomogeneous planar-slip deformation. Increasing the Li/Cu ratio, and hence the amount of δ', was found to enhance crack-path tortuosity, which in turn resulted in lower crack-extension rates and higher fatigue thresholds (Fig. 13). Conversely, δ'-reversion and reprecipitation studies (44) indicate that T_1 plates inhibit planar-slip induced crack deflection, thereby resulting in faster crack-growth rates. Growth-rate behavior was also found to be sensitive to load ratio; alloys with higher Li content showed the strongest effect (119).

Behavior in Advanced Commercial Al-Li Alloys

The design of modern Al-Li alloys has principally focused on homogenizing planar-slip deformation by adding solute elements that form incoherent precipitates and dispersoids; the rationale is to achieve acceptable ductility and toughness. The resulting microstructures are often unrecrystallized and highly textured with a laminated grain structure. Such microstructures can lead to exceptional fatigue-crack propagation resistance in specific orientations, yet concurrently often result in poor short-transverse toughness and fatigue properties (67,123-136).

Crack-growth rate results, as a function of ΔK, are plotted in Fig. 14a for commercial I/M Al-Li alloys, namely peak-aged 2090, 8090, 8091, 2091 and Weldalite (L-T orientation, R = 0.1), and are compared with data on 2124-T351 and 7150-T651 (124,125). Corresponding crack-closure levels, measured using back-face strain compliance methods and plotted as K_{cl} values normalized by K_{max}, are shown in Fig. 14b. Similar to experimental Al-Li-Cu-Zr alloys, the commercial alloys exhibit consistently slower crack velocities over the entire spectrum of growth rates (except compared to 2124-T351 at near-threshold levels). As shown in Fig. 14b, this can be attributed primarily to their higher crack-closure levels which, unlike traditional 2124 and 7150 alloys, remain significant at high stress intensities, e.g., values of K_{cl} in 2090-T81 are 90% of K_{max} (K_{cl} ~ 2 to 3 MPa$\sqrt{m}$) at the threshold ΔK_{TH}, and remain over 50% of K_{max} (K_{cl} ~ 3 to 4 MPa$\sqrt{m}$) at ΔK levels as high as 7-8 MPa$\sqrt{m}$ (124).

Such high crack-closure levels can be associated with highly tortuous and deflected crack paths, specifically for 2090, 8090 and 2091 Al-Li alloys (Fig. 15); fracture-surface morphologies are therefore unusually rough and covered with transgranular facets (97,123-135). At intermediate to high ΔK levels exceeding ~6-8 MPa$\sqrt{m}$, these facets are associated with slip-band cracking along {111} planes; however, at low ΔK levels, "pseudo cleavage" type cracking along {100} or {110} planes has been observed (131-135). In fine-grained 8091, however, which exhibits the lowest closure levels and consequently the fastest growth rates, crack paths are essentially linear; in 2090-T81 conversely, which displays the most deflected crack paths, closure levels are the highest and corresponding growth rates are the slowest (124). This implies that the tortuosity of the crack path provides a major contribution to crack-tip shielding in Al-Li alloys; additional shielding may arise from closure induced by cyclic plasticity (105) and corrosion debris (108,116-120), although the latter mechanism is relatively insignificant (41,133).

Such shielding mechanisms are common to most coherent-particle hardened aluminum alloys, although their influence is generally limited to near-threshold stress-intensity levels (116-118). What is particularly striking about Al-Li alloys is that the predominance of {111} slip-band cracking preserves such high closure levels into the intermediate and high growth-rate regimes (135,136); at near-threshold levels, where {100} or {110} "pseudo cleavage" cracking occurs, behavior in Al-Li alloys is comparable

to conventional Al alloys (132,133). Moreover, since {111} cracking is promoted by strong deformation texture, early vintage 2090 alloys, for example, tend to display the best fatigue-crack growth properties (123). However, the onset and relative proportion of {111} vs. {100} or {110} type crystallographic fatigue cracking modes with respect to ΔK level can change in chloride environments, as discussed below (132,134).

The effect of the higher elastic modulus, which reduces the CTOD, and increased slip reversibility, which reduces the crack-tip damage per cycle, act in concert with mechanisms of crack-tip shielding; however, in light of the high crack-closure levels and observed effects of crack size, load ratio and loading sequence on crack-growth kinetics (as discussed below), the role of shielding appears to be more dominant. In essence, the tortuous crack paths in Al-Li alloys lead to slower (long-crack) growth rates by increasing the path length of the crack, by reducing the local stress-intensity levels due to deflection from the principal stress plane (137), and by reducing the near-tip stress-intensity range by enhancing roughness-induced crack closure due to asperity wedging (106-109) (Fig. 16).

Crack-Path Morphology

As noted above, an essential feature of the fatigue behavior of Al-Li alloys is the shearable nature of δ' strengthening precipitates, which results in inhomogeneous (planar-slip) deformation and unusually tortuous crack-path morphologies. The nature of the deflected crack paths takes several forms, as shown in Fig. 17: the crack may undergo macroscopic branching, where the entire crack deflects at some angle to the principal stress plane due to deformation texture; alternatively, crack growth may be faceted ("zig-zagged") from crystallographic deflection at boundaries due to the marked planarity of slip, or cracks may undergo (intergranular) short-transverse delamination due to the unrecrystallized, anisotropic "laminated" grain structure (123).

Additionally, pronounced deformation textures in Al-Li alloys promote deflection along the crack front. This is illustrated in Fig. 18 by a metallographic section of a fatigue fracture surface in 2090-T81, taken across the specimen thickness perpendicular to the crack plane and crack-growth direction; the crack front is highly deflected and faceted, with apparent secondary crack branching beneath the surface. Texture analysis shows that the crystallographic facets (with an included angle of $\sim 60°$) result from a change in slip-plane orientation between two components of the $\{110\}<112>$ deformation texture, resulting in cracking along two sets of intersecting {111} slip bands (61,62). However, precise modeling of the {111} slip-band cracking mechanism occurring along planes with the highest-resolved deviatoric stress is currently lacking. Combined with small Mode III shear displacements, this cracking morphology promotes roughness-induced closure through the specimen thickness, in addition to Mode II shear induced wedging of asperities along the crack-growth direction. The crystallographic facets, however, become less sharp (the included angle approaches 180°) close to

the specimen surface, consistent with the through-thickness variations in textural components for wrought Al-Li alloys (62).

Microstructural Effects

The influence of microstructure on fatigue-crack growth in Al-Li alloys is essentially not unlike other precipitation-strengthened aluminum alloys. Resistance to crack growth is generally superior in underaged structures, because the marked planarity of slip from coherent (shearable) precipitate distributions promotes deflected crack paths and hence high closure levels (35,119-126). With artificial aging, deformation becomes more homogeneous concurrent with loss of coherency of the precipitates; crack-growth resistance is now diminished somewhat as the degree of slip-reversibility, crack-path tortuosity and resulting crack-closure levels all are reduced. In Al-Li alloys, however, δ' precipitates remain coherent up to large particle diameters; superior fatigue-crack propagation resistance can be maintained in coarse-grained microstructures even in peak-aged tempers, provided grain-boundary precipitation and associated PFZ formation are largely suppressed (122-126).

The close correlation between optimum crack-growth resistance and high closure levels in Al-Li alloys, as illustrated by the T8 tempers of 2090, 8090, 8091 and 2091 in Figs. 14 and 15, implies that if (long-crack) growth rates are compared as a function of ΔK_{eff} (after correcting for closure), behavioral differences with respect to microstructure and alloy composition will be less apparent (Fig. 19). This notion (124) is corroborated by a comparison of growth rates determined under constant-K_{max}/variable-R loading conditions* (Fig. 20). Al-Li-Cu alloys now exhibit similar growth-rate behavior to 2000 series

*Constant K_{max}/increasing K_{min} procedures permit an estimation of the intrinsic crack-growth behavior by minimizing closure effects due to crack wedging. As such, they result in crack-growth data similar to that characterized in terms of ΔK_{eff}. However, these techniques do not evaluate the influence of any other shielding mechanisms, such as crack deflection or bridging, and moreover, require prior knowledge of the variation in K_{cl} with ΔK level and R.

series aluminum alloys, although faster growth rates are observed for 7000 series alloys, presumably due to their increased environmental sensitivity (133-135).

This should not be construed as an indication that microstructure and alloy composition are unimportant to fatigue-crack propagation in Al-Li alloys since the microstructure clearly affects crack deflection, which in turn influences closure. In fact, coherent δ'-particle strengthening, strong deformation textures, coarse and unrecrystallized (elongated) grain structures, absence of heterogeneous grain-boundary precipitation and PFZs can all be identified as the prominent microstructural sources of crack deflection and branching.

Load-Ratio Effects

It is well known that increasing the load ratio at a specific stress-intensity range can lead to faster fatigue-crack propagation rates and lower fatigue thresholds. At near-threshold levels, the effect is primarily associated with a diminished role of crack closure induced by wedging mechanisms from the larger CODs at high mean stresses. In Al-Li alloys, growth rates (plotted as a function of ΔK) are particularly sensitive to the load ratio because closure levels are exceptionally high (119-126); however, by plotting as a function of ΔK_{eff}, after allowing for closure, the effect of load ratio becomes less apparent (Fig. 21). Moreover, due to this limited role of closure at high load ratios, the superior (long-crack) fatigue-crack growth properties of Al-Li alloys are less evident at high R (124,133-135). Similarly, as shown in Fig. 20, if growth rates in Al-Li alloys are measured under constant-K_{max}/variable-R conditions which minimize crack closure, behavior is equivalent to that obtained for 2000 series alloys (133-135). The superiority of Al-Li alloys can also be compromised under completely-reversed or tension-compression loading ($R < 0$) conditions, where the compressive cycles can similarly act to limit closure by crushing fracture-surface asperities (136).

Plate-Orientation Effects

As fatigue-crack growth rates in Al-Li alloys are a strong function of crack-path morphology, behavior in commercially rolled sheet and plate products is strongly anisotropic (62,66,67,123,138), both in the rolling plane and through the thickness. Growth rates for long cracks (at fixed ΔK) in 13-mm-thick 2090-T81 rolled plate can vary by up to four orders of magnitude between various orientations, concomitant with large differences in measured crack-closure levels (123) (Fig. 22). Specimen orientations in the rolling plane, namely L-T and T-L, develop the highest closure levels from highly deflected transgranular crack-path morphologies (K_{cl} values approach 90% of K_{max}); these orientations correspondingly show the slowest growth rates and highest thresholds ($\sim$3-4 MPa$\sqrt{m}$). Similarly, crack-growth resistance is high for the T-S orientation where crack growth is often deflected through $\sim 90°$ by delamination along weakened short-transverse grain boundaries (66,123). However, intrinsic crack-growth rates for the L-T, T-L and T-S orientations are all identical as the mechanism of crack propagation remains essentially transgranular (131-133); differences are associated with the variations in shielding. Conversely, crack paths for the S-L and S-T orientations are highly linear and involve delamination along grain boundaries, often weakened by the presence of Fe- and Cu-rich intermetallics, δ'-PFZs, and possible Li, Na or K segregation; growth rates in these orientations are accordingly far faster than for the L-T, T-L and T-S orientations (123).

In addition to the short-transverse orientations, the L+45° (LT-TL) orientation also shows high growth rates (66,67,123) and low thresholds (ΔK_{TH} = 2.4 MPa$\sqrt{m}$), behavior which appears to be

associated with pronounced deformation texture in wrought products. Slip-band cracking is favored along close-packed {111} planes which are aligned closer to the principal stress plane in the L+45° configuration; consequently, crack paths show a lower tendency for deflection and meandering (123). Fatigue-crack mechanisms in the L+45° orientation have not been fully examined, although reduced modulus (~6%) and lower strength (~16%) in this configuration can additionally contribute to faster crack growth rates.

Fatigue-crack growth rates in Al-Li alloys also tend to be substantially slower (at fixed ΔK) in the mid-thickness locations of wrought thick-section plate compared to the surface regions (62,66), again, associated with marked variations in grain structure and crystallographic texture. For example, in 2090-T81 plate, surface regions are often partially recrystallized and grains exhibit a weak {001}<110> texture; conversely, at mid-thickness, the microstructure remains unrecrystallized with strong "brass", "copper" and weak "S" type texture components. Since the growth-rate kinetics are a strong function of crack-path tortuosity, which is promoted by unrecrystallized and textured microstructures, growth rates are retarded at mid-thickness locations by the increased effect of crack closure (62).

Small-Crack Effects

Current design methodologies often compute the lifetimes of structural components in terms of the cycles to propagate a pre-existing flaw to failure through integration of experimental crack-growth relationships (e.g., Eq. 1) derived from standard specimen geometries containing "long cracks", typically in excess of 5 to 10 mm in size. Although presumed to be conservative, this approach can potentially overestimate lifetimes in the presence of "small cracks", which are small compared to microstructural dimensions or the plastic-zone size, or are simply physically small (i.e., < 1 mm);* such cracks are

*Mechanistically, a crack is considered "small" when its size is less than, or comparable to, the size of the steady-state shielding zone in the wake of the crack tip.

known to propagate faster than long cracks at equivalent stress-intensity levels, in part owing to a restricted role of crack-tip shielding (e.g., crack closure) with cracks of limited wake (139-141). This effect has particular significance for Al-Li alloys because their superior (long-crack) fatigue-crack growth resistance arises primarily from (roughness-induced) crack closure, a phenomenon which is strongly crack-size dependent.

Small-crack behavior is generally characterized by monitoring the early growth of naturally-occurring surface flaws (typically in the range 2 to 1000 μm in size) in unnotched bend or tension samples using optical, replication or electrical-potential techniques (see ref. 141 for details). Using such procedures, studies in commercial Al-Li alloys 2090, 2091, 8090 and 8091 have indicated that small

cracks initiate along slip bands, predominantly at cracked Fe- or Cu-rich inclusions or constituent particles on the surface, polishing pits and uncracked matrix/particle interfaces (124,142-149). During early stages of small-crack growth, fracture surfaces exhibit large "cleavage-like" features (143), resembling those observed at near-threshold ΔK levels for long cracks. Subsequent crack advance is marked by frequent deflection of the crack path at intersecting slip bands and high-angle grain boundaries (Fig. 23) (142,143,149). At higher cyclic stress levels, several cracks may nucleate along coarsened slip bands, which tend link up rapidly to form a network (143).

The growth-rate response of such microcracks is compared with conventional long-crack data in Fig. 24, as a function of ΔK (the use of K here is considered appropriate as computed maximum and cyclic plastic-zone sizes remain small (typically 4%) compared to crack size). Despite the large scatter in experimental results, it is clearly apparent that small cracks propagate at rates as much as 2-3 orders of magnitude faster than long cracks at equivalent applied stress-intensity levels (142,149); however, uncertainties do exist in the computation of ΔK for small cracks, due to the stress-concentrating effect of nucleating cracks near inclusions and due to irregular crack geometries (139-141). Nevertheless, small-crack growth is observed at ΔK levels as low as 0.8 MPa$\sqrt{m}$, far below the threshold ΔK_{TH} for long cracks (142-149).

A major reason for the discrepancy between long- and small-crack behavior is the restricted crack-tip shielding associated with flaws of limited wake (142-150). Since shielding mechanisms act primarily on the crack wake, small cracks generally are unable to develop the same degree of closure as a crack of a length larger than the equilibrium shielding zone (where for example fracture-surface asperity contact is achieved); thus, at the same nominal ΔK, the small crack may experience a larger *local* stress intensity and hence extend at a faster rate. In fact, *in-situ* compliance measurements in 8090 and 2090 confirm that closure levels for small cracks are smaller than for corresponding long cracks (143,145). Accordingly, if long- and small-crack results are characterized in terms of ΔK_{eff} (after correcting for closure), or if long-crack growth rates are evaluated using constant-K_{max}/variable-R procedures (which minimize the closure effect), the resulting data display a much closer correspondence, as shown for 2090 in Fig. 24. With increasing crack size, an equilibrium shielding zone is established in the crack wake, such that closure levels are similar, and small-crack and long-crack data merge (even when characterized in terms of ΔK); in commercial Al-Li alloys, this occurs typically at crack sizes above $\sim$700-1000 μm and nominal ΔK levels above $\sim$7 MPa$\sqrt{m}$ (142,144). However, it should be noted that there is not a perfect match between long and small crack data at near-threshold levels. This may result from scatter, uncertainties in ΔK computation, and/or the fact that naturally-occurring small cracks initiate at local heterogeneities in the microstructure which are not necessarily simulated in a long-crack test involving a pre-existing flaw and artificial load-shedding schemes.

In contrast to long-crack results where microstructural effects strongly influence crack-growth behavior (Figs. 12-14), a minimal influence of alloy chemistry and microstructure is apparent for small

cracks in Al-Li alloys (124,133,135,149); in fact, despite extensive scatter, their small-crack behavior is comparable to traditional alloys (124,148,149) (Fig. 25). This implies that the salient role of microstructure during fatigue-crack propagation in these alloys occurs principally through the development of crack-tip shielding (crack deflection and closure). This is consistent with the fact that microstructural effects become less evident where the shielding effects are suppressed, i.e., at high load ratios, with small cracks, or where results are characterized in terms of ΔK_{eff} or using constant-K_{max}/variable-R procedures (150). Accordingly, in contrast to long-crack behavior, it is to be expected, and indeed is the case, that small-crack growth rates are relatively insensitive to load ratio and specimen orientation (133,142,149). However, since the long-crack behavior of Al-Li alloys is in general superior to conventional aluminum alloys (due primarily to extensive shielding), differences between long- and small-crack results are most significant in these materials. Thus, Al-Li alloys can be considered to display the best long-crack properties of all high-strength aluminum alloys yet, *by comparison*, the worst small-crack properties, paradoxically for the same reason - crack-tip shielding (149).

BEHAVIOR UNDER VARIABLE-AMPLITUDE LOADING

The design and selection of materials for aircraft structures is increasingly based on fatigue-crack growth response under complex loading spectra which simulate in-service operating conditions. This is particularly important since the fatigue performance of a material can widely vary with the specific nature of these spectra. For example, tensile overload cycles of sufficient magnitude can act to retard crack growth and hence prolong fatigue life; compression overloads on the other hand tend to diminish this effect. The behavior of Al-Li alloys in this regard is discussed below.

Influence of Tensile Overloads

Experiments to examine the role of single tensile overloads are generally performed on fatigue cracks propagating under constant ΔK conditions by monitoring the transient crack-growth response, after resuming cycling at baseline stress-intensity levels. Typical data for 2090-T81, showing the effect of 50, 100 and 150% single tensile overloads on crack-propagation rates at a constant baseline ΔK of 8 MPa$\sqrt{m}$, are plotted in Fig. 26 (151). It is evident that 50% overloads have little effect; overloads of higher magnitude, however, result in an immediate acceleration followed by a period of prolonged retardation before growth rates return to baseline levels. The extent of the delay increases with the magnitude of the overload, and at near-threshold levels can completely arrest crack advance (151).

Mechanistically, studies on Al-Li and titanium alloys (151-154) have indicated that the post-overload retardation is associated with residual compressive stresses in the overload plastic zone, and

with crack closure which results in the immediate vicinity of the crack-tip as the crack grows into the zone; this effect is enhanced by lower CTODs in the overload zone which promote wedging of the mating fracture surfaces. Crack deflection and branching along flow bands (Fig. 27), although predominantly a surface effect, may also contribute to the delay (151).

Because Al-Li alloys develop such high shielding levels, they generally show a greater degree of post-overload retardation than traditional aluminum alloys (98,119,151-156). Behavior is illustrated in Fig. 28a, where fatigue-crack extension following an 80% tensile overload is plotted as a function of the number of cycles for three experimental Al-Li-Cu-Zr and 7075-T6 alloys (119). Although the Al-Li alloys with low Li:Cu ratio show only marginally increased delays compared to 7075, alloys with higher Li:Cu ratio clearly exhibit far superior variable-amplitude fatigue-crack propagation resistance. Mechanistically, the large improvement in variable-amplitude fatigue properties with increasing lithium content is consistent with the larger volume fraction of δ' precipitates in these microstructures; this induces crystallographic crack growth which in turn promotes crack deflection and roughness-induced closure. Similar crack-growth and crack-closure behavioral trends have been reported (151) for commercial 2090-T81 Al-Li alloy when compared with traditional 2124-T351 and 7150-T651 alloys (Figs. 28b,c).

Compression Overloads

Although compressive overloads are commonly experienced by numerous aircraft components in service, their influence on fatigue-crack propagation has received surprisingly little attention. As the crack is presumed to remain closed during the negative portion of the loading cycle, the effect of compression cycles has long been considered minimal. Recent results on high-strength steels, Al and Al-Li alloys, however, have indicated that periodic compression overloads can significantly accelerate near-threshold crack-growth rates, specifically by reinitiating the growth of long fatigue cracks previously arrested at ΔK_{TH}, or by reducing the fatigue threshold (136,157,158). This behavior has been associated with diminished levels of crack-tip shielding, resulting from a reduction in residual compressive stresses in the cyclic plastic zone and, more importantly, from the compaction of the fracture-surface asperities during the overload cycle. In view of their increased dependence on crack deflection and asperity-wedging closure mechanisms, Al-Li alloys are far more sensitive to compressive overloads than traditional Al alloys; for example, it takes 400-500% compressive overloads to reinitiate the growth of arrested fatigue cracks in traditional 2124 and 7150 alloys, whereas a mere 200% overload is sufficient to cause the same effect in Al-Li alloy 2090-T81 (136).

Spectrum loading

Comprehensive studies at Northrop (159,160) on the spectrum fatigue resistance of several 2000 and 7000 series aluminum alloys and experimental Al-Li alloys provide further corroboration of the differing response of Al-Li alloys to tension and compression overloads. Specifically, where behavior was compared for two load spectra, dominated by either tension overloads (TD)* or by tension and compression overloads of approximately equal magnitude (TC)*, Al-Li alloys can show a nearly five-fold

*These spectra represent, respectively, the lower root-wing and horizontal tail-hinge moment load histories of the F-18 fighter.

improvements in spectrum-fatigue lives compared to 2024 and 7050 under TD loading, consistent with the large crack-growth retardations observed following the tensile overloads (Fig. 29). However, alloys with the highest fatigue lives under such TD spectra also show the largest differences between TD and TC spectra, consistent with the diminished role of shielding following compression cycles. In fact, using a modified TC spectrum which eliminates all compressive loads (TCZ), the spectrum fatigue life of all alloys was increased relative to either TD or TC spectra. For example, an underaged Al-3Cu-2Li-0.12Zr alloy, which exhibited lifetimes greater than 100,000 flight hours under the TD spectrum, showed lifetimes less than 25,000 flight hours under the TC spectrum, a mere 25% of the TD life; under the modified TCZ spectrum, life was increased to nearly 110,000 flight hours (160).

It is clear that similar to behavior under constant-amplitude loading, microstructures that promote shielding, i.e., coarse-grained unrecrystallized and underaged coherent-particle hardened structures that deform by planar slip and induce deflected crack paths, are preferred for optimal performance under variable-amplitude loading conditions.

POWDER-METALLURGY ALLOYS

In addition to the I/M alloys discussed so far, several promising Al-Li alloys have been processed by powder metallurgy. The P/M route offers flexibility in developing alloys with unique compositions and homogeneous microstructures, via such techniques as rapid solidification and mechanical alloying (161-166), as problems of segregation encountered during casting largely confine the chemical compositions of I/M alloys to the maximum solid-solubility of the alloying elements in aluminum. With P/M techniques, Al-Li alloys can potentially be developed with further reduced density, improved strength and stiffness by incorporating higher Li contents exceeding 3 wt.%. In addition, elevated-temperature characteristics of Al-Li alloys can be improved by alloying with large concentrations of transition or rare earth elements, such as Zr, Hf, Ti, Ce or Co. The latter approach, which utilizes dispersion hardening for resisting dislocation motion, is also the most effective means of

reducing planarity of slip, and hence in improving the ductility and toughness of Al-Li forgings and extrusions, since pre-aging stretching procedures are not feasible for these product forms.

Prominent among the experimental P/M alloys are rapid-solidification processed (RSP) Al-3.0Li-0.9Cu-0.4Mg-0.4Zr alloy 644-B, developed by Allied-Signal, and the mechanically-alloyed (MA) Al-1.5Li-4Mg alloy IN-905XL, developed by Inco Alloys Intl. The latter alloy also contains substantial amounts of carbon and oxygen in the form of oxide (Al_2O_3) and carbide (Al_4C_3) dispersions, which are formed during ball milling of elemental powders; carbon is added as an organic agent to prevent agglomeration. Microstructural details and mechanical properties are summarized in Tables II-V.

Such near-commercial P/M alloys have roughly 10% lower density than traditional 7075-type alloys, and often exhibit far higher strength with moderate ductility and fracture toughness. The HCF and LCF resistance of mechanically-alloyed P/M extrusions is generally superior to corresponding I/M alloys (87,167) because of the more homogeneous mode of deformation in P/M alloys. Moreover, no change in deformation mode is observed for P/M Al-Li alloys between the high- and low-strain amplitudes consistent with the observation of a single slope on the Coffin-Manson plot (87). However, crack-propagation properties are invariably inferior to I/M alloys (Fig. 30a); fatigue-crack growth thresholds are generally lower and crack-propagation rates up to one or two orders of magnitude faster (168-171). The prime reason for this can be traced to a limited role of crack-tip shielding. Essentially, the fine microstructures (grain size typically below 5 μm) and more homogeneous deformation of MA Al-Li alloys, which results from dispersion hardening by oxides and carbides rather than by ordered δ' precipitates (Li remains in solid solution), yields unusually linear crack profiles and exceptionally smooth fracture surfaces (Figs. 31a,b), with little sign of slip-band cracking (170,171). As a result, MA microstructures, unlike coarser-grained I/M alloys, do not develop high shielding levels from deflection and related crack-wedging closure mechanisms; in fact, measured K_{cl} values at near-threshold levels are a mere 35% of K_{max} in the Al-Li-Mg 905-XL alloy, compared to a corresponding figure of ~90% of K_{max} in I/M alloys (Fig. 30b). The beneficial effects of lithium on fatigue-crack growth are thus not so apparent in mechanically-alloyed Al-Li systems (170).

RSP processing, conversely, can lead to better fatigue resistance for P/M alloys compared to MA microstructures (170). For example, the crack-growth and closure properties of RSP 644-B extrusions are comparable with I/M 2090-T81 plate, particularly at lower ΔK levels ($\lesssim 10$ MPa$\sqrt{m}$). Similar to I/M Al-Li alloys, the superior behavior of RSP alloys can be attributed primarily to factors that favor planar-slip deformation, namely, precipitation hardening by shearable δ' particles and the presence of β' dispersoids that inhibit recrystallization and impart preferred grain orientations (170). Accordingly, fractographic features in the RSP 644-B alloy resemble those seen in I/M Al-Li alloys; crack paths are highly deflected with rough transgranular fracture surfaces showing 3-4 μm sized facets and evidence of local slip-band cracking (Figs. 31c,d). In fact, the RSP Al-Li alloy displays superior crack-growth properties to most traditional RSP P/M aluminum alloys (162,170).

In accordance with these arguments, crack-growth rates and fatigue thresholds in MA alloys are often found to be less sensitive to load ratio (169,170,172), loading sequence (170), specimen orientation (170), specimen geometry (169) and crack-size (173) due to the limited extent of shielding. For example, nominal ΔK_{TH} values in IN-905XL are equivalent to $\Delta K_{eff,TH}$ and are independent of load ratio for either tension-tension or tension-compression cycling. Similarly, growth rates are similar for small surface cracks (<1 mm) and long through-thickness cracks in these alloys; in actuality, small cracks have been reported to propagate slower (173). Conversely, faceted crack growth, tortuous crack paths and high closure levels are all prominent in the RSP 644-B alloy, such that crack-growth behavior in this material becomes sensitive to load ratio and specimen orientation (170).

ELEVATED-TEMPERATURE PROPERTIES

The use of aluminum alloys at moderately elevated temperatures (350 to 450 K) in advanced aerospace applications can be limited by severe overaging which degrades strength, toughness and fatigue resistance. Accordingly, there has been a considerable motivation to develop higher temperature alloys, such as the Al-Fe-V-Si, Al-Fe-Ce and Al-Fe-Co systems, to replace the more expensive titanium alloys for aerospace applications above 400 K. Naturally, there has been much interest in using ultra-low density Al-Li alloys for such applications as well.

Results to date on the elevated-temperature performance of Al-Li alloys suggest that despite a loss in properties from overaging, behavior is generally superior to traditional aluminum alloys (95,98,167,174). Specifically, the crack-initiation resistance of 2020-T651, 8090 and IN-905XL alloys has been found to be relatively stable up to temperatures of $\sim$450 K; mean values of the HCF strength for 2020 and 905-XL are above the scatter band for 7075-T6 (98,167). This improved thermal stability is presumed to result from slower coarsening kinetics of strengthening precipitates and dispersoids in these alloys (98). However, stretching prior to aging can diminish the high-temperature fatigue resistance; for example, the endurance strength of 8090 has been found to decrease at higher temperatures due to dynamic recovery in the cold-worked (stretched) material (95). In addition, localized oxidation and grain-boundary embrittlement at elevated temperatures can contribute to reductions in LCF resistance, particularly at low strain amplitudes (82).

Following prolonged exposures to high temperatures of up to 1000 h at 436 K, peak-aged 2090 and 8090 Al-Li alloys have been shown to suffer only marginal reductions ($\sim$15%) in strength and toughness (174-176), even though such temperature excursions lead to grain-boundary precipitation, an increase in the width of δ'-PFZs, and coarsening of matrix precipitates. However, 1000 h exposures at 533 K can lead to drastic reductions in strength, similar to behavior in 2124-T3, 7075-T6 and 2219-T8 aluminum alloys (175,176). Fatigue-crack growth resistance in Al-Li alloys can also be degraded by high-temperature exposure, as crack paths become more linear leading to diminished crack-tip shielding

and enhanced crack-growth rates (174,175). The increase in growth rates, however, is confined to high ΔK levels (where crack velocities exceed $\sim 10^{-9}$ m/cycle); near-threshold behavior is generally unchanged. Yet, the fatigue properties of thermally exposed Al-Li alloys are still comparable to traditional 2124-T351, 7150-T6 and 7150-T7 alloys (Fig. 32).

ENVIRONMENTAL EFFECTS

Environments such as moist air, water vapor and aqueous halide solutions are known to accelerate crack-propagation rates in most 2000 and 7000 series aluminum alloys under both monotonic and cyclic loading (177-199). For example, high-strength aluminum alloys, including Al-Li alloys, are susceptible to intergranular stress-corrosion cracking (SCC) under monotonic loading, particularly in the short-transverse (S-T, S-L) orientations (187-191). Under cyclic loads, environmentally-assisted crack growth may be observed at stress intensities either above or below the sustained-load threshold for environmentally-assisted cracking (K_{Iscc}). In the latter case, environmental damage mechanisms are associated with the synergistic effects of plastic deformation and chemical/electrochemical reactions (131-133,177-186).

Because of the highly reactive nature of lithium, Al-Li alloys are often incorrectly perceived to be more sensitive to corrosive environments than traditional aluminum alloys. However, in many respects Al-Li-Cu alloys behave like 2000 series alloys, and are superior to 7000 series alloys, in moist air, water vapor and aqueous chloride environments (131-135,186).

Behavior in Gaseous Environments

Akin to 2000 and 7000 series alloys, water vapor accelerates fatigue-crack propagation rates in Al-Li alloys (131-133,178,179), as shown for 2090-T81 in Fig. 33 (crack-closure effects were minimized in these data by measuring growth rates using constant-K_{max}/variable-R techniques or with physically-short (< 1 mm) cracks (133)). At equivalent ΔK levels, crack-growth rates in pure water vapor are comparable to those in moist air, but are accelerated relative to behavior in pure helium, oxygen and vacuum. Crack velocities are independent of water-vapor pressure for p_{H2O} above $\sim$0.2 Pa (at a frequency of 5 Hz); below this "saturation pressure", growth rates decrease with decreasing partial pressure to approach inert-environment crack velocities. Environmental effects are most pronounced at near-threshold levels and diminish with increasing ΔK, showing a plateau behavior coincident with the transition; in both regimes, growth rates display a ΔK^4 power-law relationship (131).

In common to other high-strength aluminum alloys, hydrogen embrittlement has been suggested as the prime mechanism of crack-tip damage involved in the accelerated cracking of Al-Li alloys in moist air relative to vacuum (131,178-180,185). Mechanistically, this occurs in gaseous and aqueous

environments which produce atomic hydrogen via reaction with fresh metal surface exposed at the crack tip by the cyclic deformation. Hydrogen is then adsorbed and transported into the plastic zone ahead of the crack tip by diffusion or moving dislocations (178), leading to faster crack-growth rates; cracking may be further aided by reduced slip reversibility in the presence of aggressive environment (35). Because nearly identical crack-growth rates are observed in oxygen and inert environments (Fig. 33), neither oxygen nor oxide-film formation on crack surfaces is considered to influence the morphology and reversibility of plastic deformation (131). Moreover, the measured dependence of growth rates on H_2O partial pressure and dependence of "saturation pressure" on load ratio and frequency are consistent with an impeded molecular transport model of hydrogen embrittlement (131,179).

Fractographically, the embrittlement is reflected in differences in the crack-path morphology. In inert environments, fatigue cracking in Al-Li alloys proceeds along intersecting {111} slip planes, particularly at moderate to high ΔK levels exceeding ~ 6 MPa$\sqrt{m}$ (133,185), resulting in large crystallographic facets and unusually rough fracture surfaces (Fig. 18). Conversely, a flat transgranular cracking morphology (resembling cleavage) along {100} or {110} planes, combined with regions of faceted slip-band cracking within subgrains is seen at near-threshold levels. Hydrogen environments, on the other hand, lead to increased inter-subboundary cracking at high ΔKs (131-133), and promote the cleavage-like cracking at progressively higher ΔK levels (130-132), both factors that enhance crack-growth rates; no evidence for ductile or brittle striations has been reported in Al-Li alloys.

Apart from the intrinsic damage mechanisms described above, many extrinsic factors can affect environmentally-assisted cracking in Al-Li alloys. For example, *in vacuo* testing can result in more tortuous crack paths with extensive faceting compared to laboratory air, possibly due to the greater ease of reversible slip in inert environments (35). Additionally, the presence of corrosion products on crack surfaces can promote (oxide-induced) crack closure and retard crack advance, particularly at near-threshold stress-intensity levels (108,115). However, limited studies (123) show that the role of such oxidation debris in commercial Al-Li alloys is generally minimal (at least in moist air environments), as experimentally measured oxide thicknesses are considerably smaller than the relevant crack-tip opening displacements (123). Results of Al-Li-Cu alloys in gaseous oxygen and saline environments, on the other hand, suggest oxide-induced closure effects may be important (133).

Behavior in Aqueous Chloride Environments

Al-Li alloys are particularly susceptible to accelerated fatigue-crack propagation in aqueous chloride solutions (131,177-186). Typical growth-rate data for commercial 2090 and 8090 Al-Li alloys in 3.5 % aqueous NaCl (measured using conventional load-shedding schemes at R = 0.1) are illustrated in Fig. 34. Crack velocities in 2090-T81 are typically one to three orders of magnitude faster in salt water compared to moist air at low stress intensities, with a $\sim 50\%$ reduction in fatigue threshold. The

acceleration in growth rates has been proposed to result from a diminished contribution from roughness-induced closure, arising from the combined action of corrosive attack and mechanical fretting in flattening fracture-surface asperities (185). Alternatively, the reduced faceting and closure may result from an intrinsic change in cracking mechanism in chloride environments (133). However, at equivalent ΔK levels, growth rates in the Al-Li alloys in sea water environments are still an order of magnitude slower than in 7075-T6 (Fig. 34). Studies on the role of microstructure in influencing corrosion-fatigue of Al-Li alloys in chloride solutions are scarce; limited results suggest that overaging does not significantly lower fatigue resistance as crack paths remain predominantly transgranular (192).

More detailed studies (131-133) on the intrinsic fatigue-crack growth kinetics show that aqueous NaCl environments accelerate crack propagation in Al-Li alloys under both anodic and cathodic polarization (Fig. 35). The magnitude of the effect is a function of frequency and Li_2CO_3 additions, and is most pronounced at near-threshold levels under anodic polarization; in 2090-T81 for example, growth rates are almost two orders of magnitude faster than in inert or water-vapor containing environments. In contrast, cathodic potentials reduce fatigue-crack growth rates in 2090 to levels approaching those observed in moist air, similar to other aluminum alloys (177,181). In addition, passivating ions (0.4% Li_2CO_3) can also retard crack-growth rates in NaCl (Fig. 35) by forming a protective film on the crack surface (131,186).

Mechanistically, the intrinsic environmental damage of Al-Li alloys in aqueous NaCl environments is associated with combined effects of hydrogen and surface films (131,186). Cathodic polarization studies are not conclusive in ruling out hydrogen-embrittlement mechanisms because interpretations are complicated by lack of knowledge regarding the crack-tip solution chemistry (131,178). The observed effect of frequency on crack-growth rates, however, does strongly suggest an active role of surface films. In most 7000 series aluminum alloys (at ΔK levels of $\sim$5-8 MPa$\sqrt{m}$), decreasing frequency results in increasing growth rates (193-198); hydrogen-embrittlement models generally relate this to enhanced surface reactions or mass transport during the longer time period of the cycle. Fatigue-crack propagation rates in 2090-T81, conversely, decrease by a factor of two as the frequency is reduced from 5 to 0.1 Hz at ΔK levels $\sim$10 MPa$\sqrt{m}$ or above, although little effect of frequency is apparent close to ΔK_{TH} (131,192). Based on these observations, it has been suggested that mass transport is not the rate-limiting step in Al-Li alloys; rather, increased crack-tip strain rates at higher frequencies are reasoned to destabilize (protective) surface films, resulting in enhanced anodic dissolution or crack advance by film rupture. This effect may be coupled with time-based hydrogen production and entry into the metal (131,178).

Fracture surfaces in NaCl and moist air environments are nominally similar although, due to the more aggressive nature of salt water, a greater degree of inter-subgrain boundary fracture and reduced slip-band cracking is seen at high ΔK levels (132-134). At low ΔK levels, on the other hand, the crystallographic fracture morphology resembling transgranular cleavage is more prevalent in NaCl than

in moist air environments. The associated reduction in crack-path tortuosity due to an environmentally-induced change from faceted slip-band cracking in benign environments to relatively linear inter subgranular and {100} or {110} type cracking may be the prime cause of the lower closure levels measured in conventional corrosion fatigue tests (185).

Unlike behavior reported for steels (178,197,198) where local crack-tip electrochemistry effects greatly enhance environmental effects when crack sizes are small ($\sim$150 μm to 5 mm), the corrosion-fatigue behavior of short cracks ($\sim$300 μm to 4 mm) in Al-Li alloys is essentially identical to that of long (>5 mm) cracks (131,133). In fact in 2090-T81 alloy, K-based similitude adequately describes the growth kinetics of fatigue cracks for all crack sizes above 300 μm in length.

In summary, it may be concluded that the intrinsic fatigue-crack growth resistance of Al-Li alloys in moist air and sea water environments is comparable to 2000 series alloys and in fact superior to 7000 series alloys (131-135,178) (Figs. 20,35). In addition, limited studies indicate that Al-Li alloys show superior crack initiation and S/N fatigue resistance in these environments, at least compared to 7075-type alloys, a fact attributed to their reduced susceptibility to hydrogen absorption and hydrogen-assisted intergranular fracture (182-184).

CRYOGENIC PROPERTIES

The cryogenic properties of Al-Li alloys have recently been the focus of much attention following reports that indicated remarkable improvements in their strength, ductility and fracture toughness at liquid-nitrogen (77 K) and liquid-helium (4 K) temperatures compared to room temperature (38-42). Specifically, studies for the L and L-T orientations on 2090-T81 alloy plate showed a 45% increase in strength, 67% increase in tensile elongation, 12% increase in modulus, and most importantly 90% increase in fracture toughness between 298 K and 4 K*. These properties combined with lower

*The dramatic improvements in toughness at cryogenic temperatures are not, however, typical of all Al-Li microstructures or product forms; thin-sheet Al-Li alloys, such as 2090-T83 for example, may actually exhibit lower toughness with decrease in temperature (199,200).

specific modulus and superior fatigue resistance have made Al-Li alloys very attractive for many cryogenic structural applications; these include liquid-hydrogen and liquid-oxygen fuel tanks on future hypersonic and transatmospheric aerospace vehicles, supporting structures for magnets in particle accelerators, and high-energy fusion devices.

Similar to many high-strength aluminum alloys, the HCF resistance of Al-Li alloys is substantially improved at cryogenic temperatures (201-203). For example, the smooth-bar axial fatigue strength of 2090-T81 (at a life of 10^5 cycles, R = 0.1) increases from $\sim$290 MPa at 298 K to $\sim$700 MPa at 4 K ($\sim$90% of the tensile strength), behavior which is second only to 7075-T6; in

addition, the Al-Li alloy is less notch sensitive (201). Studies on the Al-Li-Cu-Mg-Zr system (203) indicate similar trends, and further show that although the fatigue strength at 298 K can be improved by increasing the Zr content, the temperature dependence of fatigue strength is compromised.

Although data are limited, fatigue-crack growth rates in Al-Li alloys such as 2090 show a decrease at lower temperatures, typical of pure aluminum and many aluminum alloys (38,204-206). Moreover, the properties are comparable to traditional aluminum alloys at cryogenic temperatures (Fig. 36). The generally improved fatigue resistance of aluminum alloys at cryogenic temperatures has been attributed to an elevation in the monotonic or cyclic yield strength, which in turn increases the plastic work required for fracture; this has been associated with more homogeneous plastic deformation (204,205), or a reduction in rates of thermally-activated processes at low temperatures (203). Alternatively, the reduced low-temperature crack velocities in 2090-T8 Al-Li alloy may be attributed to the smaller CTODs per cycle, resulting from an elevation in strength, elastic modulus and strain-hardening rate, and to limited environmental effects at cryogenic temperatures. However, the explanations are not definitive because of the lack of intrinsic low-temperature crack-propagation data in inert environments.

INFLUENCE OF WROUGHT-PRODUCT FORM

The predominant role of crack-tip shielding in promoting superior fatigue-crack growth resistance in Al-Li alloys via crack-deflection mechanisms implies that the effect may not necessarily be seen in all product forms (67,207). For example, at the same ΔK, fatigue cracks in 1.6-mm thick 2090-T83 sheet propagate significantly faster than in 12.7-mm thick 2090-T81 plate, particularly as ΔK levels (at $R = 0.1$) approach the fatigue threshold (Fig. 37a), although both rolled sheet and plate have nominally similar composition and hardening precipitates (207). Such faster crack-growth rates in the sheet are concurrent with markedly lower crack-closure levels compared to plate (Fig. 37b). This is in contrast to traditional aluminum alloys, such as 7075-T6, which rarely show such differences in behavior between sheet and plate, at least for ΔK levels below ~ 20 MPa$\sqrt{m}$.*

* Stress-state effects may be expected to affect crack-growth rates at higher ΔK levels as deformation conditions in the sheet alloys approach that of plane stress (207).

Such differences in fatigue behavior in Al-Li alloy sheet and plate are principally associated with microstructurally-induced variations in crack-path deflection and resulting crack-closure effects (Figs. 16-18,37,38). In the T81 plate material, marked slip-planarity induced by coherent δ' and deformation texture promotes crack deflection through crystallographically-faceted slip-band cracking(Figs. 16-18). Such effects are not as prominent in sheet (207) because recrystallization occurs readily in thin-section

products, below ~4 mm in thickness, despite the presence of Zr. The finer, partially-recrystallized grain structure and reduced texture induce essentially linear crack paths and hence far smoother fracture surfaces (Fig. 38). It should be noted, however, that even without significant crack-closure effects, Al-Li sheet alloys still display superior fatigue-crack growth resistance to traditional alloys, particularly at higher growth rates (Fig. 37a), presumably due to an increased modulus and the beneficial role of δ' in promoting planar-slip deformation and crack deflection.

The influence of load ratio and specimen orientation on the crack-growth behavior of Al-Li sheet is similar to that described above for plate alloys. Higher load ratios induce faster growth rates, particularly at near-threshold levels, and the lowest crack-growth resistance is found for the L+45° orientation (67,207). However, owing to the limited role of crack closure in sheet, the magnitude of the load-ratio and orientation effects is less pronounced than in plate alloys (207). In fact, the larger CTOD levels associated with higher load ratios minimize the closure effect to such an extent that, at $R > 0.75$, sheet and plate material show essentially similar behavior.

Differences in the S/N fatigue behavior of commercial Al-Li alloys have also been noted with differing wrought-product form (Fig. 39). Specifically, for the three principal product variants of 2090-T8X alloy, T86 extrusions exhibit the highest smooth-specimen fatigue strength, followed by T81 plate and T83 sheet; behavior, as in plate alloys, is anisotropic (67). For notched tests (with a stress concentration factor, k_t, of 3), extrusions and plate show equivalent behavior, with the fatigue strength of the sheet material being slightly inferior. Such results have been attributed to delamination-induced reduction in lateral constraint in the thicker product forms (67), although they are more likely to be associated with the lower strength of the 2090 sheet.

CONCLUDING REMARKS

The resurgence of interest in Al-Li alloys has resulted in the development of a series of low-density, monolithic aerospace materials with strength-toughness properties comparable to traditional aluminum alloys and a considerable price advantage over competing composites. Moreover, they offer the designer a material with improved fatigue-crack growth properties over many composites (Fig. 40) and traditional Al alloys, provided in-plane (e.g., L-T, T-L) orientations are used. For other orientations such as S-T and S-L, delamination cracking can lead to poor toughness and crack-growth properties in thick-plate sections. Furthermore, short-transverse delamination failures are responsible for the low fatigue lives measured under anticlastic bending fatigue (208). Under these circumstances, the performance of Al-Li alloys is inferior to traditional alloys.

Since the beneficial fatigue properties can be traced primarily to extrinsic crack-tip shielding mechanisms, designers must appreciate the implications of this phenomenon on life prediction. For example, many of the contrasting observations on the fatigue-crack growth behavior of Al-Li alloys can

be rationalized as consequences of crack-tip shielding, resulting from highly tortuous crack paths induced by planar-slip. This leads to superior long-crack properties, under constant-amplitude loading at positive, low load ratios and under tension-dominated spectrum loading, all instances where crack closure due to wedging phenomena is not restricted. However, factors which limit crack-path tortuosity and asperity wedging can compromise the superiority of these alloys. This can occur at high load ratios, under compression-dominated spectrum loading, with microstructurally-small cracks, and with refined and overaged microstructures; in these instances, the fatigue behavior of Al-Li alloys is essentially similar to 2000 and 7000 series alloys.

A further consequence of the role of crack-tip shielding in Al-Li alloys is complications with the assessment of fatigue-crack growth resistance. In addition to loading spectra, crack size and specimen orientation, crack-growth behavior tends to be strongly dependent on wrought-product form and specimen geometry. For example, thin specimens generally will exhibit significantly faster crack-growth rates than thick specimens of nominally identical composition and microstructure, principally by reducing through-thickness crack-path meandering. Similarly, center-cracked, rather than compact tension, bend or double-cantilever beam, specimen geometries may also limit the fatigue-crack growth property advantage of Al-Li alloys by reducing off-angle cracking and inhibiting crack deflection. A similar suppression of shielding in Al-Li alloys has been reported by testing single-edged-notched tension specimens with fixed grips compared to freely-rotating grips (131).

Finally, it should be noted that primary sources for crack deflection and crack-path tortuosity, which confer the excellent fatigue-crack growth properties in commercial Al-Li plate alloys, are marked slip planarity, strong deformation texture and weak short-transverse properties, all microstructural features which limit toughness and which may be considered undesirable for many service applications. Although new alloys can, and have been, developed with less anisotropy to solve this problem, their fatigue-crack growth properties are likely to be inferior to those of the early commercial alloys.

These factors suggest that the use of Al-Li alloys, or the direct substitution for traditional alloys, in fatigue critical designs requires a greater mechanistic understanding and more detailed analysis of the correlation of laboratory-scale coupon tests to the performance of structures in service; with Al-Li alloys, it is by no means certain that the superior fatigue properties measured in laboratory tests will always be realized in actual structures.

ACKNOWLEDGEMENTS

This work was supported by the Director, Office of Energy Research, Office of Basic Energy Sciences, Materials Sciences Division of the U.S. Department of Energy under Contract No. DE-AC03-76SF00098. The authors would particularly like to thank Dr. R. J. Bucci of Alcoa for his help and encouragement throughout this work. In addition, they thank Drs. P. E. Bretz and R. R. Sawtell, also from Alcoa, P. O. Wakeling formerly of Alcan, Drs. G. R. Chanani, G. V. Scarich and K. M. Bresnahan of Northrop, Dr. W. E. Quist of Boeing, Mr. G. J. Petrak of WRDC, Dr. S. Das of Allied-Signal Inc., Prof. R. P. Gangloff of the University of Virginia, Prof. N. J. Kim of Pohang Institute of Technology (Korea), Dr. K. V. Jata of the University of Dayton Research Institute, Dr. R. S. Piascik of NASA Langley, and Prof. P. P. Pizzo of San José State University for their collaboration. The assistance of the late Dr. W. Yu, H. F. Hayashigatani, J. E. Miles, D. Kovar and J. C. McNulty with the experiments, Ms. Madeleine Penton with preparation of the manuscript, and the key reader and referees for their critical comments, is also gratefully acknowledged.

REFERENCES

1. F. H. Froes: *Mater. Design*, 1989, **10**:3, 111.
2. M. A. Steinberg: *Sci. Amer.*, 1986, **255**:4, 66.
3. D. R. Tenney, B. Lisagor and S. D. Dixon: *J. Aircraft*, 1989, **26**, 953.
4. P. Cannon: *J. Metals*, 1988, **40**:5, 10.
5. J. J. De Luccia, R. E. Trabocco, J. Waldman and J. F. Collins: *Adv. Mater. Proc.*, 1989, **137**:5, 39.
6. T. M. F. Ronald: *ibid.*, 1989, **137**:5, 29.
7. W. E. Quist, A. L. Wingert and G. H. Narayanan: in 'Aluminum-Lithium: Development, Application and Superplastic Forming', (ed. S. P. Agrawal and R. J. Kar), 227-279; 1986, Metals Park, Ohio, ASM International.
8. T. W. Chou, R. L. McCullough and R. B. Pipes: *Sci. Amer.*, 1986, **255**:4, 192.
9. S. V. Nair, J. K. Tien and R. C. Bates: *Int. Met. Rev.*, 1985, **30**, 275.
10. A. L. Geiger and M. Jackson: *Adv. Mater. and Proc.*, 1989, **137**:7, 23.
11. J.-K. Shang, W. Yu and R. O. Ritchie: *Mater. Sci. Eng.*, 1988, **102A**, 181.
12. S. V. Kamat, J. P. Hirth and R. Mehrabian: *Acta Metall.*, 1989, **37**, 2395.
13. R. J. Bucci, L. N. Mueller, L. B. Vogelsang and J. W. Gunnink: 'Aluminum Alloys: Contemporary Research and Applications', (ed. A. K. Vasudévan and R. D. Doherty), Treatise on Materials Science and Technology, Vol. 31, 295-322; 1990, New York, Academic Press Inc.
14. R. O. Ritchie, W. Yu and R. J. Bucci: *Eng. Fract. Mech.*, 1989, **32**, 361.
15. R. Marissen: Ph.D. Thesis, Delft. Univ. of Tech. (1988).
16. * T. H. Sanders and E. A. Starke (eds.): 'Aluminum-Lithium Alloys', Proc. of the I Intl. Conf. on Aluminum-Lithium Alloys, 1981, Warrendale, Pennsylvania, The Metallurgical Society of AIME.
17. * T. H. Sanders and E. A. Starke (eds.): 'Aluminum-Lithium Alloys II', Proc. of the II Intl. Conf. on Aluminum-Lithium Alloys, 1984, Warrendale, Pennsylvania, The Metallurgical Society of AIME.
18. * C. Baker, P. J. Gregson, S. J. Harris and C. J. Peel (eds.): 'Aluminum-Lithium Alloys III', Proc. of the III Intl. Conf. on Aluminum-Lithium Alloys, 1986, London, Institute of Metals.
19. * C. Champier, B. Dubost, D. Miannay and L. Sabetay (eds.): '4th International Aluminum-Lithium Conference', J. de Phys. Coll., Vol. C3:9; 1987, Paris, Les Editions de Physique.
20. * T. H. Sanders and E. A. Starke (eds.): 'Aluminum-Lithium Alloys V', Proc. of the V Intl. Conf. on Aluminum-Lithium Alloys, 1989, Edgbaston, U.K., Materials and Component Engineering Publications Ltd.
21. E. A. Starke, T. H. Sanders and I. G. Palmer: *J. Metals*, 1981, **33**:8, 24.

22. R. Grimes, A. J. Cornish, W. S. Miller and M. A. Reynolds: *Metals Mater.*, 1988, **4**:7, 357.
23. C. A. Stubbington: *ibid.*, 1988, **4**:7, 424.
24. T. H. Sanders and E. S. Balmuth: *Metals Prog.*, 1978, **121**, 32.
25. R. C. Dorward and T. R. Pritchett: *Mater. Design.*, 1988, **9**:2, 63.
26. R. S. James: in 'Metals Handbook,' Vol. 2, 178-199; 1990, Tenth Edition, Metals Park, OH, ASM International.
27. W. E. Quist and G. H. Narayanan: in 'Aluminum Alloys: Contemporary Research and Applications', (ed. A. K. Vasudévan and R. D. Doherty), Treatise on Materials Science and Technology, Vol. 31, 219-254; 1990, New York, Academic Press Inc.
28. C. J. Peel: *Mater. Sci. Tech.*, 1987, **4**, 1169.
29. E. S. Balmuth and R. Schmidt: in Ref. 16, 69.
30. W. E. Quist, G. H. Narayanan and A. L. Wingert: in Ref. 16, 313.
31. J. C. Ekvall, J. E. Rhodes and G. G. Wald: in 'Design of Fatigue and Fracture Resistant Structures', ASTM STP 761, 328-341; 1982, Philadelphia, American Society for Testing and Materials.
32. R. E. Lewis, D. Webster and I. G. Palmer: 'A Feasibility Study for Development of Structural Aluminum Alloys from Rapidly Solidified Powders for Aerospace Structural Applications', Final Report No. AFML- TR-78-102, Lockheed Palo Alto Research Laboratory, Palo Alto, 1978.
33. B. Noble, S. J. Harris and K. Dinsdale: *J. Mater. Sci.*, 1982, **17**, 461.
*34. T. H. Sanders and E. A. Starke: *Acta Metall.*, 1982, **30**, 927.
*35. K. V. Jata and E. A. Starke: *Metall. Trans. A*, 1986, **17A**, 1011.
36. W. S. Miller, M. P. Thomas, D. J. Lloyd and D. Creber: *Mater. Sci. Tech.*, 1986, **2**, 1210.
37. D. Dew-Hughes, E. Creed and W. S. Miller: *ibid.*, 1988, **4**, 106.
38. J. Glazer, S. L. Verzasconi, E. N. C. Dalder, W. Yu, R. A. Emigh, R. O. Ritchie and J. W. Morris: *Adv. Cryogen. Eng.*, 1986, **32**, 397.
39. D. Webster: *Metal Prog.*, 1984, **125**, 31.
40. R. C. Dorward: *Scripta Metall.*, 1986, **20**, 1379.
41. K. T. Venkateswara Rao, W. Yu and R. O. Ritchie: *Metall. Trans A*, 1989, **20A**, 485.
42. K. V. Jata and E. A. Starke: *Scripta Metall.*, 1988, **22**, 1553.
43. S. Suresh, A. K. Vasudévan, M. Tosten and P. R. Howell: *Acta Metall.*, 1987, **35**, 25.
*44. A. K. Vasudévan, R. D. Doherty and S. Suresh: in 'Aluminum Alloys: Contemporary Research and Applications', (ed. A. K. Vasudévan and R. D. Doherty), Treatise on Materials Science and Technology, Vol. 31, 445- 462; 1990, New York, Academic Press Inc.
45. R. O. Ritchie: *Mater. Sci. Eng. A*, 1988, **A103**, 15.
46. A. G. Evans: in 'Fracture Mechanics: Perspectives and Directions (20th Symposium)', (ed. R. P. Wei and R. P. Gangloff), ASTM STP 1020, 267-291; 1989, Philadelphia, American Society for Testing and Materials.
47. H. M. Flower and P. J. Gregson: *Mater. Sci. Tech.*, 1987, **3**, 81.
48. S. F. Baumann and D. B. Williams: *Metall. Trans. A*, 1985, **16A**, 1203.
49. T. H. Sanders and E. A. Starke: in Ref. 20, 1.
50. D. B. Williams: in Ref. 20, 551.
51. M. H. Tosten, A. K. Vasudévan and P. R. Howell: *Metall. Trans. A*, 1988, **19A**, 51.
52. R. J. Rioja, P. E. Bretz, R. R. Sawtell, W. H. Hunt and E. A. Ludwiczak: in 'Aluminum Alloys: Their Physical and Mechanical Properties', (ed. T. H. Sanders and E. A. Starke), 1781-1797; 1986, Warley, U.K., Engineering Materials Advisory Services Ltd.
53. J. C. Huang and A. J. Ardell: in Ref. 18, 455.
54. D. B. Williams and P. R. Howell: in 'Aluminum Alloys: Contemporary Research and Applications', (ed. A. K. Vasudévan and R. D. Doherty), Treatise on Materials Science and Technology, Vol. 31, 365-388; 1990, New York, Academic Press Inc.
55. J. M. Papazian and P. S. Gilman: *Mater. Sci. Eng. A*, 1990, **A125**, 121.
56. F. W. Gayle and B. Vandersande: *Acta Metall.*, 1989, **37**, 1033.
*57. J. Dhers, J. Driver and A. Fourdeux: in Ref. 18, 233.
58. K. T. Venkateswara Rao and R. O. Ritchie: *Mater. Sci. Tech.*, 1989, **5**, 882.

59. A. K. Vasudévan, W. G. Fricke, R. C. Malcolm, R. J. Bucci, M. A. Przystupa and F. Barlat: *Metall. Trans. A*, 1988, **19A**, 731.
60. J. Hirsch, O. Engler, K. Lucke, M. Peters, K. Welpmann: in Ref. 19, 605.
61. G. R. Yoder, P. S. Pao, M. A. Imam and L. A. Cooley: *Scripta Metall.*, 1988, **22**, 1241.
62. G. R. Yoder, P. S. Pao, M. A. Imam and L. A. Cooley: *Scripta Metall.*, 1989, **23**, 1455.
63. C. J. Warren and R. J. Rioja: in Ref. 20, 417.
64. M. Peters, J. Eschweiler and K. Welpmann: *Scripta Metall.*, 1986, **20**, 259.
65. A. K. Vasudévan, M. A. Pryzstupa and W. G. Fricke: *Scripta Metall.*, 1990, **24**, 1429.
66. S. J. Harris, B. Noble and A. Dodd: in Ref. 20, 1061.
*67. R. J. Bucci, R. C. Malcolm, E. L. Colvin, S. Murtha and R. S. James: 'Cooperative Test Program for the Evaluation of Engineering Properties of Al-Li Alloy 2090-T8X Sheet, Plate and Extrusion Products', Report NSWC TR 89-106, Aluminum Technical Center, Pittsburgh, 1989.
68. P. Meyer, Y. Cans, D. Ferton and M. Reboul: in Ref. 19, 131.
69. M. A. Reynolds and E. Creed: in Ref. 19, 195.
70. W. S. Miller, J. White, M. A. Reynolds, D. S. McDarmaid and G. M. Starr: in Ref. 17, 151.
71. A. F. Smith: in Ref. 20, 1587.
72. N. J. Kim, D. Raybould, R. L. Bye and S. K. Das: in Ref. 20, 123.
73. M. R. Mitchell: in 'Fatigue and Microstructure', 385-437; 1979, Metals Park, Ohio, American Society for Metals.
*74. E. J. Coyne, T. H. Sanders and E. A. Starke: in Ref. 16, 293.
*75. T. S. Srivatsan, K. Yamaguchi and E. A. Starke: *Mater. Sci. Eng.*, 1986, **83**, 87.
76. Y. Brechet, F. Louchet and J. L. Verger-Gaugry: in Ref. 19, 709.
*77. Y. Brechet, F. Louchet and T. Magnin: *J. Mater. Sci.*, 1990, **25**, 3053.
78. S. Han, A. Tourabi and B. Wack: in Ref. 19, 701.
79. J. Schneider, H.-J. Gudladt and V. Gerold: in Ref. 19, 745.
80. Y. Xiao and P. Bompard: in Ref. 17, 737.
81. T. S. Srivatsan and E. J. Coyne: *Mater. Sci. Tech.*, 1989, **5**, 548.
82. T. S. Srivatsan and E. J. Coyne: *Int. J. Fatigue*, 1988, **10**, 91.
83. D. Khireddine, R. Rahouadj and M. Clavel: *Scripta Metall.*, 1988, **22**, 167.
*84. D. Khireddine, R. Rahouadj and M. Clavel: *Acta Metall.*, 1989, **37**, 191.
*85. N. Eswara Prasad, G. Malakondaiah, K. N. Raju and P. Rama Rao: in 'Advances in Fracture Research', Proc. of the VII Intl. Conf. of Fracture, (ed. K. Salama et al.), 1103-1112; 1989, London, Pergamon Press.
*86. W. X. Feng, F. S. Lin and E. A. Starke: *Metall Trans. A*, 1984, **15A**, 1209.
*87. R. T. Chen and E. A. Starke: *Mater. Sci. Eng.*, 1984, **67**, 229.
88. B. Velten, A. K. Vasudévan and E. Hornbogen: *Z. Metallkde.*, 1989, **80**, 21.
*89. J. M. Gentzbittel and F. Fougeres: *Scripta Metall.*, 1987, **21**, 1411.
*90. Y. Brechet, F. Louchet, C. Marchionni and J. L. Verger-Gaugry: *Phil. Mag.*, 1987, **56**, 353.
91. J. Lendvai, H.-J. Gudladt and V. Gerold: *Scripta Metall.*, 1988, **22**, 1755.
*92. Z. Di, S. Saji, S. Hori: in Ref. 19, 753.
93. R. E. Lee and W. J. D. Jones: *J. Mater. Sci.*, 1974, **9**, 476.
94. S. H. Chen: 'Fatigue Properties of Al-Li alloy', M.S. Thesis, 1985, China, National Tsing Hua University.
*95. P. J. E. Bischler and J. W. Martin: in Ref. 19, 761.
96. L. Farcy, C. Carre, M. Clavel, Y. Barbaux and D. Aliaga: in Ref. 19, 769.
*97. M. Peters, K. Welpmann, W. Zink and T. H. Sanders: in Ref. 18, 239.
*98. P. E. Bretz, L. N. Mueller and A. K. Vasudévan: in Ref. 17, 543.
99. P. J. Gregson, J. Newman and A. Gray: *Mater. Sci. Tech.*, 1989, **5**, 65.
100. Y. Mutoh, G. H. Fair, B. Noble and R. B. Waterhouse: *Fat. Fract. Engng. Mater. Struct.*, 1987, **10**, 261.
101. V. J. Bolam, P. J. Gregson and A. Gray: in Ref. 20, 1097.
102. R. W. Hertzberg: 'Deformation and Fracture Mechanics of Engineering Materials', 1989, Third Edition, New York, John Wiley & Sons.
103. R. O. Ritchie: *Int. Met. Rev.*, 1979, **20**, 205.

104. S. Suresh: 'Fatigue of Materials', 1991, New York, Cambridge University Press.
105. W. Elber: in 'Damage Tolerance in Aircraft Structures', ASTM STP 486, 230-242; 1971, Philadelphia, American Society for Testing and Materials.
106. N. Walker and C. J. Beevers: *Fat. Eng. Mater. Struct.*, 1979, **1**, 135.
107. K. Minakawa and A. J. McEvily: *Scripta Metall.*, 1981, **15**, 633.
108. S. Suresh, G. F. Zamiski and R. O. Ritchie: *Metall. Trans. A*, 1981, **12A**, 1435.
109. R. O. Ritchie and S. Suresh: *Metall. Trans A.*, 1982, **13A**, 937.
110. J. C. Newman and W. Elber (eds.): 'Mechanics of Fatigue Crack Closure', ASTM STP 982, 1988, Philadelphia, American Society for Testing and Materials.
111. J. E. Allison: in 'Fracture Mechanics: Eighteenth Symposium', ASTM STP 945, 913-933; 1988, Philadelphia, American Society for Testing and Materials.
112. W. A. Herman, R. W. Hertzberg and R. Jaccard: *Fat. Eng. Mater. Struct.*, 1988, **10**, 303.
113. S. J. Harris, B. Noble and K. Dinsdale: in Ref. 17, 219.
114. P. S. Pao, K. K. Sankaran and J. E. Neal: in Ref. 16, 307.
115. A. K. Vasudévan, P. E. Bretz, A. C. Miller and S. Suresh: *Mater. Sci. Eng.*, 1984, **64**, 113.
116. S. Suresh, A. K. Vasudévan and P. E. Bretz: *Metall. Trans A*, 1984, **15A**, 369.
117. E. Zaiken and R. O. Ritchie: *Mater. Sci. Eng.*, 1985, **70**, 151.
118. R. D. Carter, E. W. Lee, E. A. Starke and C. J. Beevers: *Metall. Trans. A*, 1984, **15A**, 555.
119. J. Petit, S. Suresh, A. K. Vasudévan and R. C. Malcolm: in Ref. 18, 257.
120. A. K. Vasudévan and S. Suresh: *Metall. Trans. A*, 1985, **16A**, 475.
121. C. Q. Chen and H. X. Li: in Ref. 20, 973.
122. R. Tintillier, H. J. Gudladt, V. Gerold and J. Petit: in Ref. 20, 1135.
123. K. T. Venkateswara Rao, W. Yu and R. O. Ritchie: *Metall. Trans. A*, 1988, **19A**, 549.
124. K. T. Venkateswara Rao and R. O. Ritchie: *Mater. Sci. Tech.*, 1989, **5**, 896.
125. C. P. Blankenship and E. A. Starke, Jr.: *Fat. Fract. Engng. Mater. Struct.*, 1991, **14**, 103.
126. R. Tintillier, H. S. Yang, N. Ranganathan and J. Petit: in Ref. 19, 777.
127. M. Peters, V. Bachmann, K. Welpmann: in Ref. 19, 785.
128. D. S. McDarmaid and C. J. Peel: in Ref. 20, 993.
129. H. D. Peacock and J. W. Martin: in Ref. 20, 1013.
130. J. M. Newman, P. J. Gregson, P. D. Pitcher and P. J. E. Forsyth: in Ref. 20, 1043.
131. R. S. Piascik and R. P. Gangloff: *Metall. Trans A*, 1991, **22A**, 2415.
132. R. S. Piascik and R. P. Gangloff: *Metall. Trans. A*, 1991, **22A**, in review.
133. R. S. Piascik: Ph.D. Thesis, 1989, Charlottesville, University of Virginia.
134. R. P. Gangloff, R. S. Piascik, D. L. Dicus and J. C. Newman: in 'Proceedings 17th ICAS Congress', in press; 1990, London, Royal Aeronautical Society.
135. K. T. Venkateswara Rao, R. S. Piascik, R. P. Gangloff and R. O. Ritchie: in Ref. 20, 955.
136. W. Yu and R. O. Ritchie: *J. Eng. Mater. Tech.*, 1987, **109**, 81.
137. S. Suresh: *Metall. Trans. A*, 1983, **14A**, 2375.
138. F. L. Haddleton, S. Murphy and T. J. Griffin: in Ref. 19, 809.
139. R. O. Ritchie and J. Lankford (eds.): 'Small Fatigue Cracks', 1986, Warrendale, Pennsylvania, The Metallurgical Society of AIME.
140. K. J. Miller and E. R. de los Rios (eds.): 'The Behavior of Short Fatigue Cracks', 1986, London, Institution of Mechanical Engineers.
141. S. Suresh and R. O. Ritchie: *Int. Met. Rev.*, 1984, **29**, 445.
142. K. T. Venkateswara Rao, W. Yu and R. O. Ritchie: *Metall. Trans A*, 1988, **19A**, 563.
143. M. R. James: *Scripta Metall.*, 1987, **21**, 783.
144. Z. Chen, A. Zeghloul and J. Petit: *Scripta Metall.*, 1989, **23**, 1005.
145. X. Su, J. M. Larsen and J. R. Jira: in 'Fatigue '90', Proc. of IV Intl. Conf on Fatigue and Fatigue Thresholds, (ed. H. Kitagawa and T. Tanaka) 1049-1054; 1990, Edgbaston, Materials and Component Engineering Publications Ltd.
146. J. M. Newman, P. J. Gregson, P. J. E. Forsyth and P. D. Pitcher: *Scripta Metall.*, 1989, **23**, 1157.
147. D. J. Nicholls and J. W. Martin: *Fat. Fract. Eng. Mater. Struct.*, 1990, **13**, 83.
148. D. J. Nicholls and J. W. Martin: *Mater. Sci. Eng. A*, 1990, **A128**, 141.

*149. K. T. Venkateswara Rao, W. Yu and R. O. Ritchie: *Eng. Fract. Mech.*, 1988, **31**, 623.
*150. R. W. Hertzberg, W. A. Herman and R. O. Ritchie: *Scripta Metall.*, 1987, **21**, 1541.
*151. K. T. Venkateswara Rao and R. O. Ritchie: *Acta Metall.*, 1988, **26**, 2949.
152. R. P. Wei and R. I. Stephens (eds.): 'Fatigue Crack Growth Under Spectrum Loads', ASTM STP 595; 1976, Philadelphia, American Society for Testing and Materials.
153. C. M. Ward-Close, A. F. Blom and R. O. Ritchie: *Eng. Fract. Mech.*, 1989, **32**, 613.
154. D. J. Alexander and J. F. Knott: in 'Fatigue '87', Proc. of III Intl. Conf. on Fatigue and Fatigue Thresholds, (ed. R. O. Ritchie and E. A. Starke), 395-406; 1987, Warley, U.K., Engineering Materials Advisory Services Ltd.
155. C. Espinasse and C. Bathias: in Ref. 19, 793.
*156. N. Ohrloff, A. Gysler and G. Lütjering: in Ref. 19, 801.
157. M. T. Yu and T. H. Topper: *J. Eng. Mater. Tech.*, 1985, **107**, 19.
158. E. Zaiken and R. O. Ritchie: *Eng. Fract. Mech.*, 1985, **22**, 35.
159. G. V. Scarich and P. E. Bretz: 'Fatigue Crack-Growth Resistance of Aluminum Alloys Under Spectrum Loading: Volume I-Commercial 2XXX and 7XXX Alloys', Technical Report No. NOR 85-141, Northrop Corporation, Hawthorne, CA, 1985.
*160. G. V. Scarich, K. M. Bresnahan and P. E. Bretz: 'Fatigue Crack-Growth Resistance of Aluminum Alloys Under Spectrum Loading: Volume II- Aluminum-Lithium Alloys', Technical Report No. NOR 85-141, Northrop Corporation, Hawthorne, CA 1985.
161. W. E. Quist, G. H. Narayanan, A. L. Wingert and T. M. F. Ronald: in Ref. 18, 625.
162. N. J. Kim, R. L. Bye and S. K. Das: in Ref. 19, 309.
163. W. Wang and N. J. Grant: in Ref. 17, 447.
164. R. D. Schelleng: *J. Metals*, 1983, **41**:1, 32.
165. P. S. Gilman: in Ref. 17, 485.
166. F. W. Gayle, N. F. Levoy and J. B. Vandersande: *J. Metals*, **39**:5, 33.
167. H. Kemper, B. Weiss and R. Stickler: in *Proc. of VIII Intl. Conf. on Light Metals*, 1987.
168. W. Ruch and E. A. Starke: in Ref. 18, 121.
*169. H. Kemper, B. Weiss and R. Stickler: in 'Fatigue '87', Proc. of III Intl. Conf. on Fatigue and Fatigue Thresholds, (ed. R. O. Ritchie and E. A. Starke), 789-800; 1987, Warley, U.K., Engineering Materials Advisory Services Ltd.
*170. K. T. Venkateswara Rao and R. O. Ritchie: *Metall. Trans A*, 1991, **22A**, 191.
171. K. V. Jata, W. Ruch and E. A. Starke: in 'Light Metals', 55-62; 1985, Europe, Materials Research Society.
172. H. Kemper, B. Weiss and R. Stickler: *Eng. Fract. Mech.*, 1989, **32**, 591.
173. M. D. Wright and C. J. Beevers: in Ref. 20, 1087.
*174. K. T. Venkateswara Rao and R. O. Ritchie: *Mater. Sci. Eng.*, 1988, **100**, 23.
175. K. T. Venkateswara Rao, J. C. McNulty and R. O. Ritchie: *Metall. Trans A*, 1991, **22A**, in review.
176. R. C. Malcolm, F. J. Cordier and R. J. Bucci: 'The Effects of Various Thermal Conditions on the Tensile Properties of Aluminum Alloy 2090-T8E41 Plate', Report No. 56-86-AH429, Alcoa Technical Center, Pittsburgh, 1986.
177. R. M. Pelloux, R. E. Stoltz and J. A. Moskowitz: *Mater. Sci. Eng.*, 1976, **25**, 193.
178. R. P. Gangloff: in 'Environment Induced Cracking of Metals, (ed. R. P. Gangloff and M. B. Ives), in press; 1990, Houston, National Association of Corrosion Engineers.
179. M. Gao, P. S. Pao and R. P. Wei: *Metall. Trans A*, 1988, **19A**, 1739.
180. R. P. Gangloff and D. J. Duquette: in 'Chemistry and Physics of Fracture' (ed. R. M. Latanision and R. H. Jones), 612-645; 1987, Netherlands, Martinus Nijhoff Publishers.
181. R. E. Stoltz and R. M. Pelloux: *Metall. Trans.*, 1972, **3**, 2433.
182. C. P. Dervenis, E. I. Meletis and R. F. Hochman: *Mater. Sci. Eng. A*, 1988, **A102**, 151.
183. M. Rebiere and T. Magnin: *Mater. Sci. Eng. A*, 1990, **A128**, 99.
184. R. E. Ricker: Ph.D. Thesis, 1982, Troy, New York, Rensselaer Polytechnic Institute.
*185. P. S. Pao, M. A. Imam, L. A. Cooley and G. R. Yoder: *Corrosion*, 1989, **45**, 530.
*186. R. S. Piascik and R. P. Gangloff: in 'Environment Induced Cracking of Metals', (ed. R. P. Gangloff and M. B. Ives), in press; 1990, Houston, National Association of Corrosion Engineers.

187. M. O. Spiedel: *Metall. Trans. A*, 1975, **6A**, 631.
188. A. Gray, N. J. H. Holroyd and J. White: in Ref. 20, 1175.
189. J. G. Rinker, M. Marek and T. H. Sanders: *Mater. Sci. Eng.*, 1984, **64**, 203.
190. R. C. Dorward and K. R. Hasse: *Corrosion*, 1988, **44**, 932.
191. N. J. H. Holroyd, A. Gray, G. M. Scamans and R. Hermann: in Ref. 16, 310.
192. K. T. Venkateswara Rao, D. Kovar and R. O. Ritchie: unpublished results, 1990.
193. N. J. H. Holroyd and D. Hardie: *Corr. Sci.*, 1983, **23**, 527.
194. A. M. Green and J. F. Knott: in 'Advances in Fracture Research', Proc. of the VII Intl. Conf. of Fracture (ed. K. Salama *et al.*), 1747-1756; 1989, London, Pergamon Press.
195. F. J. Bradshaw and C. Wheeler: *Int. J. Fract. Mech.*, 1969, **5**, 255.
196. R. J. Selines and R. M. Pelloux: *Metall. Trans.*, 1972, **3**, 2525.
197. R. P. Wei and R. P. Gangloff: in 'Fracture Mechanics: Perspectives and Directions', ASTM STP 1020, (ed. R. P. Wei and R. P. Gangloff), 233- 264; 1989, Philadelphia, American Society for Testing and Materials.
198. R. P. Gangloff and R. O. Ritchie: in 'Fundamentals of Deformation and Fracture', (ed. B. A. Bilby, K. J. Willis and K. J. Miller), 529- 558;1985, Cambridge, U.K., Cambridge University Press.
199. K. T. Venkateswara Rao and R. O. Ritchie: *Scripta Metall.*, 1989, **23**, 1129.
200. K. T. Venkateswara Rao and R. O. Ritchie: *Acta Metall. Mater.*, 1990, **38**, 2309.
201. L. M. Ma, J. K. Han, R. L. Tobler, R. P. Walsh and R. P. Reed: *Adv. Cryog. Eng.*, 1990, **34**, 1143.
202. R. L. Tobler, J. K. Han, L. Ma, R. P. Walsh and R. P. Reed: in Ref. 20, 1115.
203. Y. B. Xu, Z. G. Wang, Y. Zhang, H. H. Zhao and Z. Q. Hu: in Ref. 20, 1147.
204. P. K. Liaw and M. E. Fine: *Metall. Trans. A*, 1981, **12A**, 1927.
205. J. McKittrick, P. K. Liaw, S. I. Kwun and M. E. Fine: *Metall. Trans. A*, 1981, **12A**, 1535.
206. P. K. Liaw and W. A. Logdson: *Acta Metall.*, 1988, **36**, 1731.
*207. K. T. Venkateswara Rao, R. J. Bucci, K. V. Jata and R. O. Ritchie: *Mater. Sci. Eng. A*, 1991, **A141**, 39.
208. R. Crooks and M. R. Mitchell: in Ref. 20, 1023.

*Key references on fatigue of Al-Li alloys.

TABLE I

Chemical composition limits for the major alloying elements in advanced aluminum-lithium alloys and traditional aluminum alloys (wt. %)

Alloy	Li	Cu	Mg	Zn	Zr	Mn	O*	Other	Al
I/M 2090	1.9-2.6	2.4-3.0	0.0-0.25	--	0.08-0.15	--	--	--	bal
I/M 2091	1.7-2.3	1.8-2.5	1.1-1.9	0.25	0.04-0.16	--	--	--	bal
I/M 8090	2.2-2.7	1.0-1.6	0.6-1.3	--	0.04-0.16	--	--	--	bal
I/M 8091	2.4-2.8	1.6-2.2	0.5-1.2	--	0.08-0.16	--	--	--	bal
I/M W049 (Weldalite)	1.3	5.0	0.4	--	0.1	--	--	--	bal
I/M 2020	1.1	--	--	--	--	0.5	--	0.2Cd	bal
MA IN-905XL	1.5	--	4.0	--	--	--	0.8	1.1C	bal
RSP 644-B	3.0-3.2	0.8-1.1	0.4-0.6	--	0.4-0.6	--	--	--	bal
I/M 2124	--	4.5	1.5	0.25	--	--	--	--	bal
I/M 7150	--	2.1	2.2	6.16	0.13	--	--	--	bal
I/M 7075	--	2.0	2.6	5.8	--	--	--	--	bal
P/M 7091	--	1.7	2.5	6.2	--	--	0.35	0.4Co	bal

*as oxide

TABLE II

Summary of Chemical Compositions, Heat Treatments, Microstructures and Mechanical Properties of Selected Binary Aluminum-Lithium Alloys†

Alloy wt. %	Heat Treatments Procedures	Microstructural Features	Tensile Properties* σ_y MPa	σ_u MPa	% Elongation
Al-0.7Li	SHT + CWQ** naturally aged	Li in solid solution with short range order	45	65	26
Al-2.5Li underaged	SHT + CWQ naturally aged	δ' (Al_3Li) 2-5 nm in diameter	67	157	33
Al-2.5Li peakaged	SHT + CWQ aged 1 h at 473 K	δ' (Al_3Li) 15-20 nm in diameter, δ (AlLi)	185	220	2.6

†Taken from reference 57.
*σ_y and σ_u are the yield and ultimate tensile strengths, respectively.
**solution heat treatment for 2 h at 806 K + cold water quench.

TABLE III

Experimental thermomechanical treatments utilized to obtain the various microstructures in commercial aluminum-lithium and aluminum alloys†

Alloy	Condition	Heat Treatment
2090 T81	(peak-aged)	solution treat, CWQ*, 6% stretch, aged 24 h at 436 K
2091 T351	(underaged)	solution treat, CWQ, 2% stretch, naturally aged
2091 T8	(peak-aged)	solution treat, CWQ, 2% stretch, aged 10 h at 408 K
8090 T351	(underaged)	solution treat, CWQ, 3% stretch, naturally aged
8090 T8	(peak-aged)	solution treat, CWQ, 3% stretch, aged 16 h at 463 K
8091 T351	(underaged)	solution treat, CWQ, 3% stretch, naturally aged
8091 T8	(peak-aged)	solution treat, CWQ, 3% stretch, aged 16 h at 463 K
W049 T3	(underaged)	solution treat, CWQ, 3% stretch, naturally aged
W049 T8	(peak-aged)	T3 condition + aged 24 h at 433 K
2020 T651	(peak-aged)	solution treat, CWQ, 1.5% stretch, aged 24 h at 422 K
IN-905XL	(peak-aged)	solution treat, CWQ, aged 24 h at 443 K
644-B	(near peak-aged)	solution treat, HWQ**, aged 16 h at 405 K
2124 T351	(underaged)	solution treat, CWQ, 2% stretch, naturally aged
7150 T651	(peak-aged)	solution treat, CWQ, 2% stretch, aged 100 h at 394 K
7075 T651	(peak-aged)	solution treat, CWQ, 2% stretch, aged 24 h at 394 K
7091 T7E69	(overaged)	solution treat, CWQ, aged 24 h at 394 K + 4 h at 436 K

†Taken from references 16-20,58,125,170.
*cold water quench at 298 K
**hot water quench at 333 K

TABLE IV

Summary of the grain-size measurements and strengthening precipitates in the various advanced and conventional aerospace aluminum alloys†

Alloy	Typical Grain Size* L mm	T μm	S μm	Principal Hardening Precipitates**
2090-T81	2-3	500	50	$\delta'(Al_3Li)$, $T_1(Al_2CuLi)$, $\theta'(Al_2Cu)$ $\beta'(Al_3Zr)$
2091-T351	1-2	600	50	δ', β'
2091-T8				δ', β'
8090-T351	1-2	350	40	δ', β'
8090-T8				δ', T_1, S (Al_2CuMg) , β'
8091-T351	0.3	65	25	δ', β'
8091-T8				δ', S, β'
W049-T3	--	--	--	GP zones, δ'
W049-T8	--	--	--	δ', T_1, θ'
2020-T651	0.8	75	35	δ', T_1, θ', T_B
IN-905XL	0.0015	0.4	0.3	Al_2O_3, Al_4C_3
644-B	0.05-0.1	1-2	1-2	δ', β', composite δ'-β'
2124-T351	0.7	350	50	GP zones
7150-T651	2-3	750	30	η' ($MgZn_2$-$Mg(CuAl)_2$)
7075-T651	0.125	16	10	GP zones, η', $Al_{12}Mg_2Cr$
7091-T7E69	2-5	1-2	1-2	GP zones, η', Co_2Al_9, Al_2CuMg, oxides

† Taken from references 16-20,58,125,170.

* L, T, and S refer to measurements in the longitudinal, long-transverse and short-transverse directions, respectively.

**Refer text for details on morphology and structure of the different phases.

TABLE V

Room-temperature mechanical properties of selected experimental and commercial aluminum-lithium and aluminum alloys*

Alloy	Young's Modulus E (GPa)	Yield Strength σ_y (MPa)	U.T.S. σ_u (MPa)	% Elongation (on 25 mm gauge)	Strain Hardening Coefficient n	Fracture Toughness K_{Ic} (MPa$\sqrt{m}$)
2090-T8	76	552	589	11	0.06	36
2091-T351	75	369	451	10	0.12	33
2091-T8	75	425	481	8	0.10	46
8090-T351	77	226	352	17	0.19	27
8090-T8	77	482	534	6	0.08	36
8091-T351	--	309	417	11	0.16	38
8091-T8	--	537	581	6	0.07	20
W049-T3	79	379	496	15	--	37
W049-T8	79	683	703	5	--	--
2020-T651	77	534	567	5	--	21
IN-905XL	--	559	596	2.3	--	13
644-B	--	422	539	8	0.19	24
2124-T351	73	360	488	18	--	24
7150-T651	73	404	480	6	--	21
7075-T651	73	503	572	11	--	28
7091-T7E69	--	545	593	11	--	46

* Uniaxial tensile properties are obtained in the longitudinal (L) direction and fracture toughness in the long-transverse (L-T) orientation. Values taken from references 16-20,58,125,170,200.

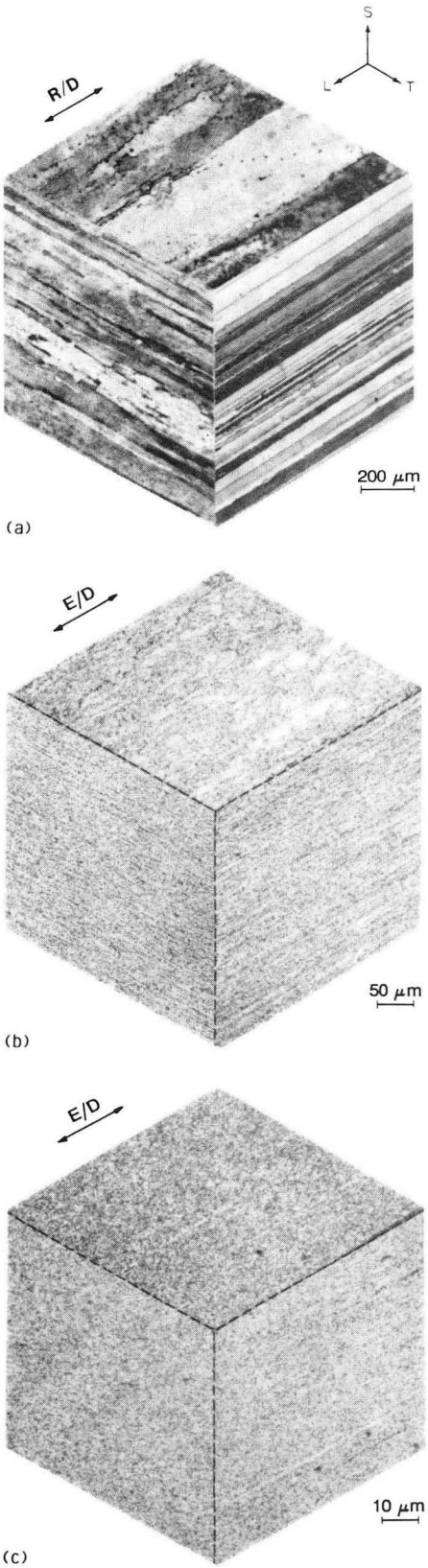

Fig. 1: Three-dimensional optical micrographs of grain structures in commercial Al-Li Alloys, processed via (a) ingot-metallurgy I/M, (b) rapid solidification (RSP) and (c) mechanical alloying (MA) techniques (170).

XBB 864-3075G

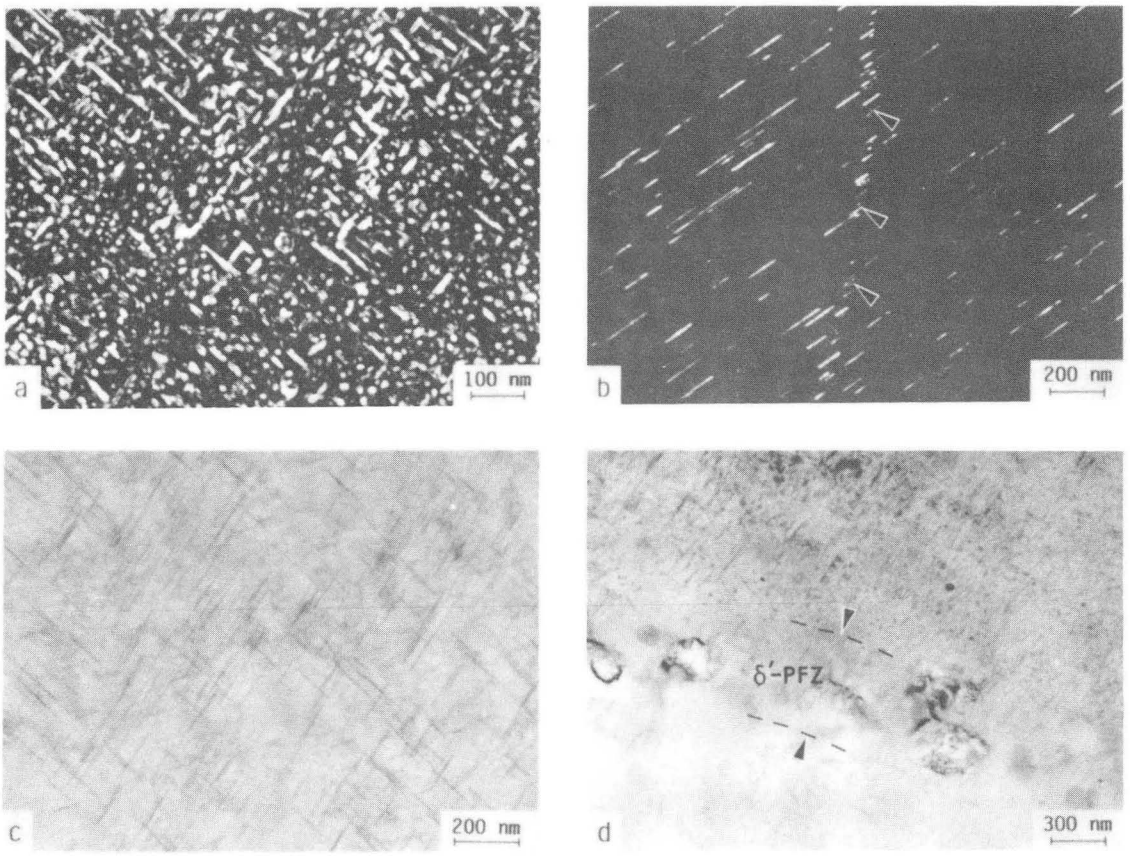

XBB 888-8249

Fig. 2: TEM micrographs showing the predominant microstructural features and strengthening precipitates in commercial Al-Li alloys, (a) δ' (Al_3Li) spheres and θ'-like (Al_2Cu) plates and (b) T_1 (Al_2CuLi) plates seen in Al-Li-Cu-Zr systems (2090-T81), (c) S (Al_2CuMg) lathes in Mg-bearing alloys (peak-aged 8090 and 8091), and (d) grain-boundary precipitation with associated δ'-PFZs (8090-T8). Spherical β' (Al_3Zr) dispersoids surrounded by δ', and δ' wetting the θ' plates may also be noted in (a); Imaging in (a), (b) was done under dark-field conditions using δ' and T_1 superlattice reflections, respectively (41).

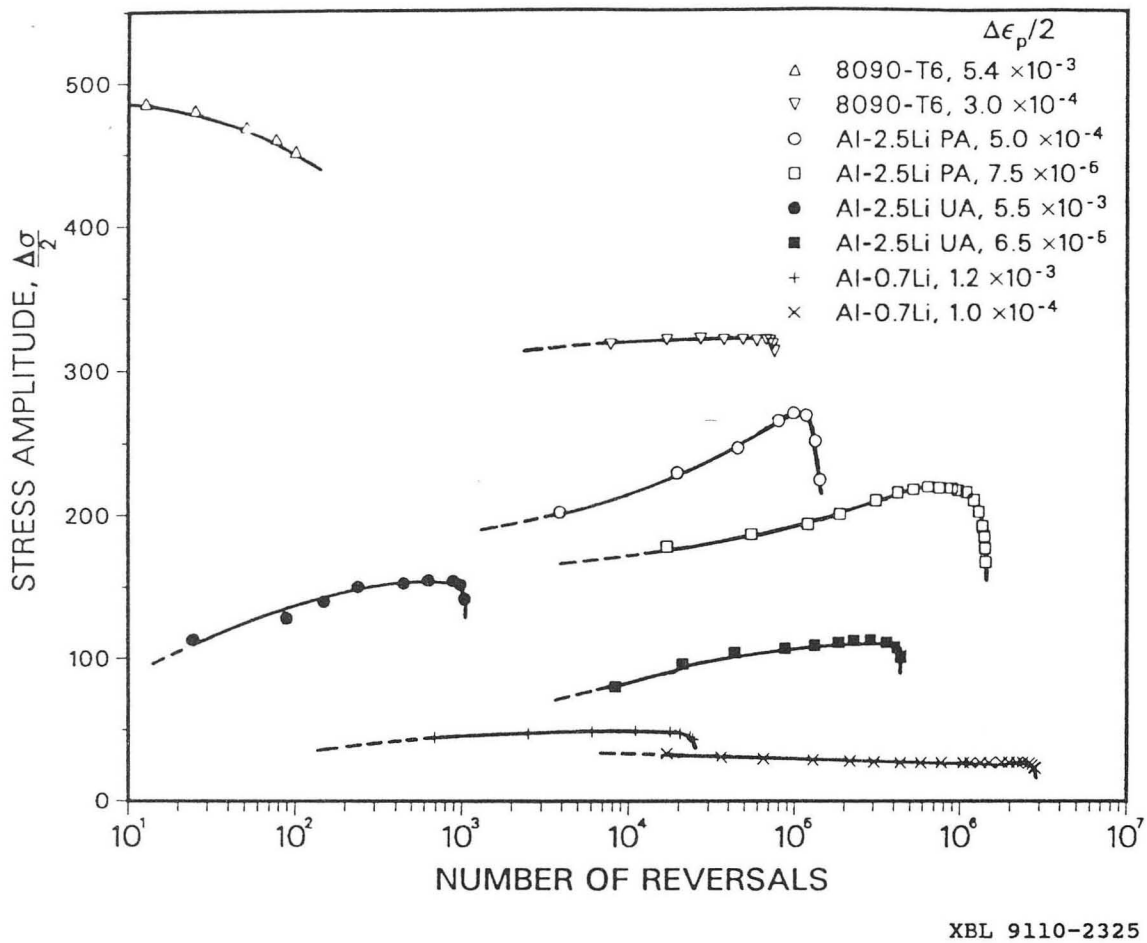

Fig. 3: Variation in cyclic stress amplitude with the number of reversals at various plastic-strain amplitudes in a Al-0.7wt.%Li solid solution, underaged and peak-aged Al-2.5wt.%Li alloy (precipitation hardened), and commercial 8090-T6 alloy (57,85).

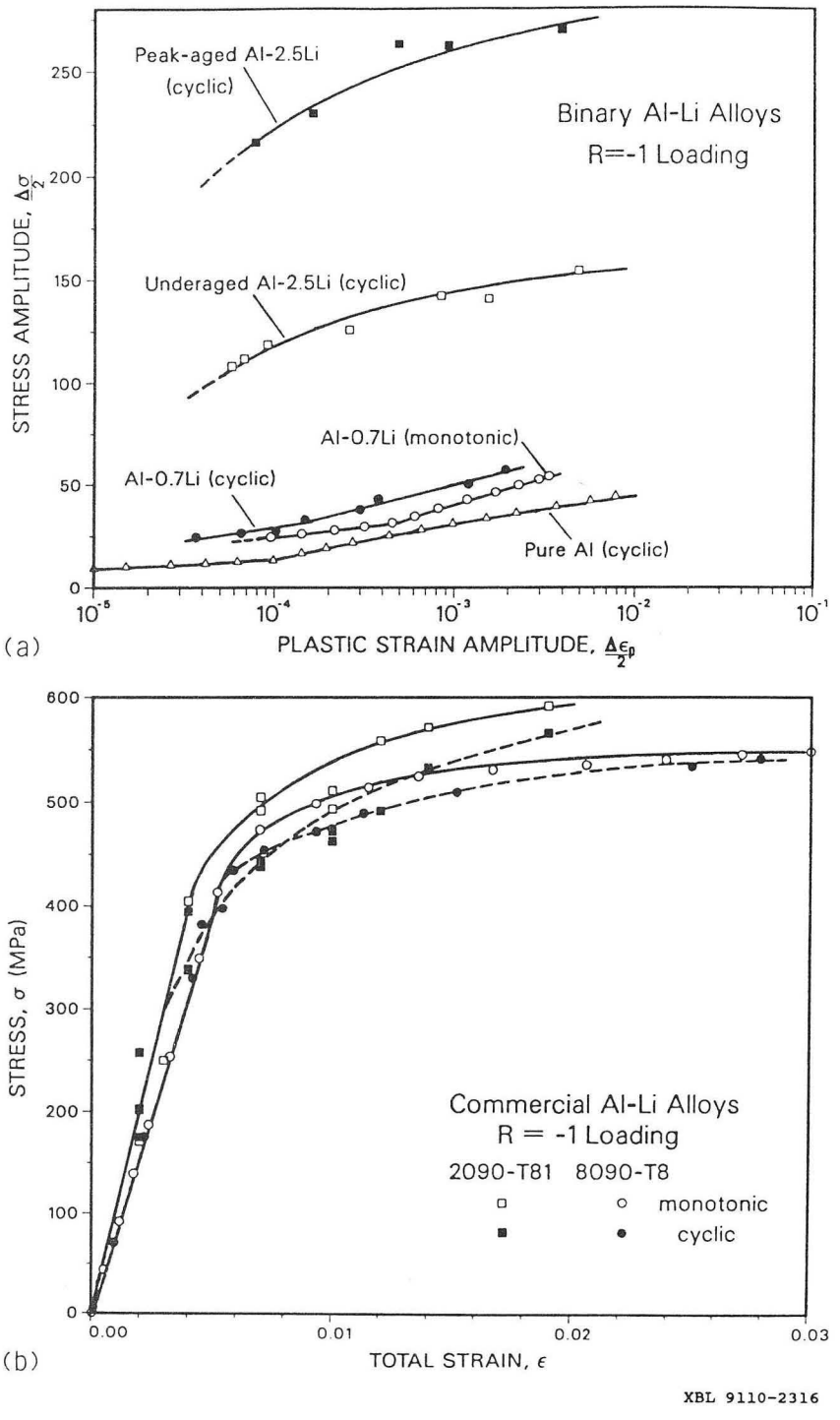

Fig. 4: Monotonic and stabilized cyclic stress-strain curves for (a) various binary Al-Li alloy microstructures and (b) commercial 2090-T81 and 8090-T8 alloys (longitudinal direction, R = -1) (57,67,85).

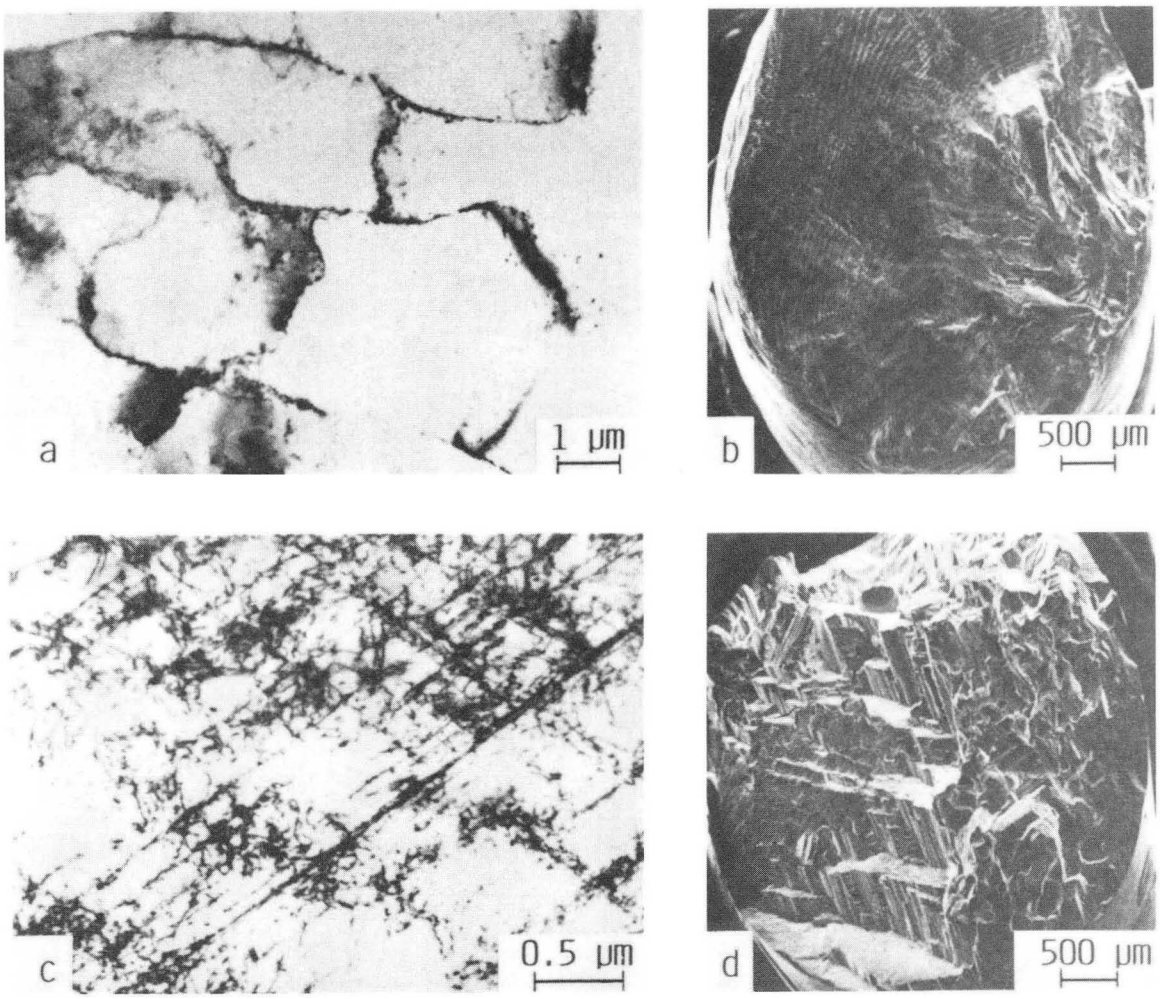

XBB 912-642

Fig. 5: TEM micrographs of dislocation substructures generated during cyclic deformation (a,c), and corresponding SEM images of fatigue fracture surfaces (b,d), in binary Al-Li alloys hardened by, (a,b) Li in solid solution (underaged Al-0.7 wt. %Li alloy), and (c,d) ordered δ' (Al_3Li) precipitates (peak-aged Al-2.5 wt. %Li). Failures in the solid solution occur by ductile striated-type mechanism corresponding to homogeneous, cellular deformation structures, whereas δ'-hardened structures fracture by slip-band cracking due to localized deformation along close-packed {111} planes (34,57).

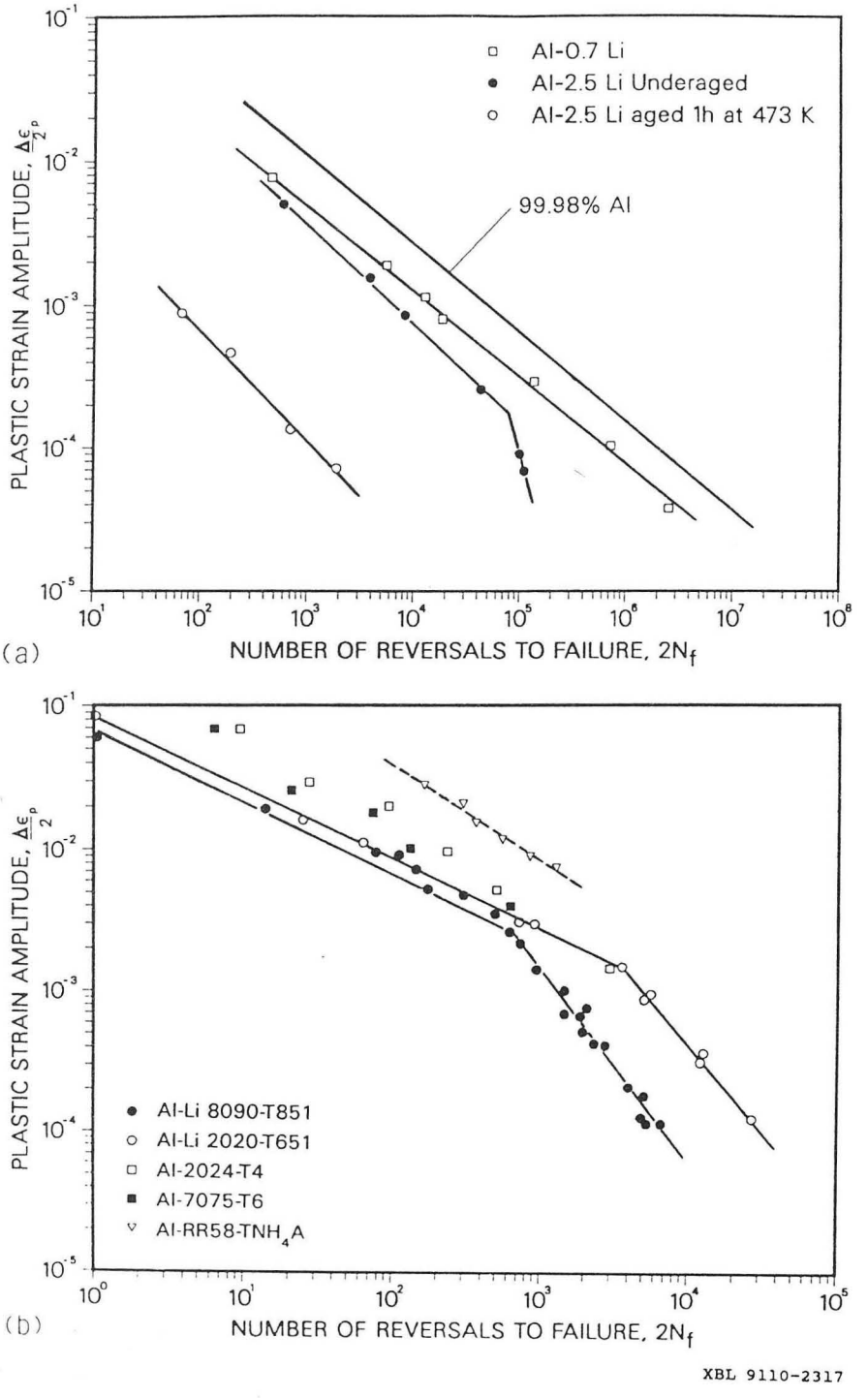

Fig. 6: Comparison of the Coffin-Manson relationships for different (a) binary and (b) commercial 8090 and 2020 Al-Li alloys, compared to pure aluminum and traditional 2000 and 7000 series aluminum alloys in the longitudinal orientation. Note that Li present as δ' particles, is detrimental to LCF resistance. Data taken from Refs. 34,57,85.

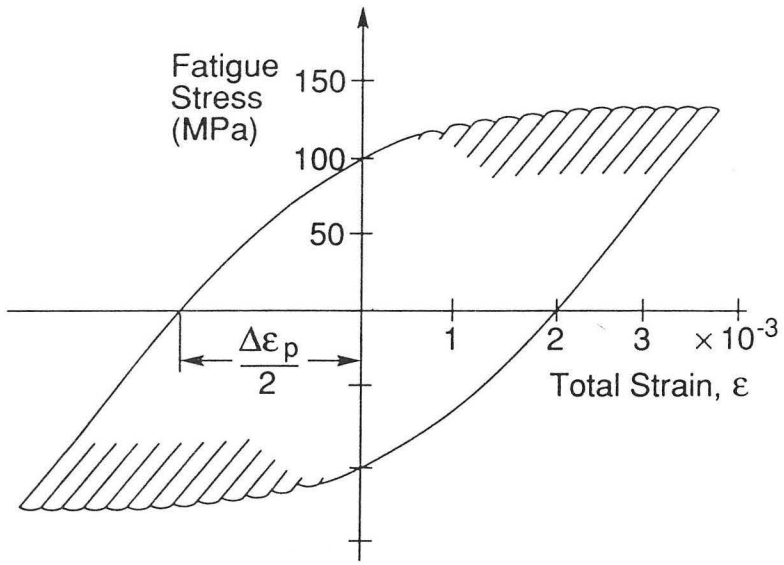

XBL 9110-2326

Fig. 7: Illustration of the fatigue stress instabilities observed on the stabilized cyclic stress-strain hysteresis loop of Al-2.5Li alloy, aged for 5 h at 423 K. Results are for a plastic strain amplitude $\Delta\epsilon_p/2 = 2x10^{-3}$ (0.01 Hz) at room temperature (89).

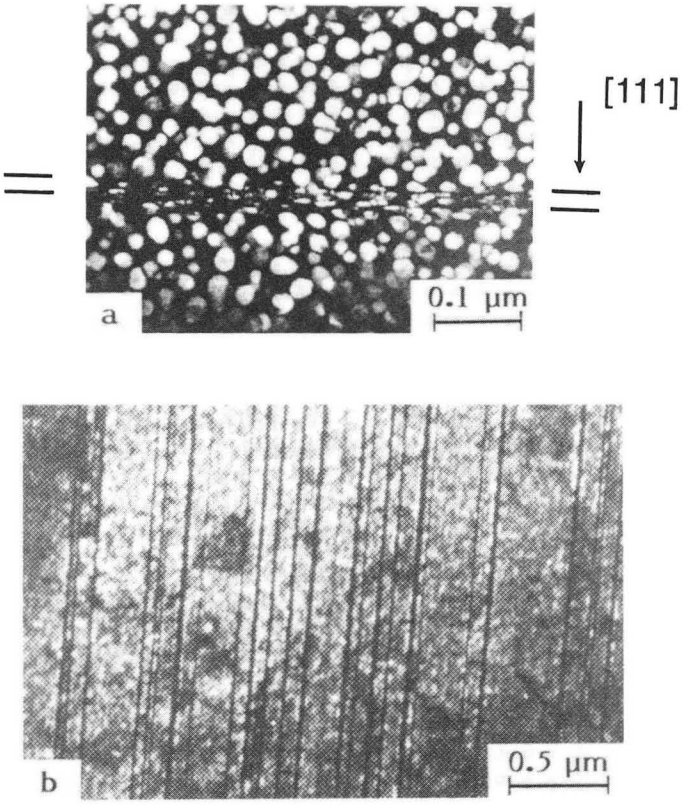

XBB 912-641

Fig. 8: Dark-field TEM micrographs showing (a) shearing of ordered δ'particles during early stages of cyclic deformation (as seen in a peak-aged 8090 Al-Li alloy, $\Delta\epsilon_p/2 = 0.5\%$, from Ref. 84) and (b) fatigue-induced, δ'-precipitate-free bands parallel to {111} slip bands in binary Al-Li alloys (Al-2.5wt.%Li, aged for 8 h at 373 K; mean diameter of δ' particles ~2 nm, from Ref. 90). Imaging performed using δ'-superlattice reflections.

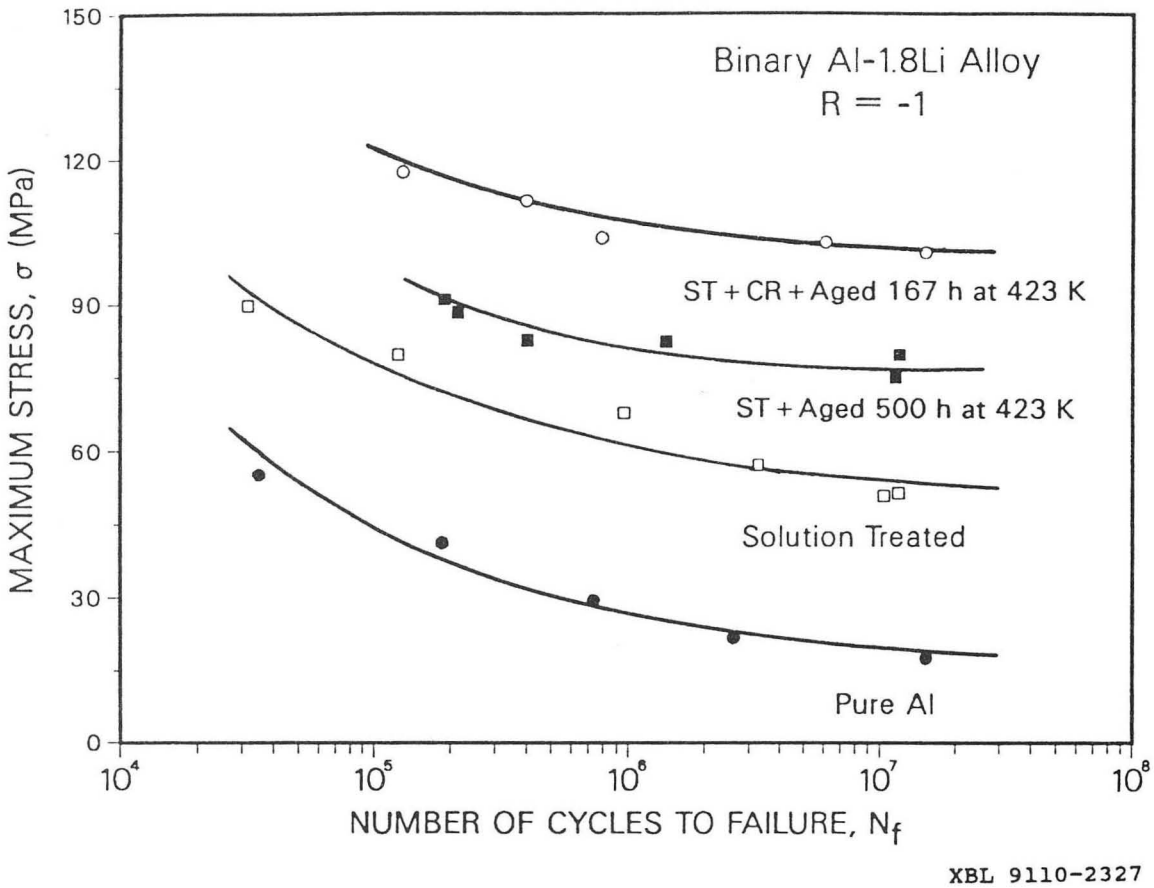

Fig. 9: High-cycle fatigue curves for a binary Al-1.8 wt. % Li alloy, following various thermomechanical treatments compared to pure aluminum. Results shown are for smooth, 2.3 mm thin-sheet specimens, tested under fully-reversed (R = -1) bending fatigue parallel to the rolling direction, taken from Ref. 92. ST and CR refer to solution treatment and 67% cold rolling, respectively.

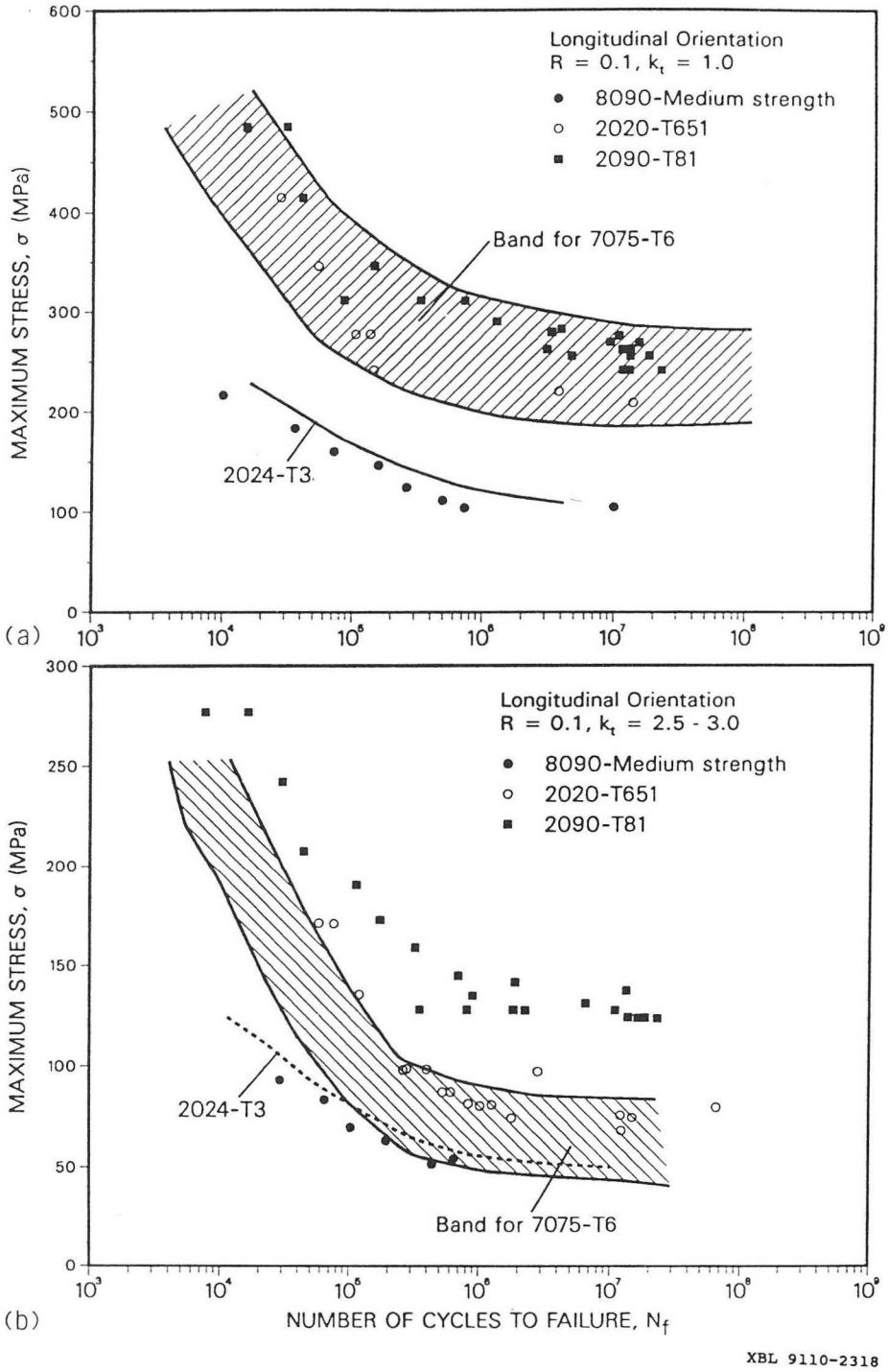

Fig. 10: Comparison of (a) smooth unnotched (stress-concentration factor, k_t = 1), and (b) notched (k_t = 3) fatigue-crack initiation resistance under axial loading conditions (R = 0.1) for various commercial Al-Li and conventional aluminum alloys. HCF resistance of Al-Li alloys is comparable to 2000 and 7000 series aluminum alloys. Results compiled from Refs. 97,98.

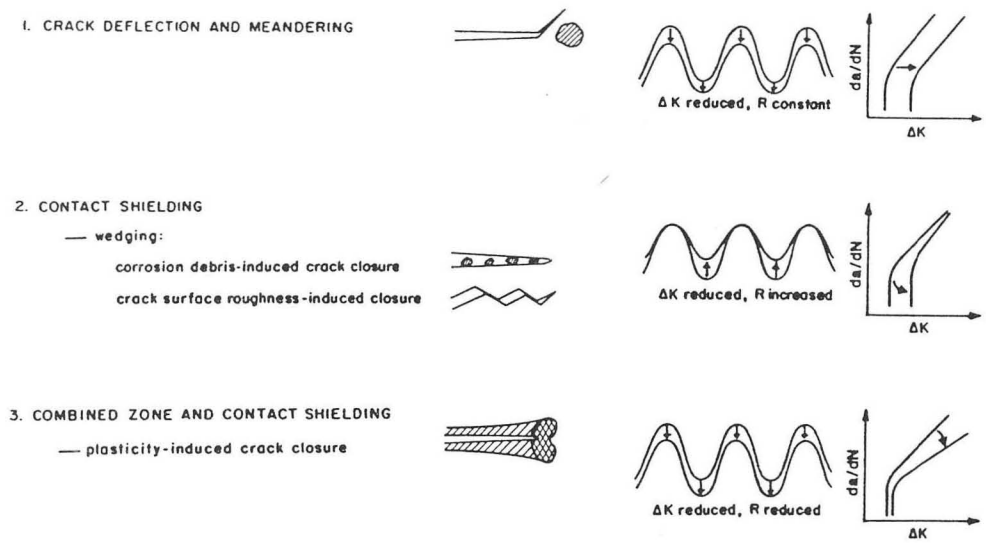

XBL 871-84

Fig. 11: Schematic illustration of the crack-tip shielding mechanisms influencing fatigue-crack propagation in high-strength aluminum alloys, showing primary mechanisms and their consequences to crack growth-rate behavior (123).

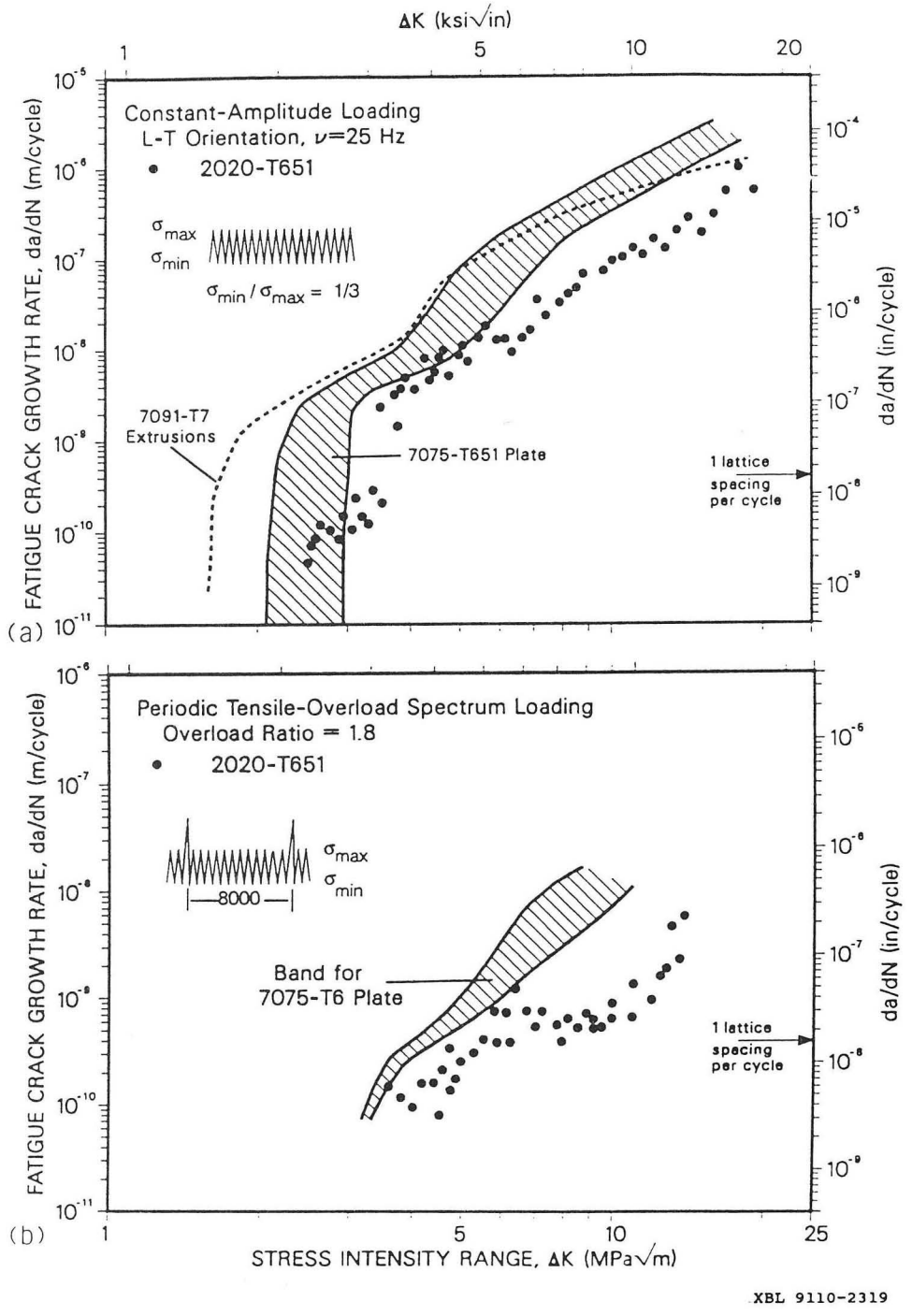

Fig. 12: Fatigue-crack propagation behavior in peak-aged 2020-T651 alloy compared with I/M 7075-T651 and P/M 7091-T7E69 alloys, under (a) constant-amplitude and (b) periodic single-spike overload spectrum loading. Note that growth rates in 2020 are significantly slower, particularly at near-threshold stress-intensity levels and under tension-dominated spectrum loading (98).

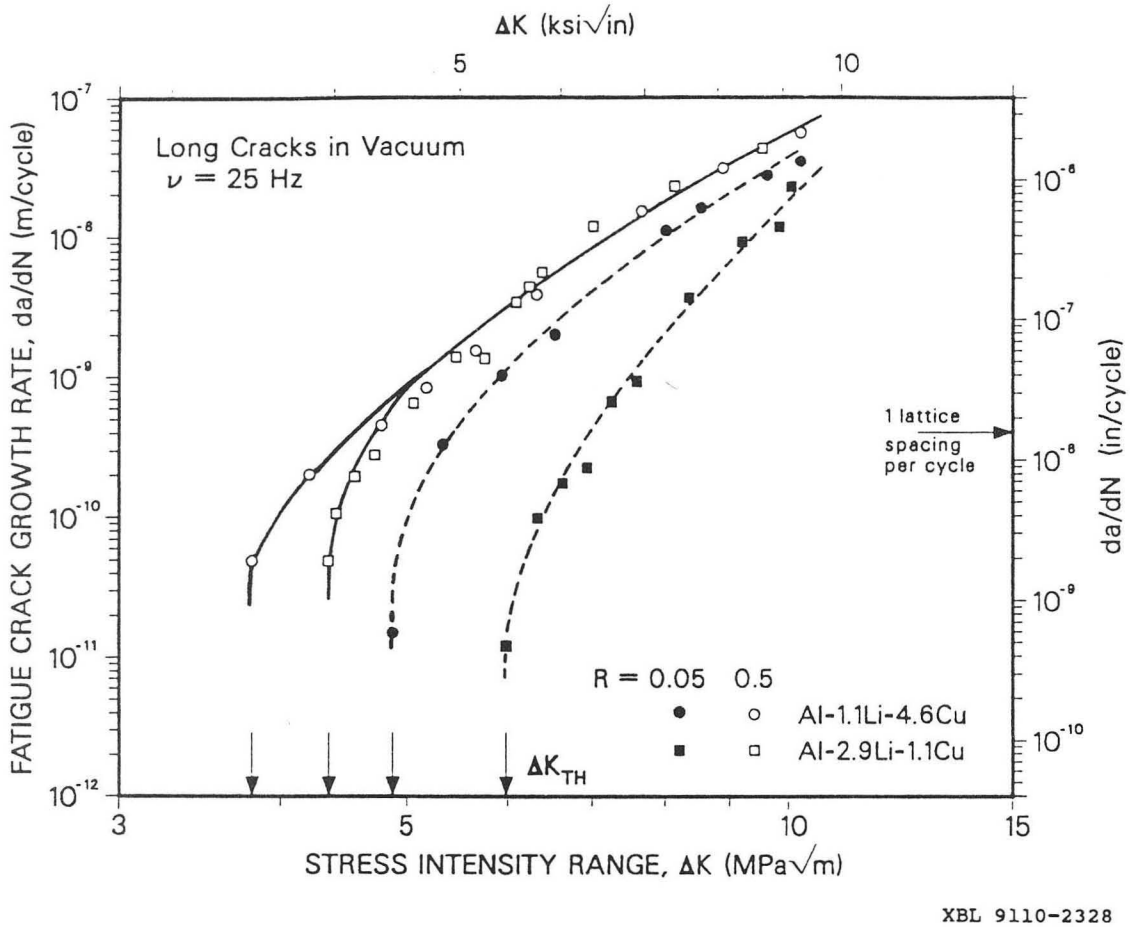

Fig. 13: Growth-rate behavior of long fatigue-cracks in experimental Al-Li-Cu-Zr alloys under constant-amplitude loading for R = 0.05 and 0.5 *in vacuo* at room temperature. Note that increasing the Li:Cu ratio leads to slower crack velocities, particularly at low R (119).

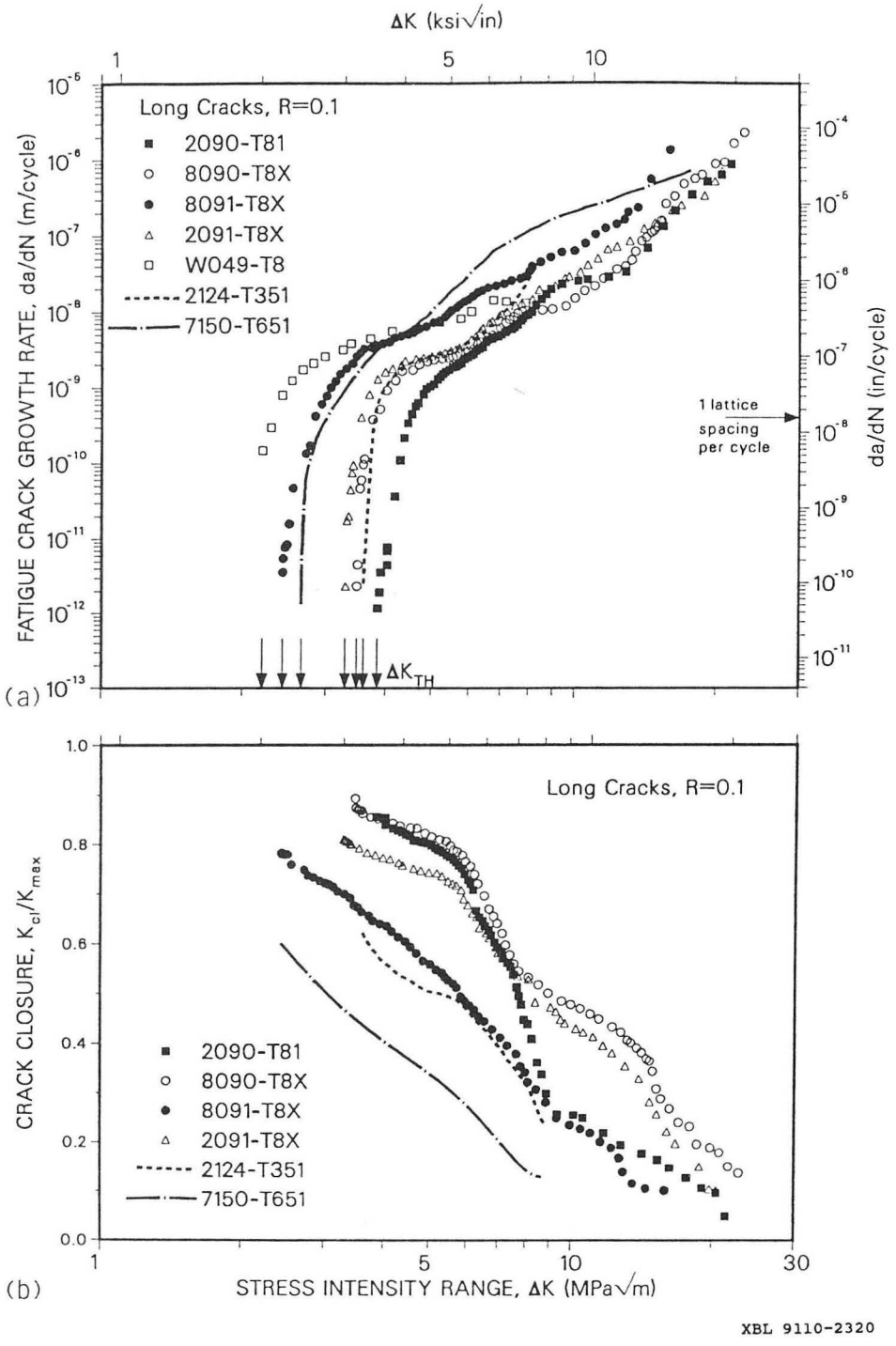

Fig. 14: Constant-amplitude (a) fatigue-crack growth rates and (b) corresponding crack-closure levels for long cracks in peak-aged commercial Al-Li and traditional Al alloys in plate form (L-T orientation, R = 0.1, moist ambient-air environment, using 6.4 mm thick specimens, t/2 location). Growth-rate behavior in Al-Li alloys is superior to traditional aluminum alloys consistent with the higher crack-closure levels (124).

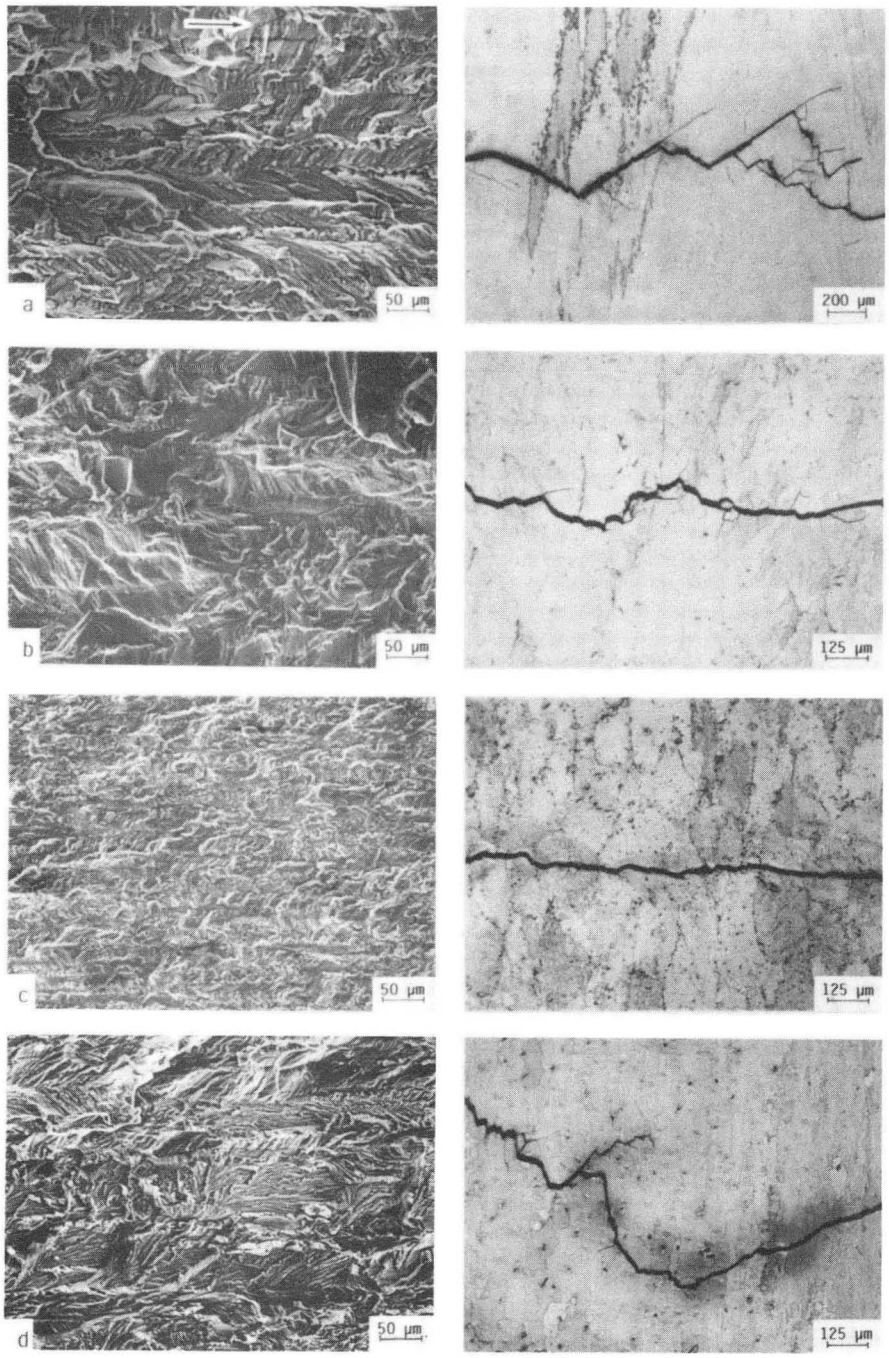

XBB 883-2387A

Fig. 15: SEM and optical micrographs of fatigue fracture surfaces and crack-path morphologies, respectively, in (a) 2090-T81, (b) 8090-T8, (c) 8091-T8 and (d) 2091-T8 (L-T orientation, R = 0.1, t/2 location) at ΔK levels between 6 to 8 MPa$\sqrt{m}$. Note the rough fracture surfaces and deflected crack paths in 2090, 8090 and 2091, compared to the relatively flat surface and linear crack path in fine-grained 8091. Arrow indicates the general direction of crack growth (124).

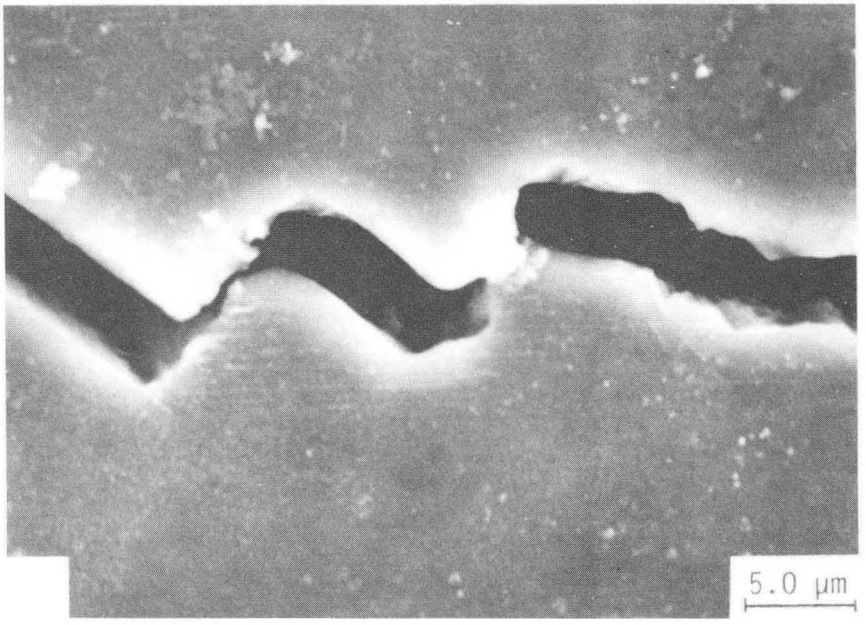

XBB 878-6961 (top)

Fig. 16: Meandering fatigue-crack paths and resultant wedging of fracture-surface asperities (termed roughness-induced crack closure) in the plane of loading for Al-Li alloys. Micrograph obtained from the specimen surface of 2090-T81 in L-T orientation; horizontal arrow indicates general direction of crack advance (124).

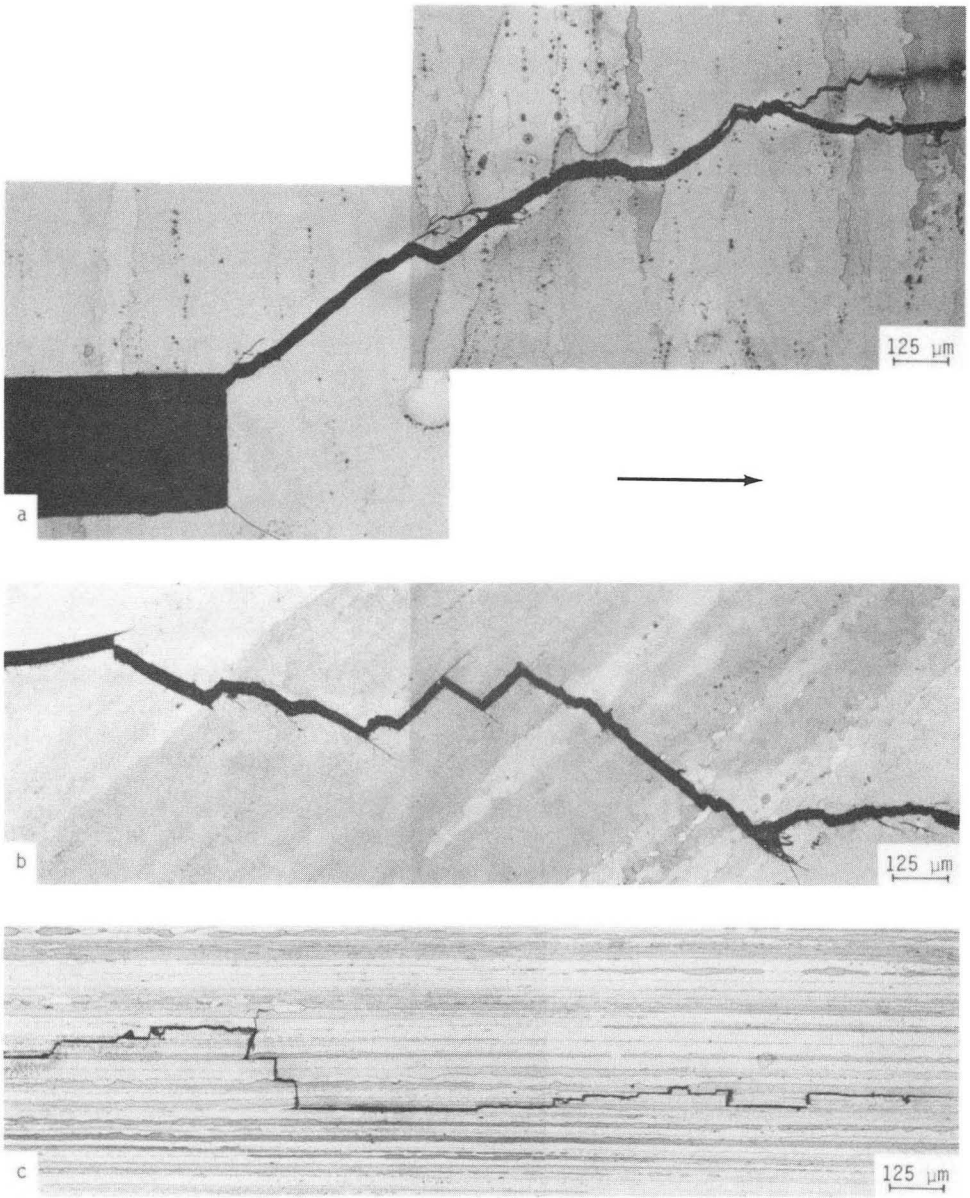

XBB 869-7356

Fig. 17: Various modes of non-linear cracking morphologies observed during fatigue-crack propagation in commercial Al-Li alloys, showing (a) macroscopic crack branching, (b) crack meandering (crystallographic slip-band cracking), and (c) intergranular delamination (short-transverse) cracking. Micrographs taken for 2090-T81 plate. Arrow indicates the crack-growth direction (123).

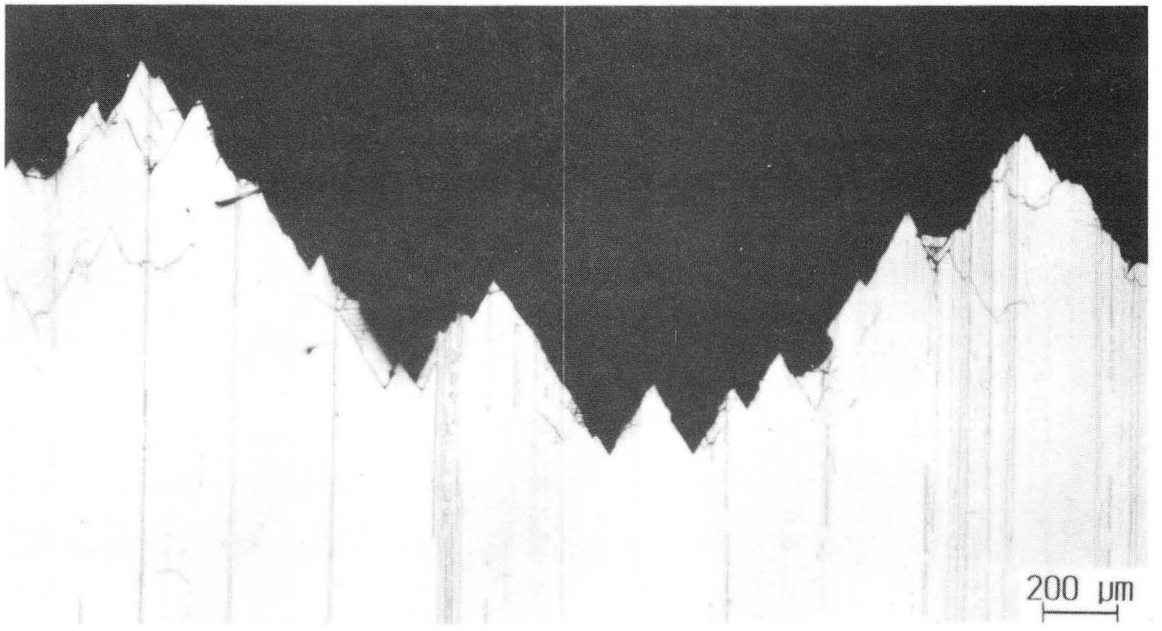

XBB 912-640

Fig. 18: Crystallographic crack-path tortuosity through the specimen thickness observed during fatigue-crack growth in Al-Li alloys induced by pronounced deformation texture. The sharp facets with an included angle of $\sim 60°$ are a result of shearing along intersecting (111) planes across several high-angle grain boundaries. Micrograph obtained for 2090-T81 plates (L-T orientation) at the mid-section thickness normal to the crack-growth direction and crack-growth plane. ΔK = 8-10 MPa$\sqrt{m}$. Crack growth direction is into the page.

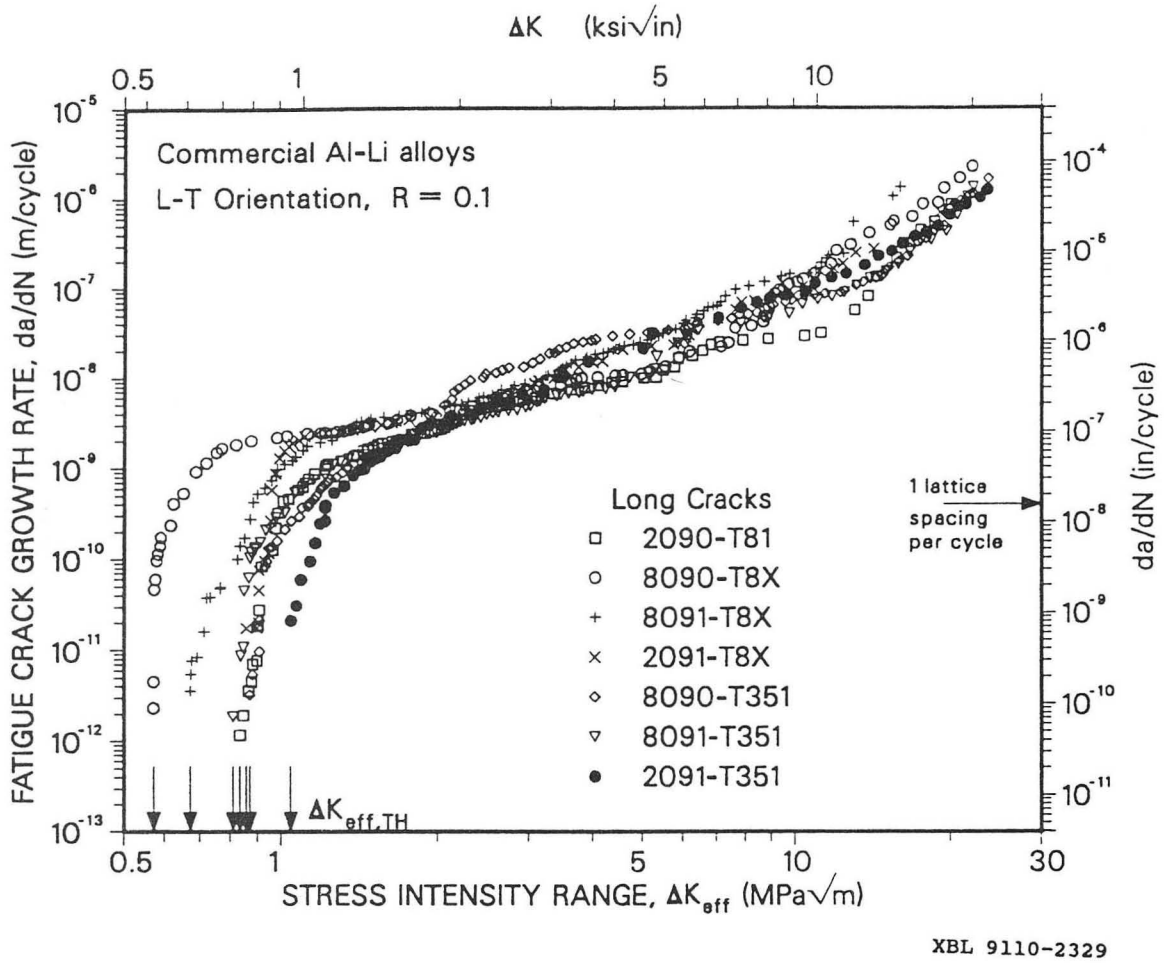

Fig. 19: Intrinsic fatigue-crack propagation resistance of various commercial Al-Li alloy microstructures in moist-air environments obtained using variable-ΔK/constant-R (= 0.1) schemes and plotted in terms of ΔK_{eff}, after correcting for closure (124). Note that growth-rate differences between the alloys are reduced compared to results presented in Fig. 14.

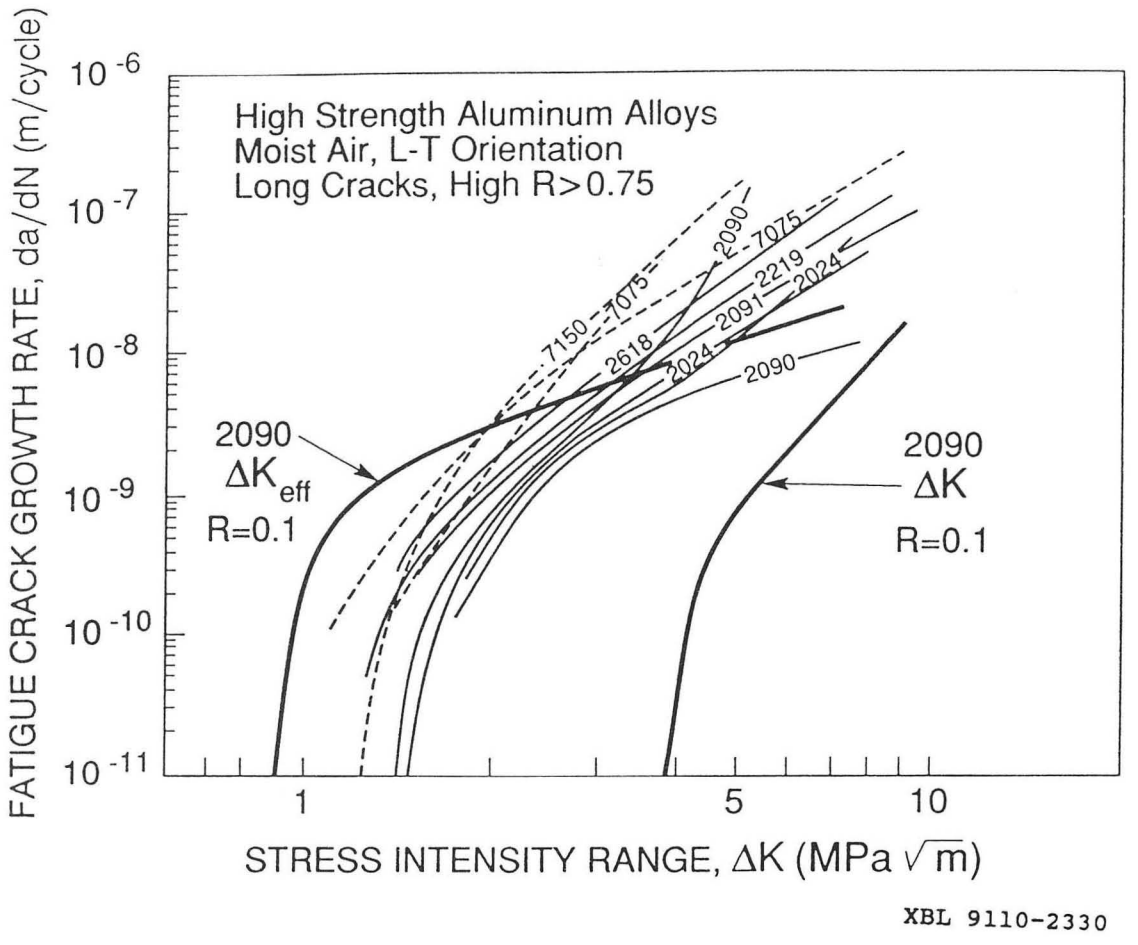

Fig. 20: Intrinsic fatigue-crack propagation rates in commercial Al-Li, 2000 and 7000 series high-strength aluminum alloys in moist air, obtained by using constant-K_{max}/variable-R loading techniques (R increases from 0.1 at the highest ΔK to about 0.9 at ΔK_{TH}) or by measuring crack-growth rates at high R (133-135). All alloys show comparable fatigue resistance; the 7000 series alloys are slightly more sensitive to environment.

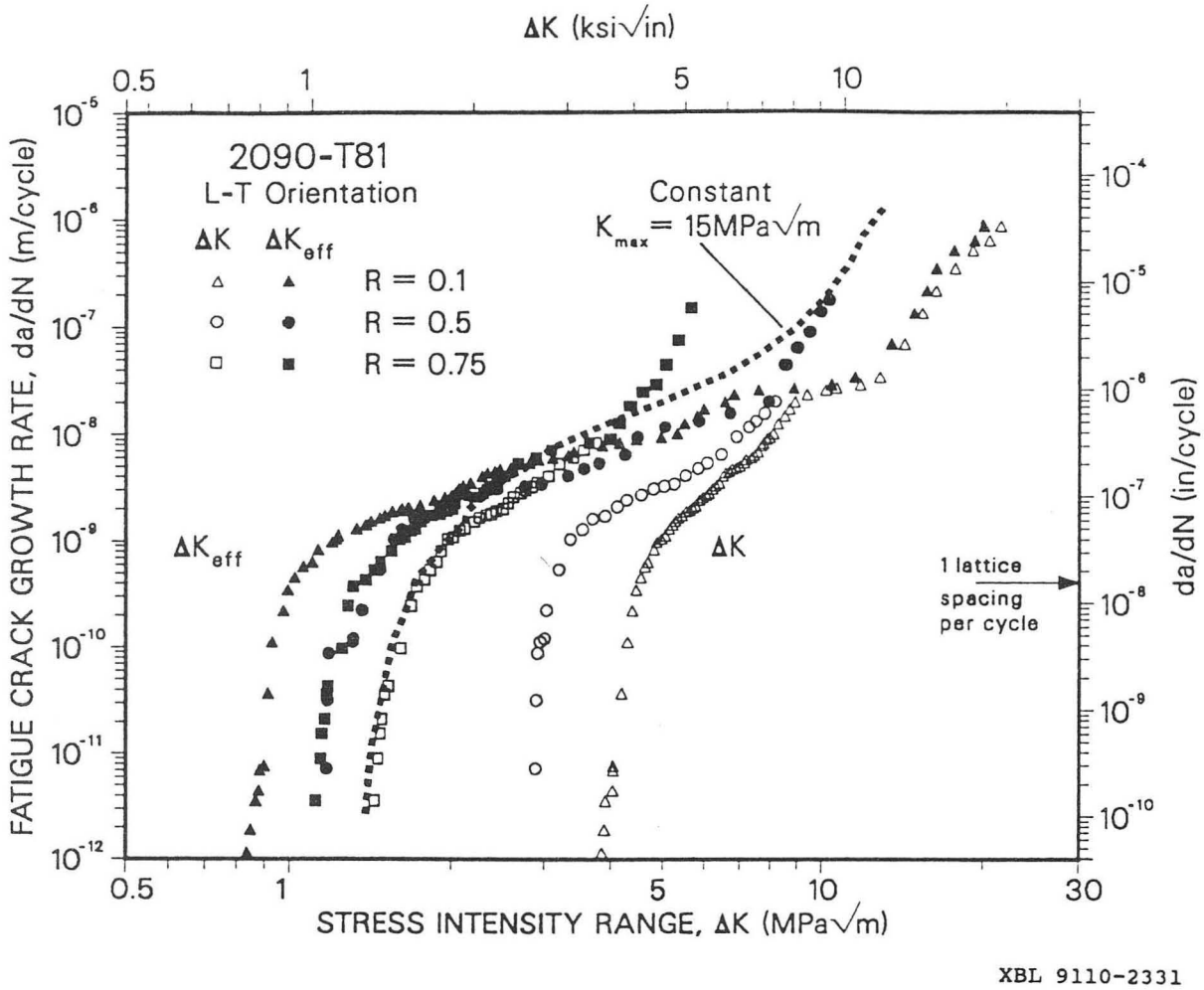

Fig. 21: Influence of load ratio, R, on the (long) crack-extension rates in 2090-T81, as a function of ΔK and ΔK_{eff}; results obtained using constant-K_{max}/variable-R schemes (K_{max} = 15 MPa$\sqrt{m}$, R = 0.1-0.9) are also compared. Note that differences in growth-rates with respect to R are reduced when data are characterized using the ΔK_{eff} or determined using the constant-K_{max}/variable-R approach (123,131-133).

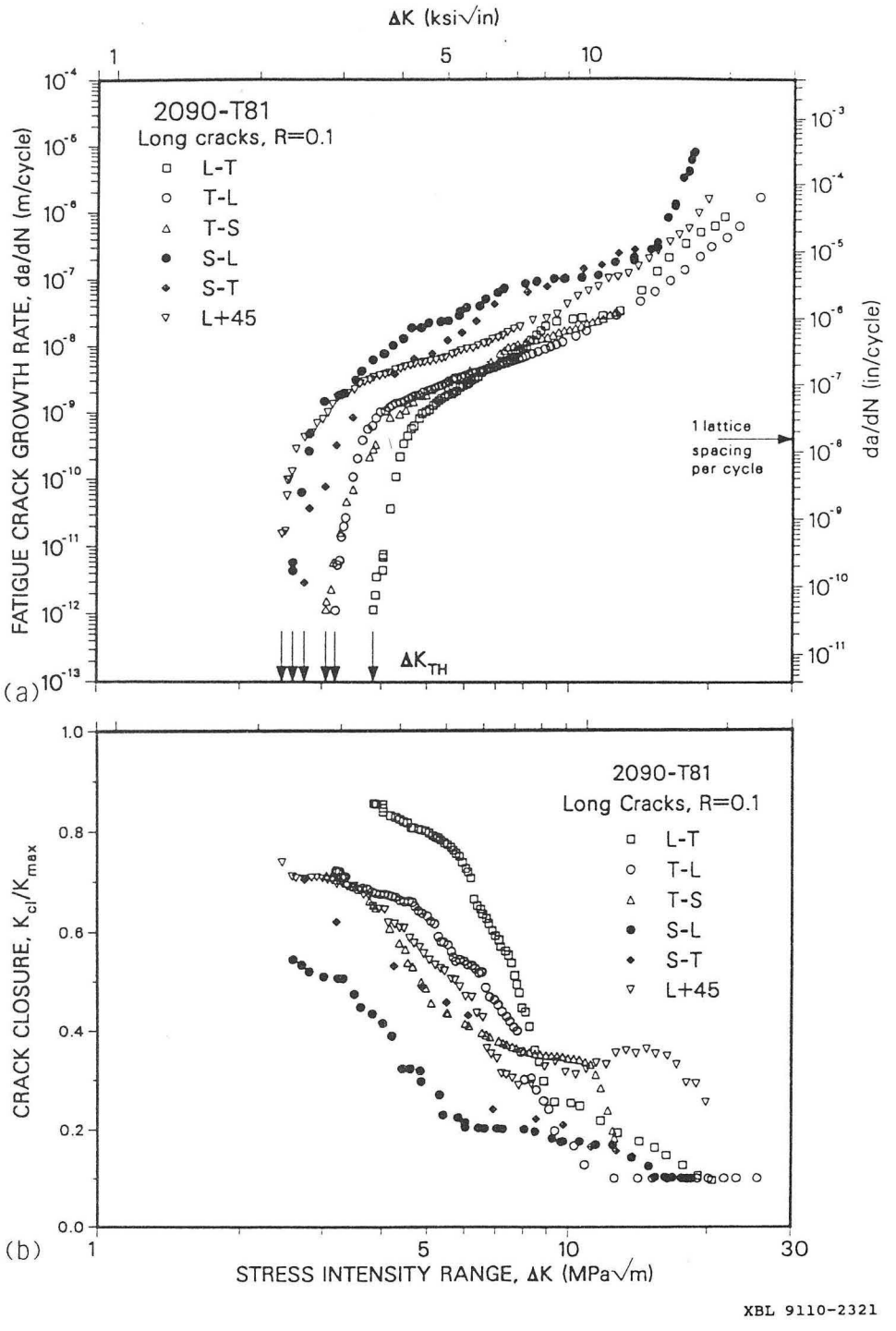

Fig. 22: Variation in (a) fatigue-crack extension rates and (b) crack-closure levels for long cracks in 2090-T81 alloy at R = 0.1, as a function of specimen orientation. Note how growth-rates parallel to the rolling plane (S-L, S-T) are the fastest, whereas growth rates normal to the rolling plane (L-T, T-L, T-S) are the slowest, consistent with the non-linearity of crack-path morphologies and resulting levels of crack closure (123).

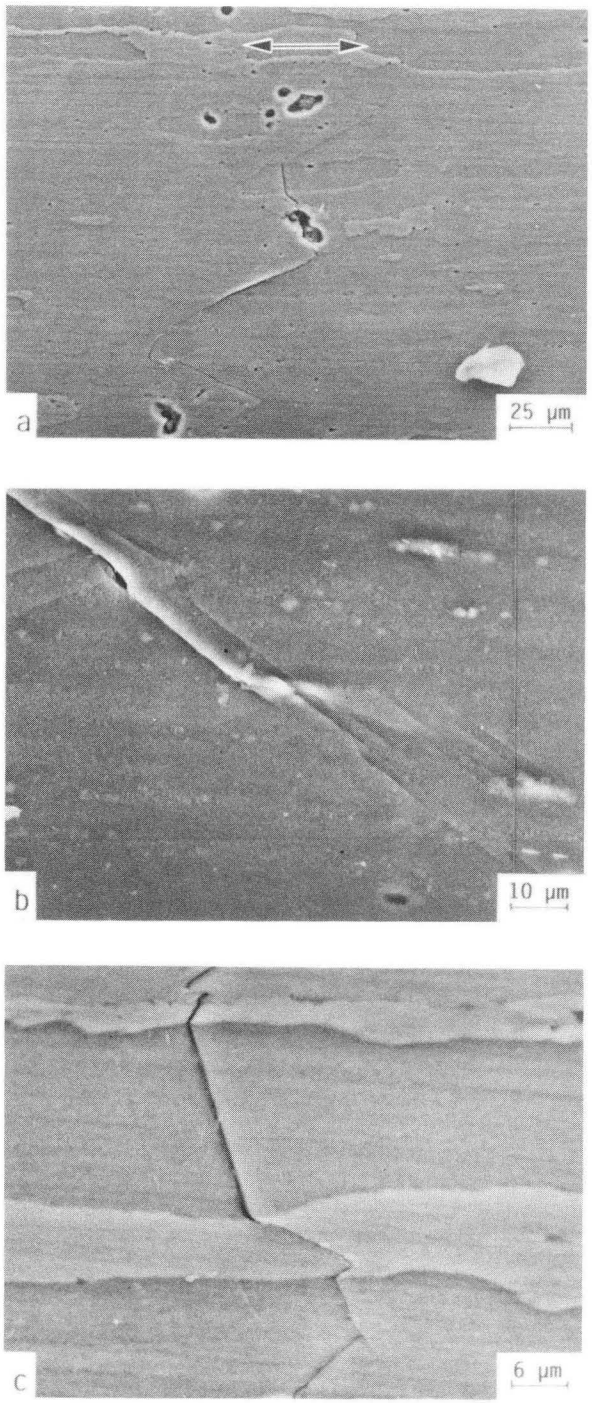

XBB 885-4510

Fig. 23: SEM micrographs illustrating the growth morphology of naturally-occurring, microstructurally-small (2-1000 μm) surface fatigue-cracks in Al-Li alloys. As shown in (a), they initiate at local heterogeneities in the microstructure, propagate by periodically deflecting (b) along intersecting slip bands, and (c) at grain boundaries. Micrographs were obtained from gold coated cellulose-acetate replicas of the specimen surface for 2090-T81. Horizontal arrow represents the direction of loading (124).

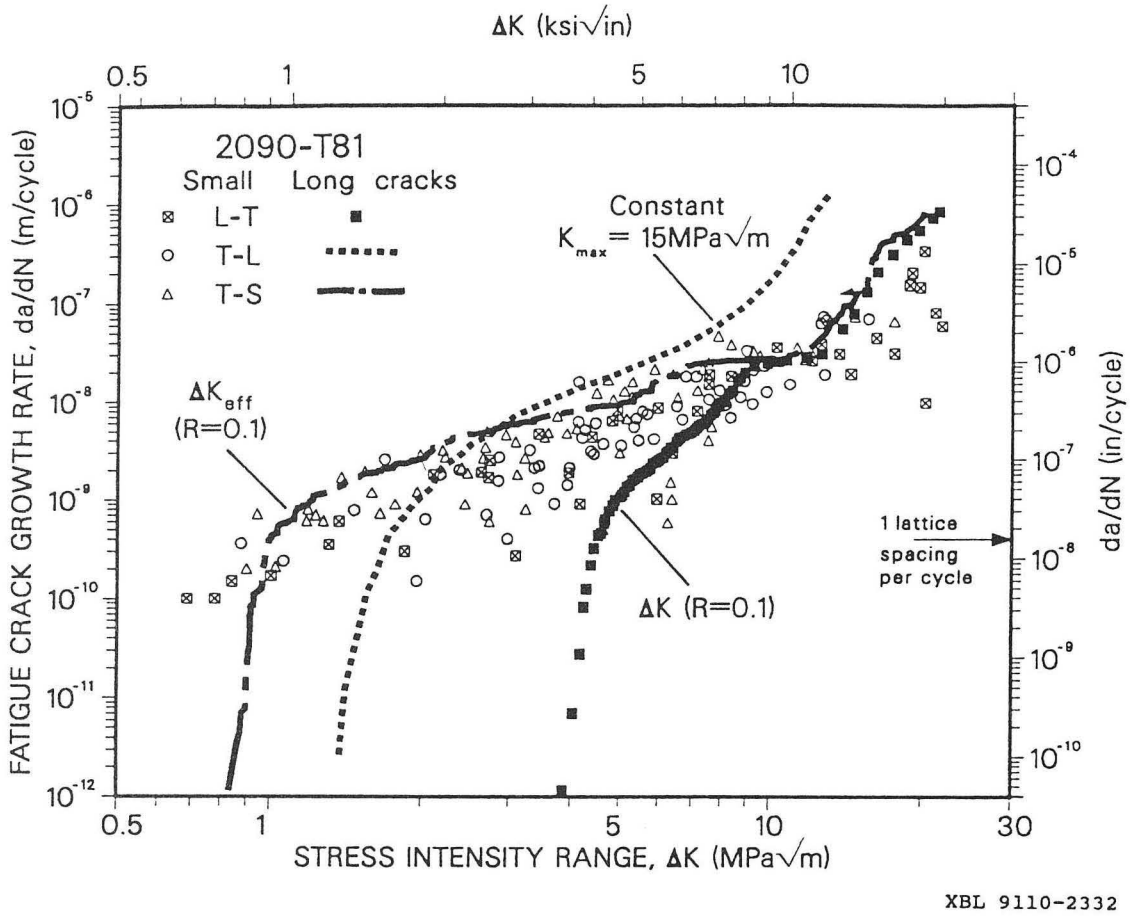

Fig. 24: Growth-rate behavior of microstructurally-small (2-1000 μm) surface, and long (> 10 mm) fatigue cracks in peak-aged 2090 Al-Li alloy. Note that at ΔK levels below 7-8 MPa$\sqrt{m}$, small-crack velocities are nearly 2-3 orders of magnitude faster than long crack da/dN at R = 0.1. Closer correspondence between long and small-crack data is seen when long-crack results are characterized using ΔK_{eff} or measured using constant-K_{max}/variable-R schemes (142,149).

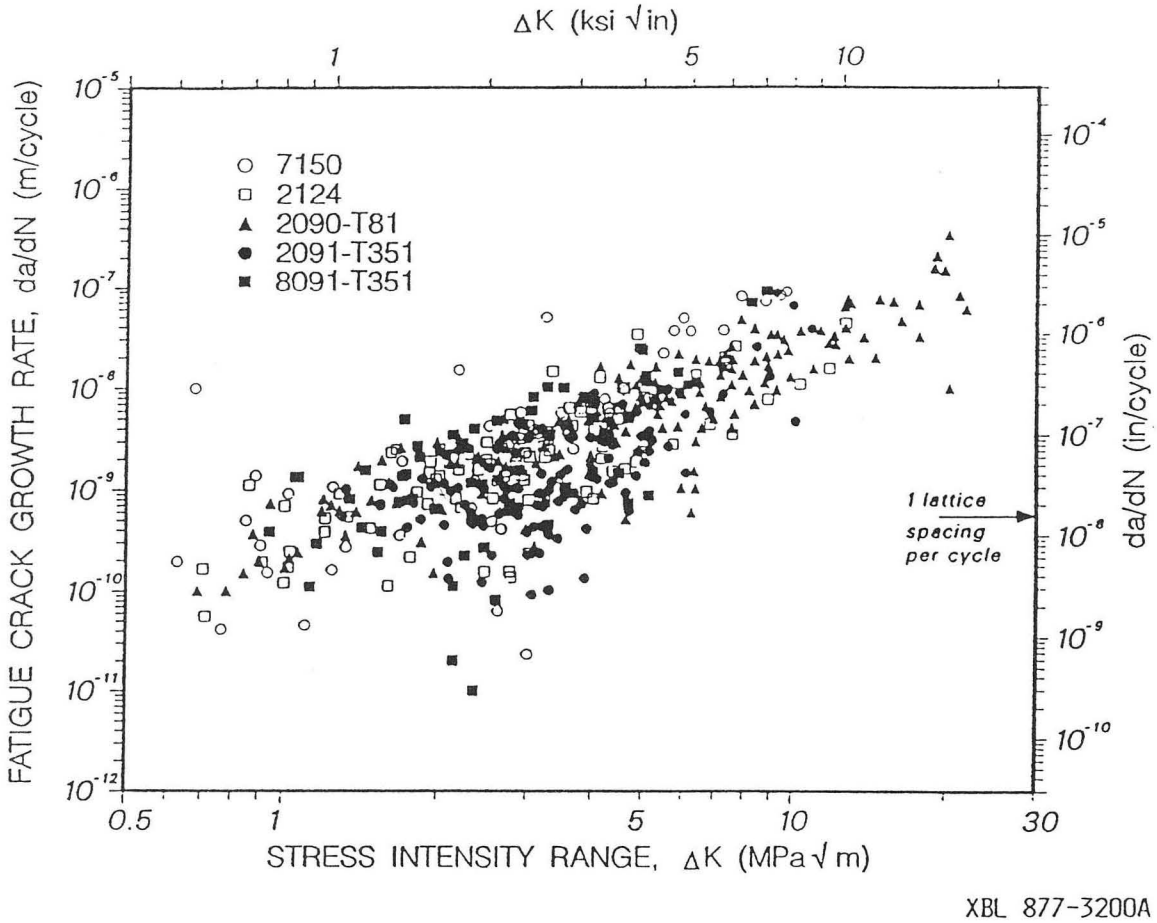

Fig. 25: **Growth-rate response of naturally-occurring, microstructurally-small surface cracks in commercial Al-Li and traditional alloys. Note that the results show no apparent influence of microstructure and composition; small-crack resistance of Al-Li alloys remains comparable to other high-strength aluminum alloys (151).**

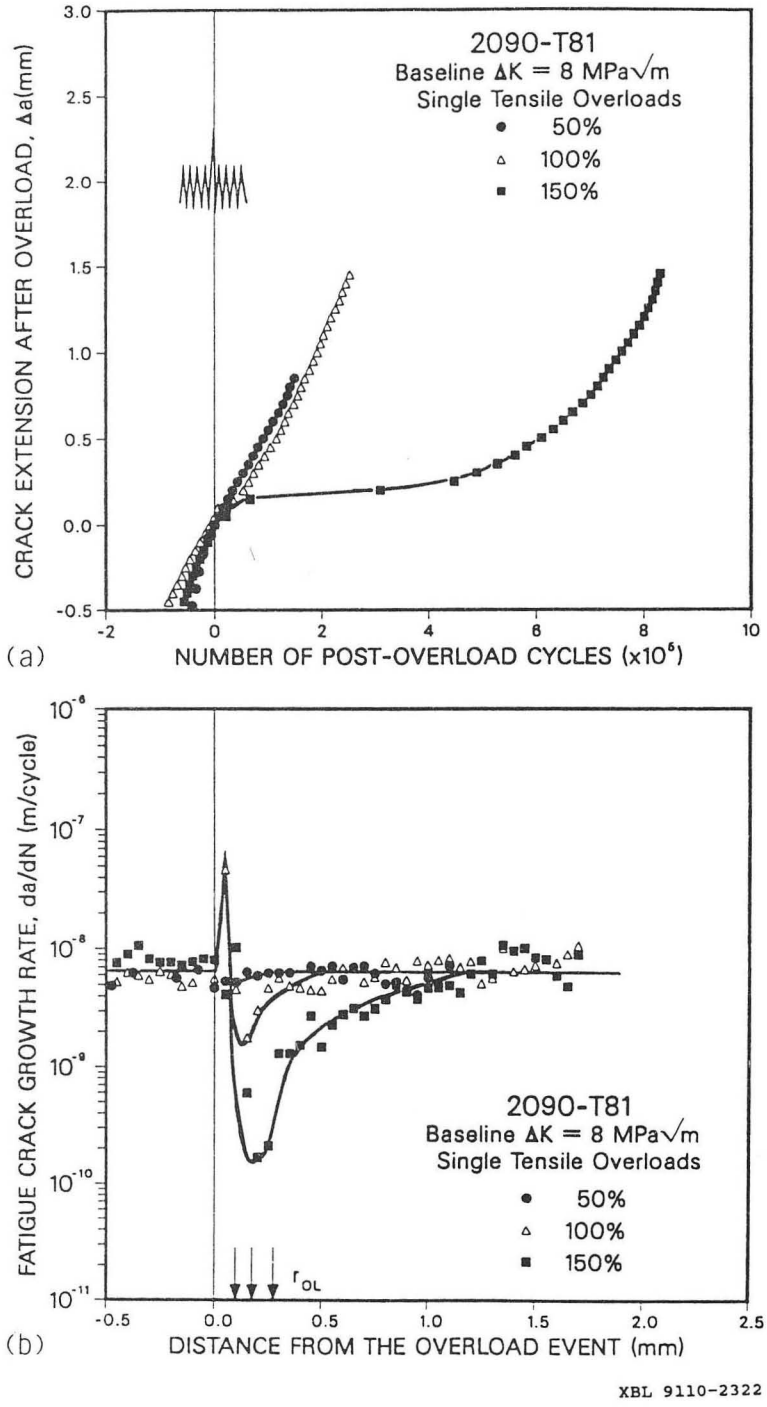

Fig. 26: Transient fatigue (a) crack-growth and (b) growth-rate response, as a function crack extension, following tensile overloads in 2090-T81 (L-T orientation) at a constant baseline ΔK of 8 MPa$\sqrt{m}$. Retardation distances following the overload are typically 2-3 times the computed maximum overload plastic-zone sizes, r_{oL}, as indicated by the vertical arrows (151).

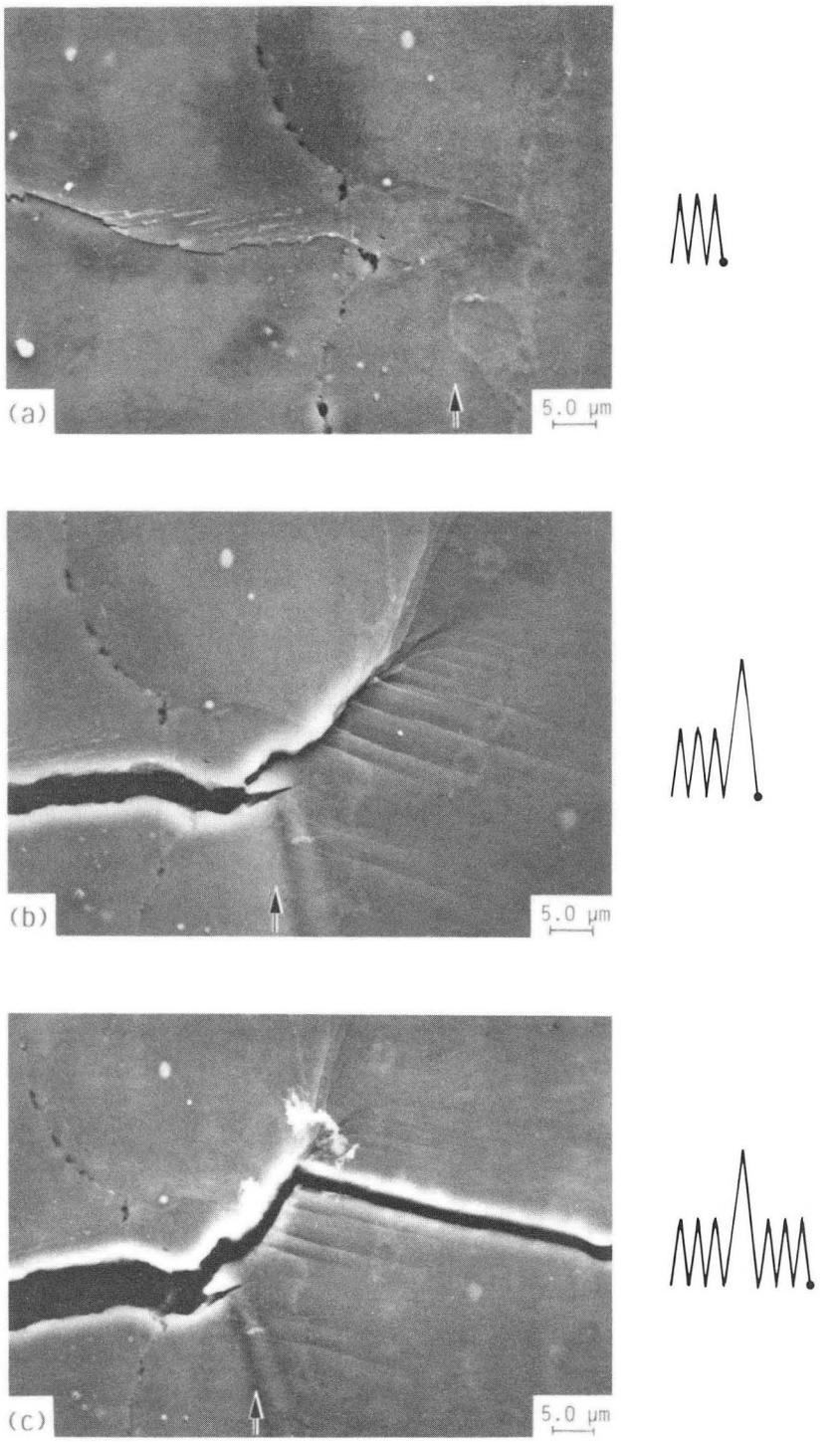

Fig. 27: SEM images of the surface fatigue-crack morphology, showing the crack tip (a) prior to, (b) at, and (c) after a 100% single peak tensile overload in 2090-T81 at a baseline ΔK level of 8 MPa$\sqrt{m}$ ($R = 0.1$). Imaging was performed after unloading; the vertical arrows indicate the position of the overload event (151).

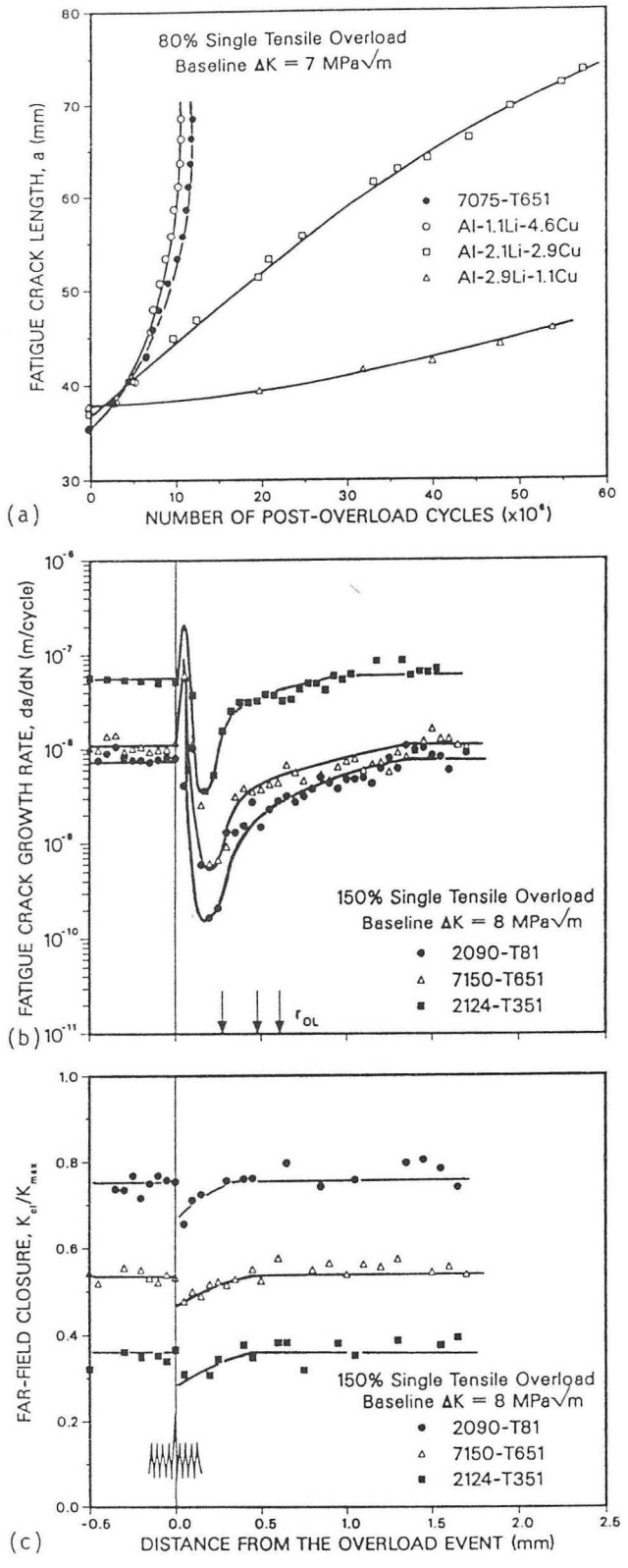

XBL 911-157

Fig. 28: Post-overload fatigue-crack propagation behavior following single tensile overloads in Al-Li alloys compared to other aluminum alloys, characterized in terms of (a) crack extension, (b) crack-growth rates and (c) far-field crack-closure levels. Note the greater delay periods and retardations in higher Li-containing alloys, and specifically 2090, consistent with the higher closure levels (119,151).

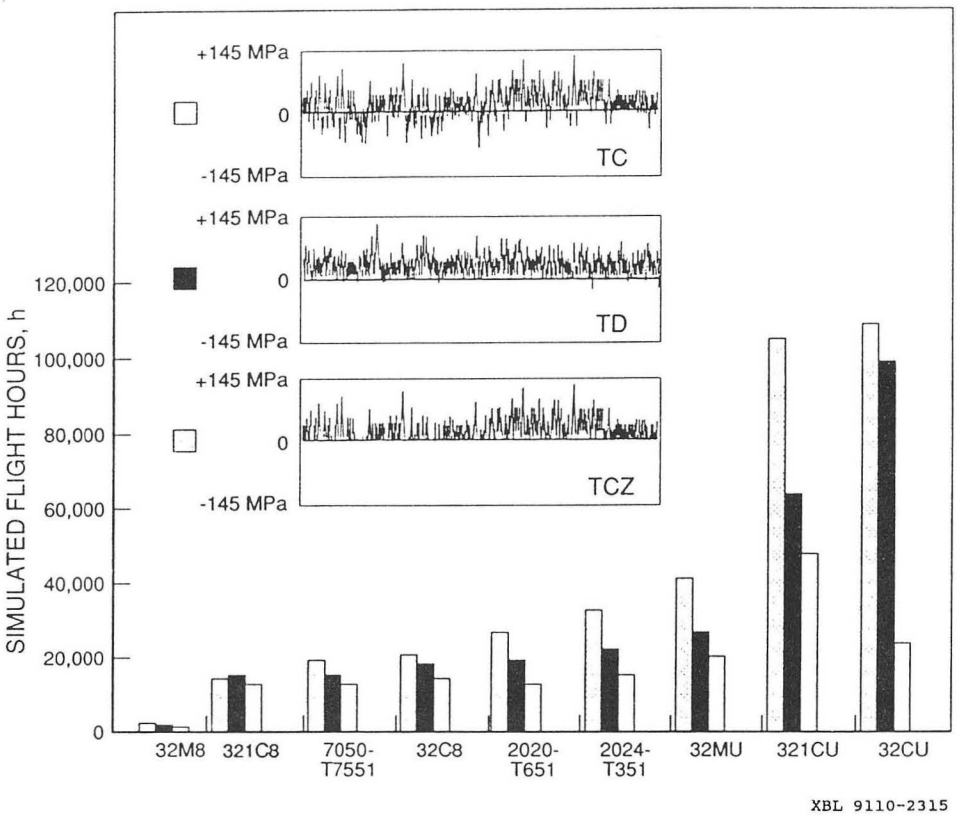

Fig. 29: Comparison of spectrum fatigue lifetimes (in simulated flight hours) for experimental Al-Li-Cu, 2020-T651, 2024-T351 and 7050-T7551 aluminum alloys, under tension-dominated (TD), tension-compression-dominated (TC), and modified tension-compression dominated (TCZ) loading. Estimated lives are based on the growth of a 6 mm flaw to final failure, for maximum peak stresses below 145 MPa. Note that Al-Li alloys show remarkable improvements in lifetimes under TD spectrum loading over 2024 and 7050; behavior under TC spectrum loading remains comparable (159,160). (3, 2, and 1 refer to alloy composition, namely, Al with 3 wt% Cu, 2 wt% Li and 1 wt% Mg, respectively; C and M refer to coarse and mixed grain structures, respectively; U and 8 denote underaged and peak-aged tempers.)

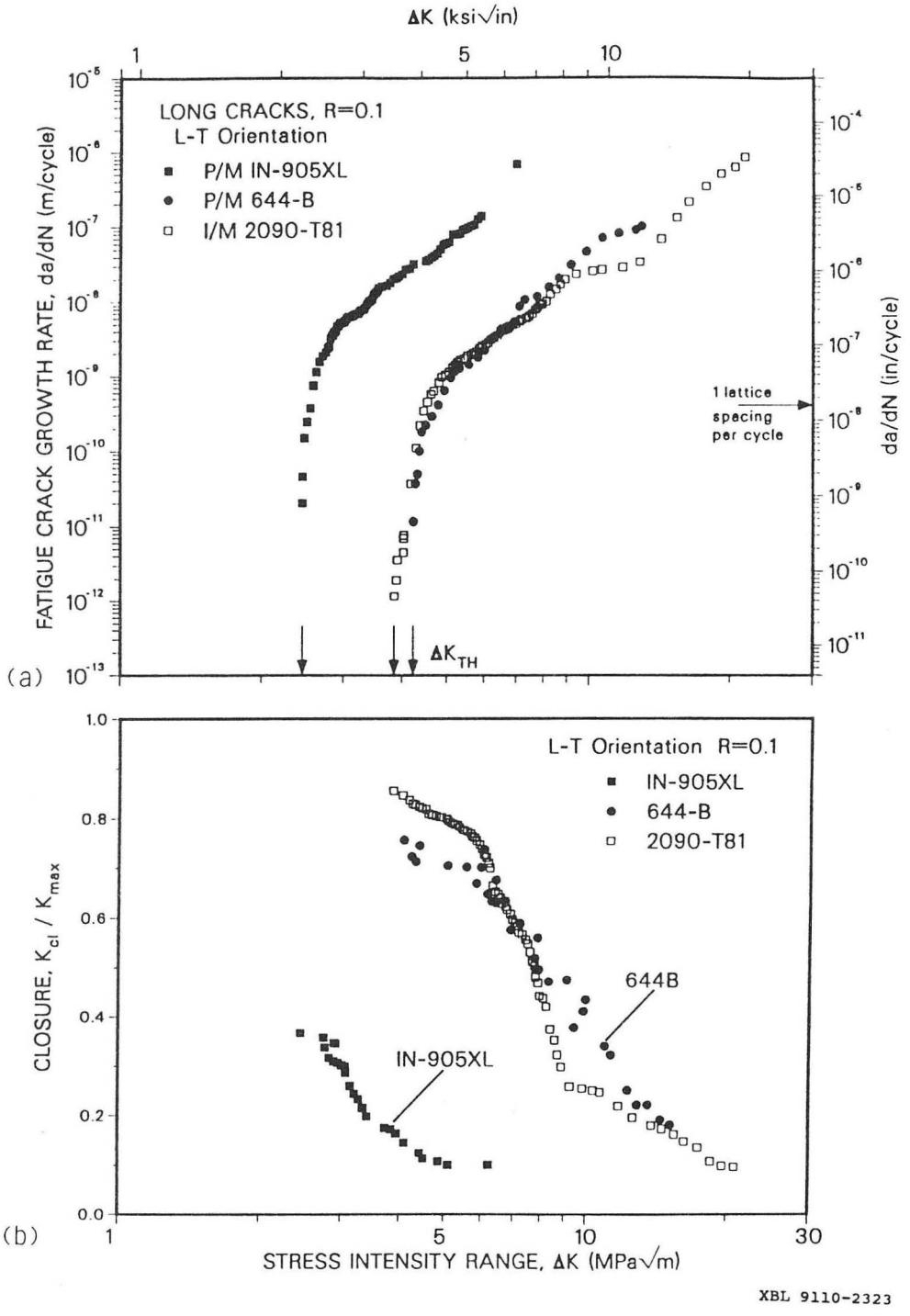

Fig. 30: Constant-amplitude (a) fatigue-crack propagation and (b) crack-closure behavior in P/M Al-Li extrusions processed via rapid solidification (Allied-Signal 644-B alloy) and mechanical alloying (IN-905XL). Growth rates in I/M 2090-T81 plate are also plotted for comparison (170).

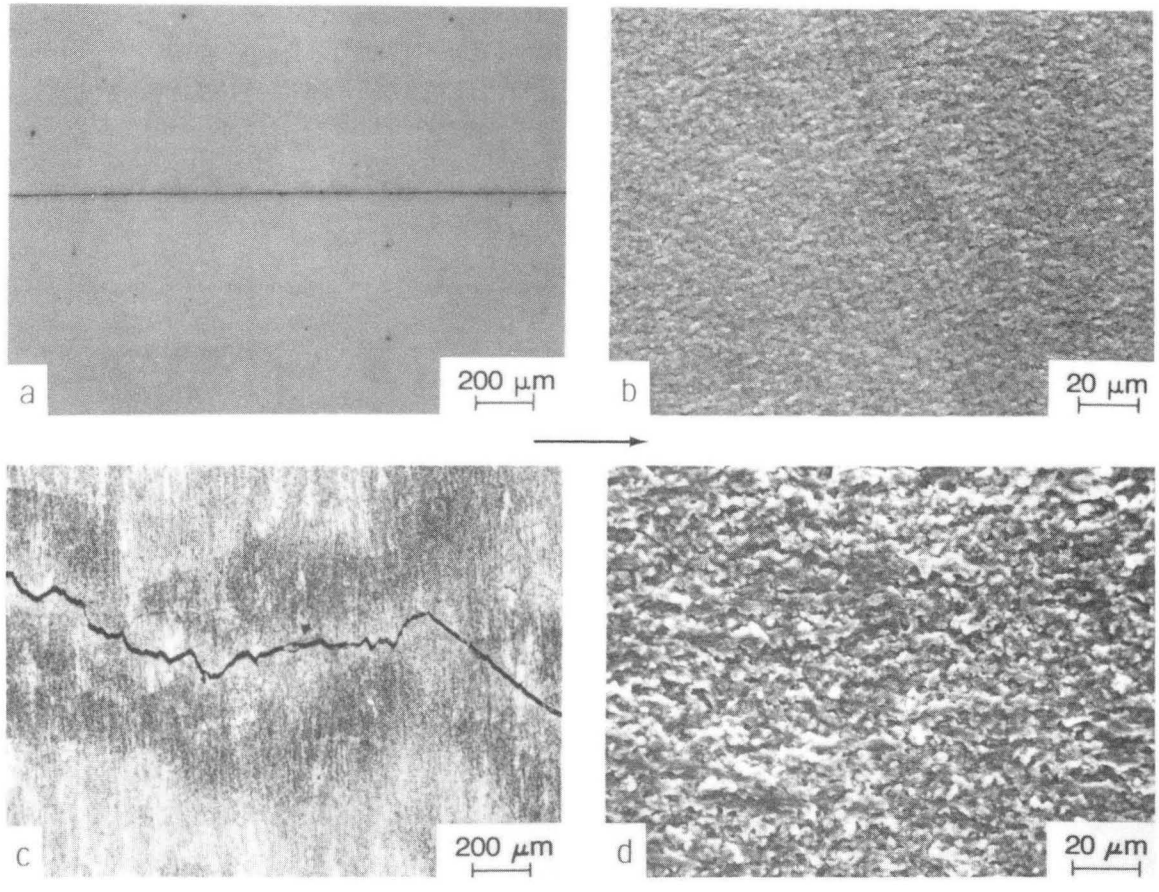

XBB 899-8156A

Fig. 31: Comparison of fatigue crack-path and fracture-surface morphologies in (a,b) MA IN-905XL, (c,d) RSP 644-B extrusions at ΔK levels between 6 and 8 MPa$\sqrt{m}$. Crack paths in MA 905-XL are unusually linear, without features of crystallographic crack growth. Arrow indicates the direction of crack advance (170).

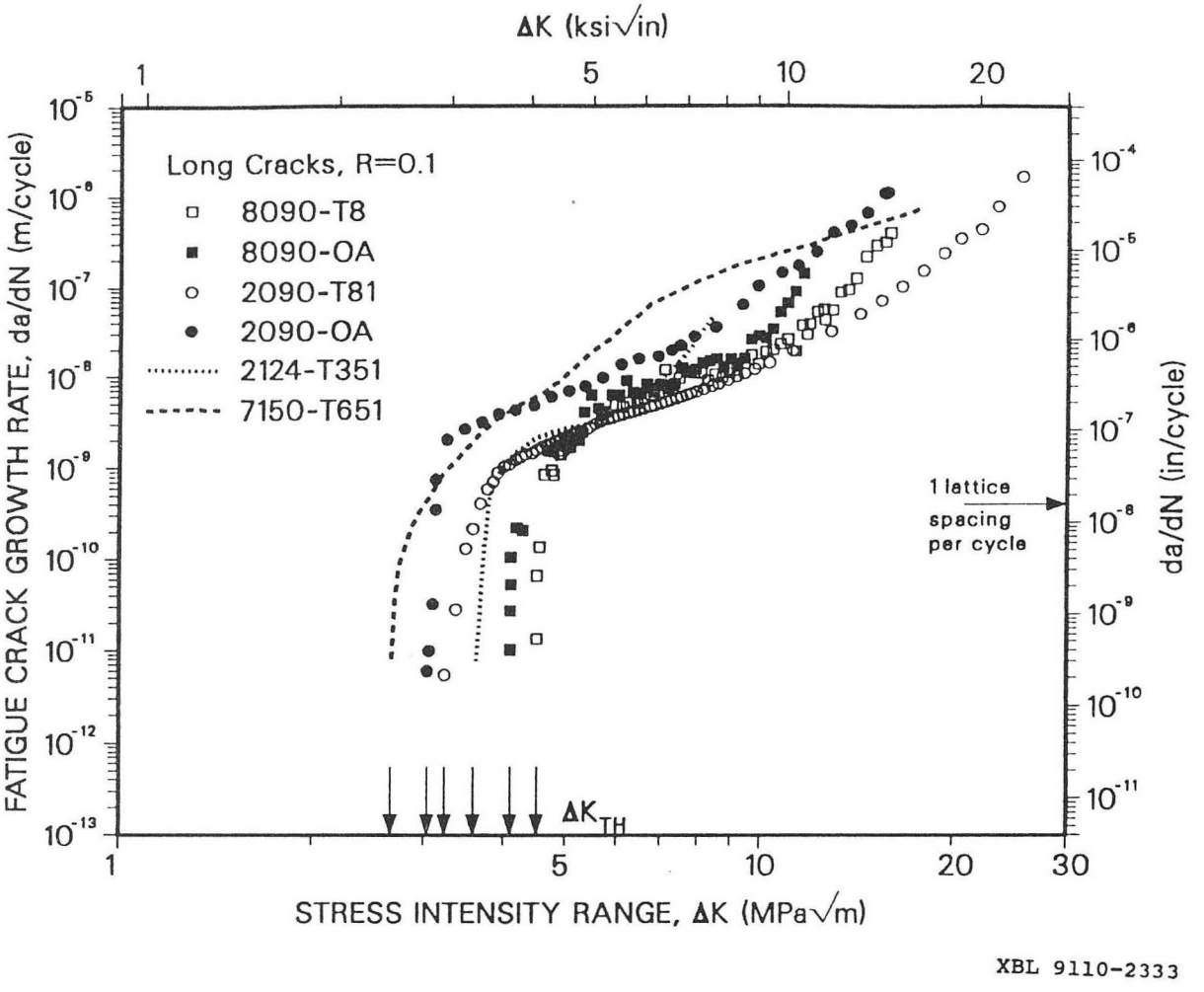

Fig. 32: Influence of high-temperature exposure of 1000 h at 436 K (overaging) on fatigue-crack propagation rates in 2090-T81, compared with traditional alloys. Although overaging degrades the crack-growth resistance of the Al-Li alloy, it still remains comparable, if not superior, to the traditional alloys (174,175).

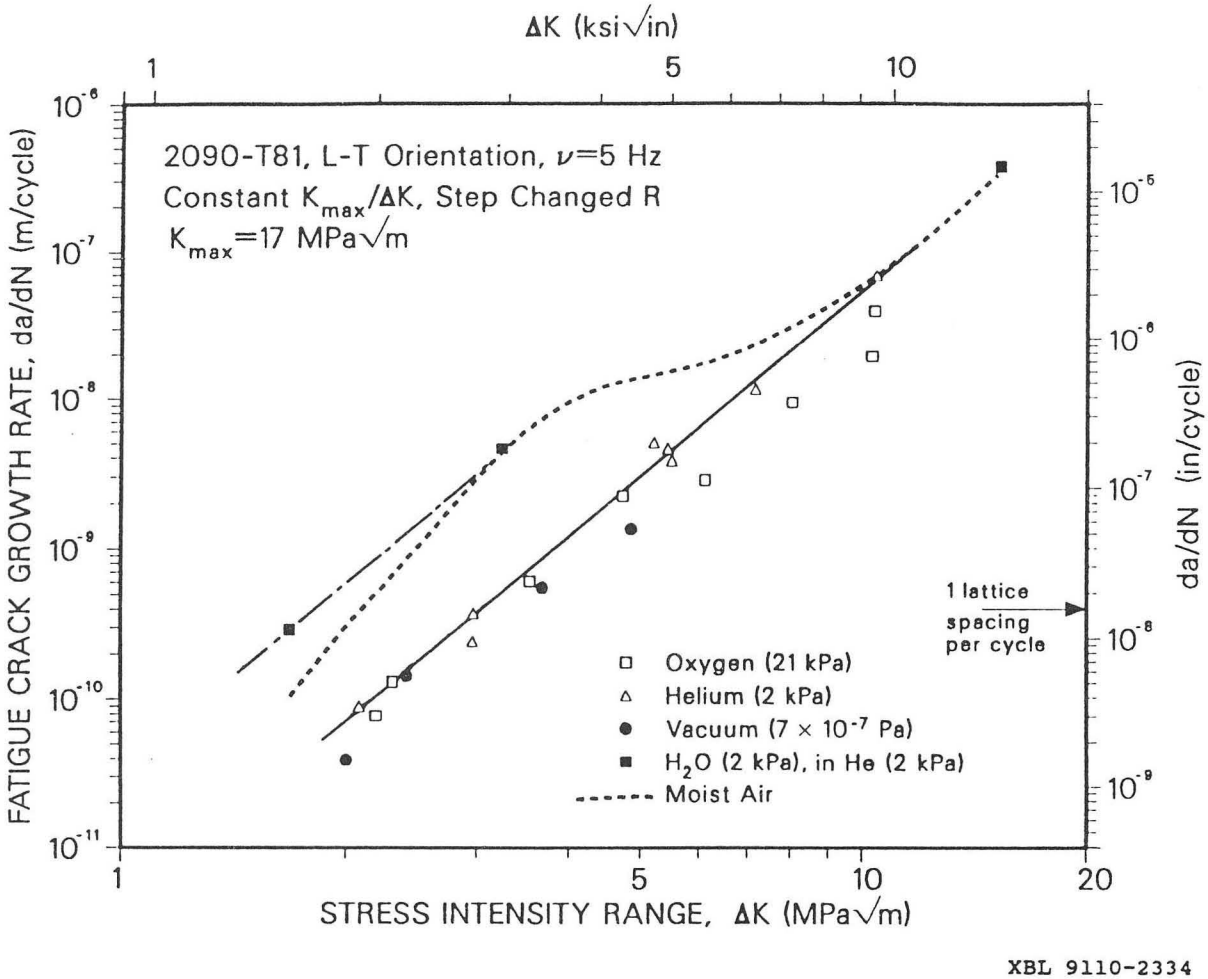

Fig. 33: Influence of environment on the intrinsic fatigue-crack growth rates in 2090-T81 alloy (L-T orientation, 5 Hz), obtained from short through-thickness cracks or long cracks under constant-K_{max}/variable-R conditions. Note that crack velocities are significantly enhanced only by water vapor, particularly close to ΔK_{TH}; behavior in O_2 is comparable to that in inert environments (131).

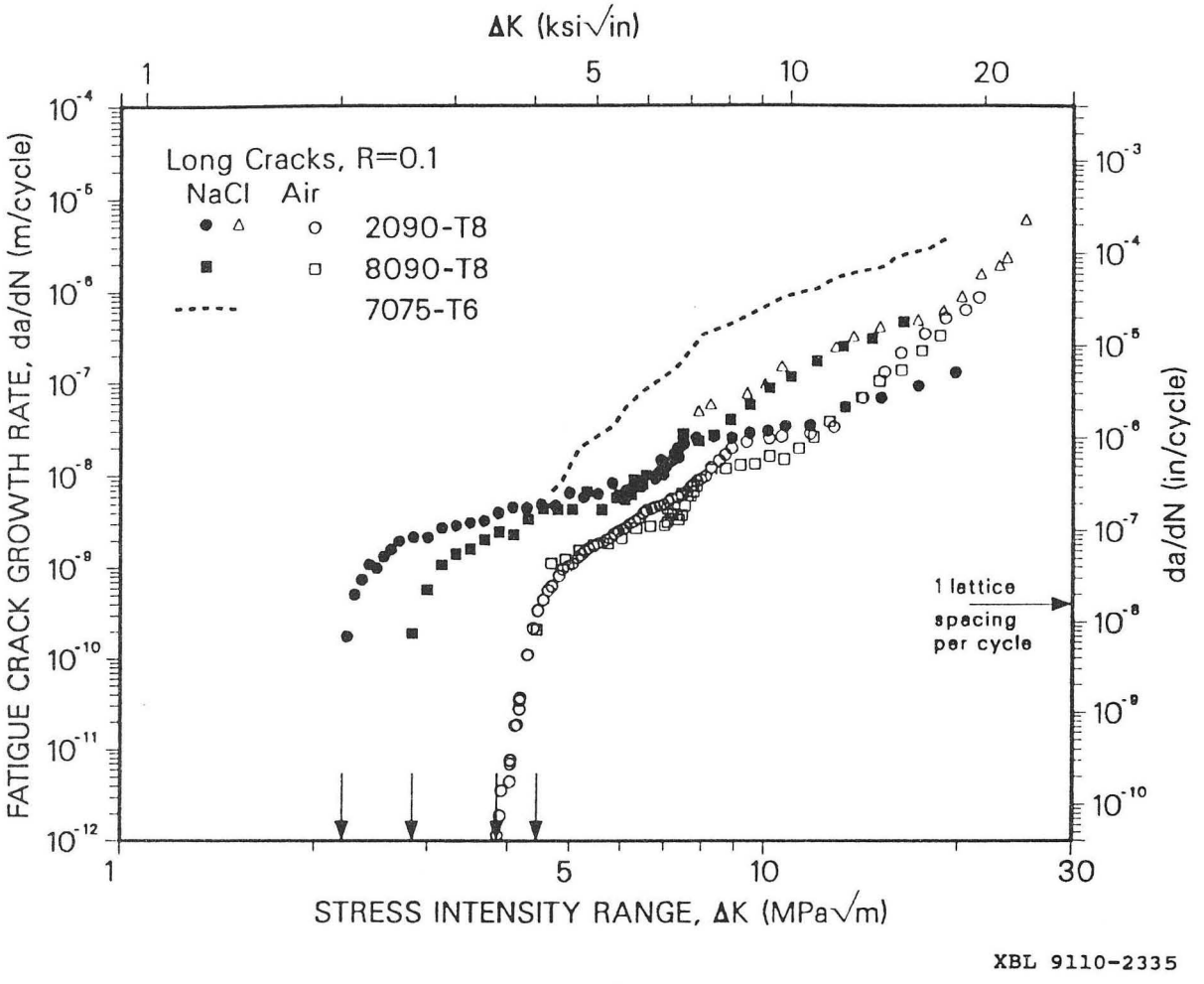

Fig. 34: Comparison of fatigue-crack propagation rates in 2090-T81 and 8090-T8 Al-Li alloys (L-T orientation, R=0.1, 50 Hz) compared to traditional 7075-T6 aluminum alloy in aqueous 3.5 wt.% NaCl environments (185,192).

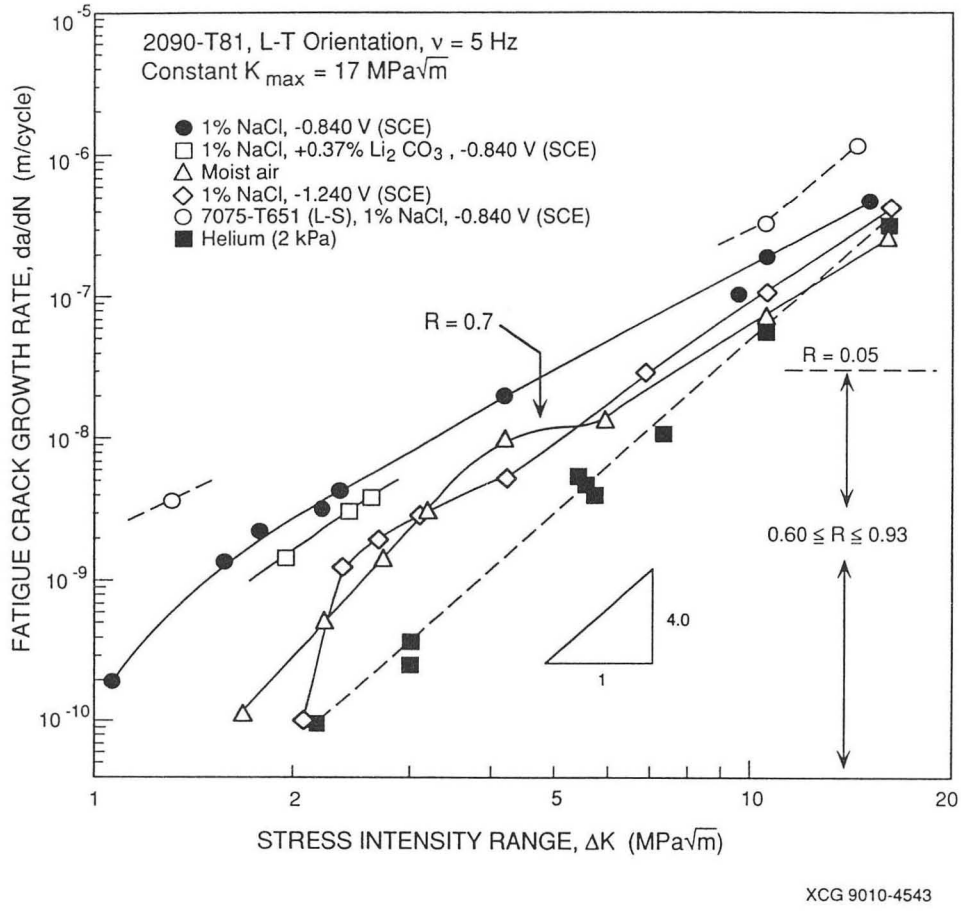

Fig. 35: Intrinsic corrosion-fatigue crack-growth rates for 2090-T81 and 7075-T6 alloys (L-T orientation, 5 Hz) in aqueous 1 wt.% NaCl under impressed anodic (-0.84 V) and cathodic (-1.24 V) potentials, compared to helium and moist air. Anodic polarization produces the largest corrosion-fatigue effect, which is reduced by Li_2CO_3 additions (131-133).

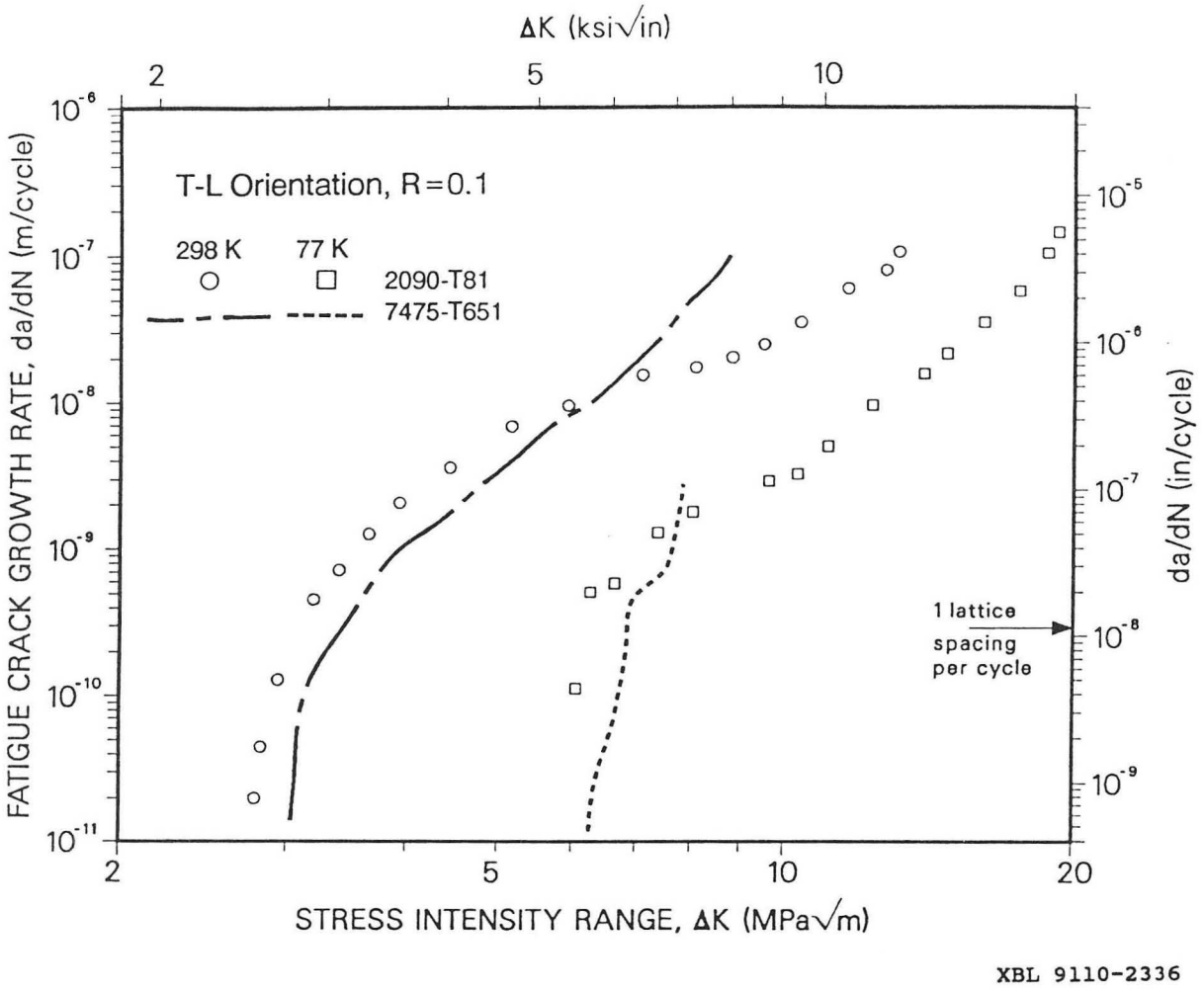

Fig. 36: Fatigue-crack propagation behavior in 2090-T81 and 7475-T6 alloys at ambient and liquid-nitrogen temperatures (T-L orientation, R=0.1, 50 Hz) (38).

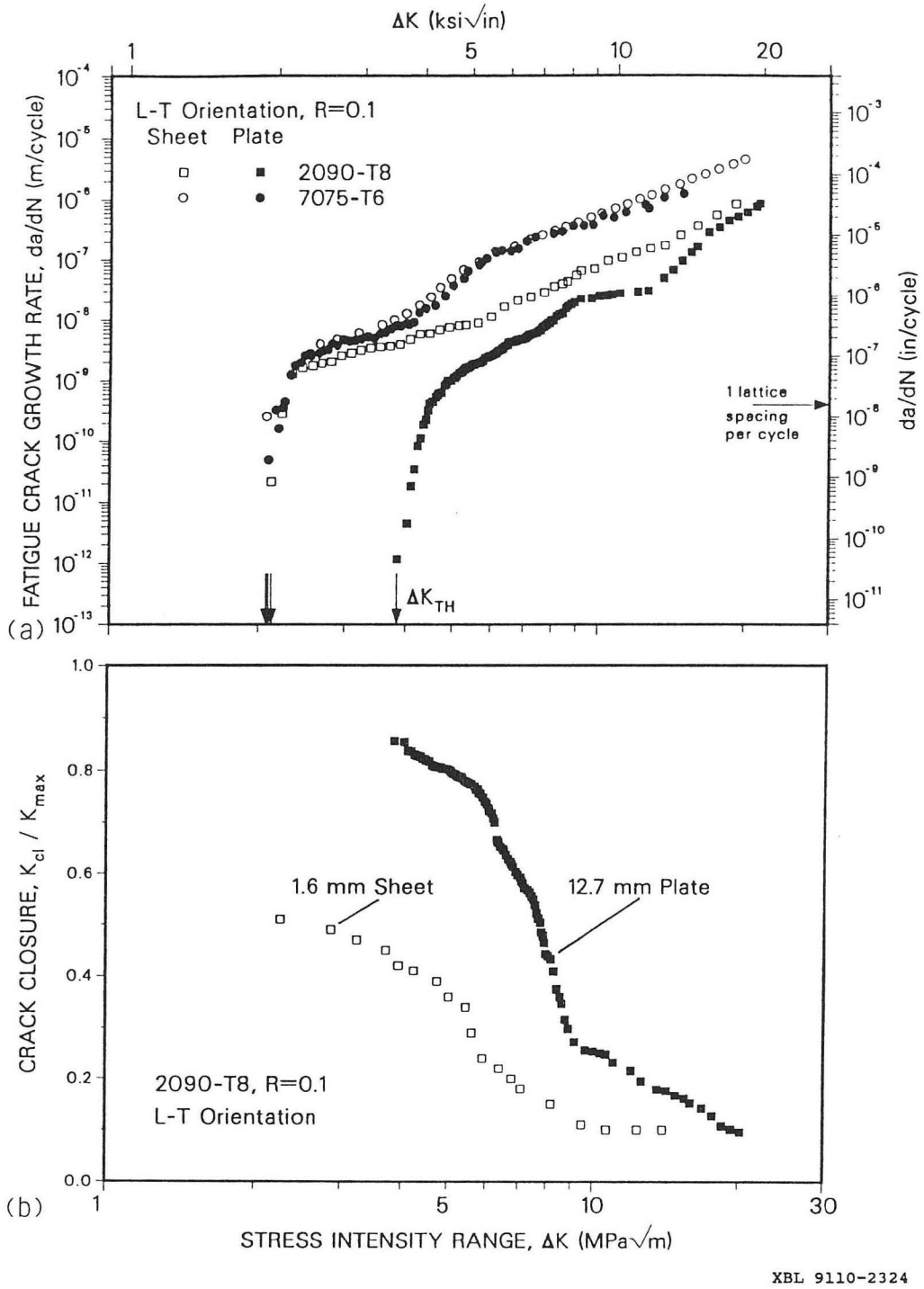

Fig. 37: (a) Fatigue-crack propagation and (b) crack-closure behavior in 1.6 mm-thin 2090-T83 sheet and 12.7 mm-thick T81 plate, as a function of ΔK (L-T orientation, R=0.1, 50 Hz, moist air), compared to 7075-T6 (67,207). Properties in plate were measured on 6.4 mm-thick samples (t/2 location); sheet behavior was examined in the as-received thickness.

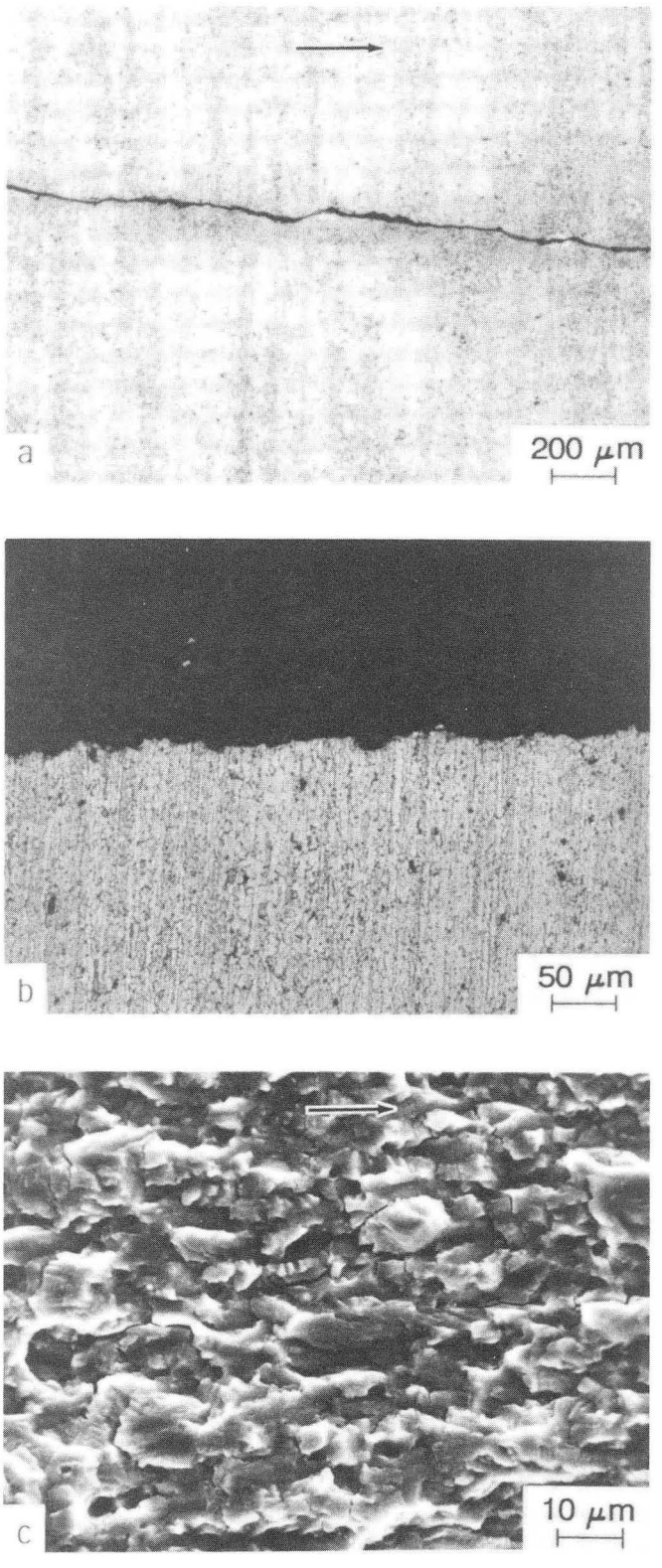

Fig. 38. Comparison of crack-path and fracture-surface morphologies during fatigue-crack growth in 2090-T83 sheet, showing crack paths (a) along the crack-growth direction, (b) specimen thickness, and (c) on the fracture surface. Arrow indicates the general direction of crack advance (207).

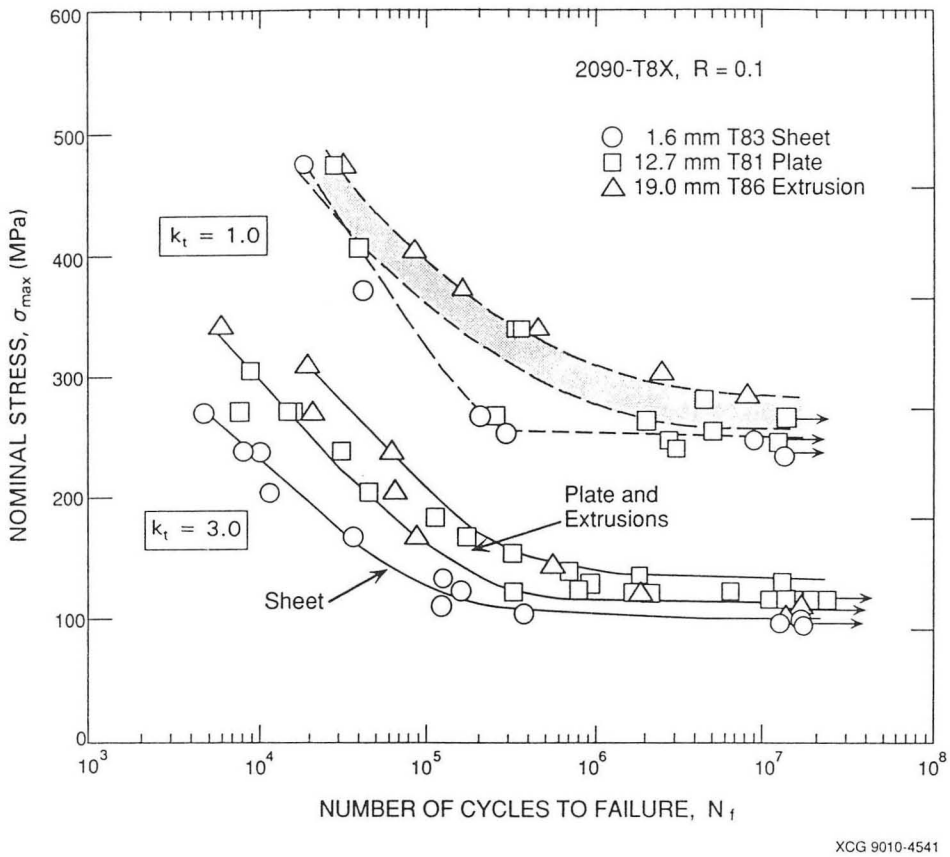

Fig. 39. Influence of wrought-product form on the HCF resistance of 2090-T8 (k_t = 1 or 3, R = 0.1, longitudinal orientation) in ambient air. Note that plates and extrusions show better fatigue resistance compared to sheet (67).

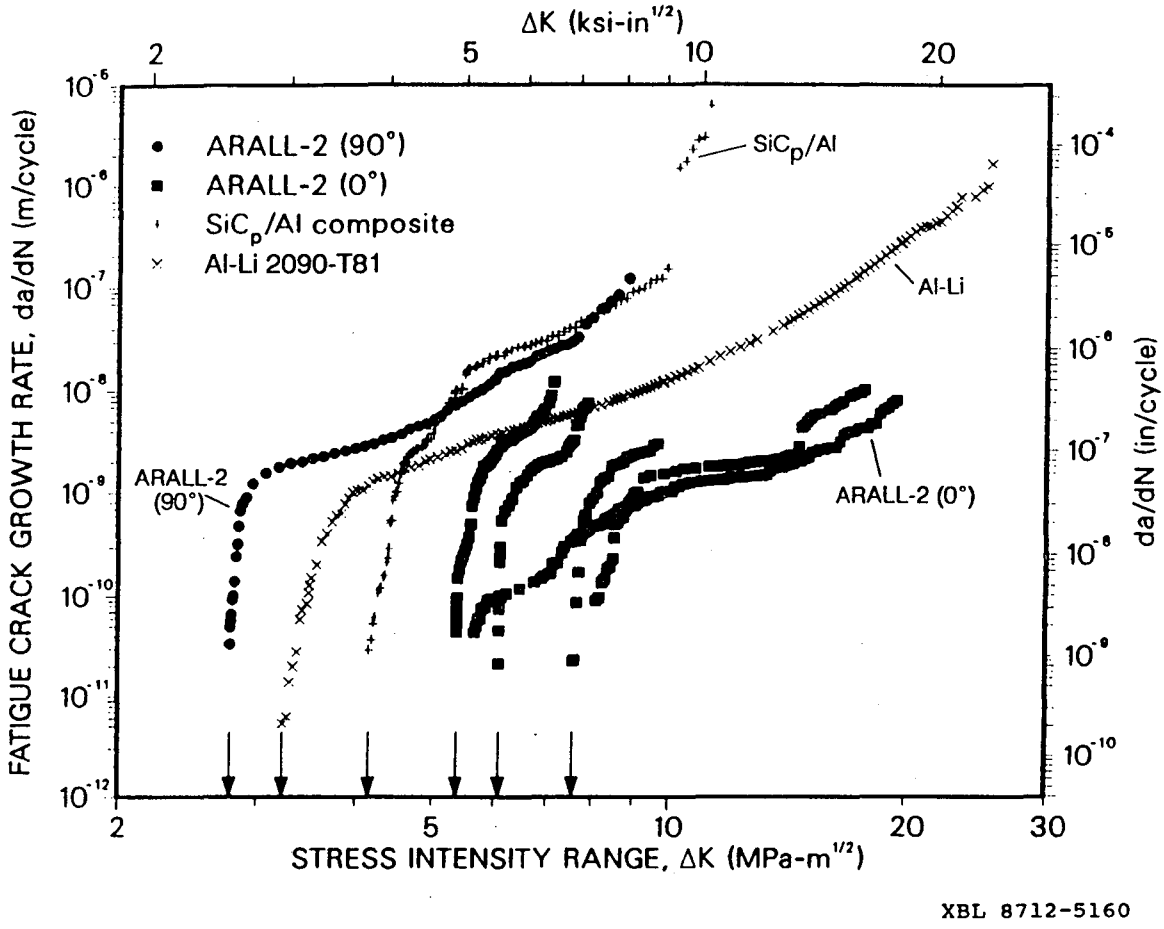

Fig. 40: Comparison of the fatigue-crack growth resistance of advanced structural aerospace materials, namely, Al-Li alloys (2090-T81), metal-matrix composites (SiC-particulate reinforced 7091 P/M aluminum alloy) and ARALL-2 laminates. Data taken from refs. 11,14,123.

LAWRENCE BERKELEY LABORATORY
CENTER FOR ADVANCED MATERIALS
1 CYCLOTRON ROAD
BERKELEY, CALIFORNIA 94720